

Atomic Force Microscopy: Principles, Instrumentation, and Applications

Francesco Ruffino (francesco.ruffino@ct.infn.it)

*Dipartimento di Fisica e Astronomia, Università di Catania, via S. Sofia
64, 95123 Catania, Italy*

CNR-IMM MATIS via S. Sofia 64, 95123 Catania, Italy

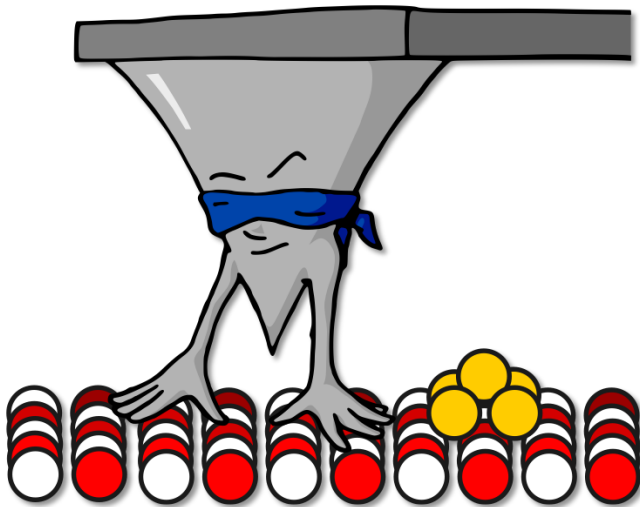
Literature:

*1) V. L. Mironov, **Fondamenti di Microscopia a Scansione di Sonda, tutto***

Additional

*2) A. Foster, W. Hofer, **Scanning Probe Microscopy***

*3) B. Bhushan, **Scanning Probe Microscopy in Nanoscience and Nanotechnology***



Outline

Part 1: AFM, instrumentations, principles and mode of operations

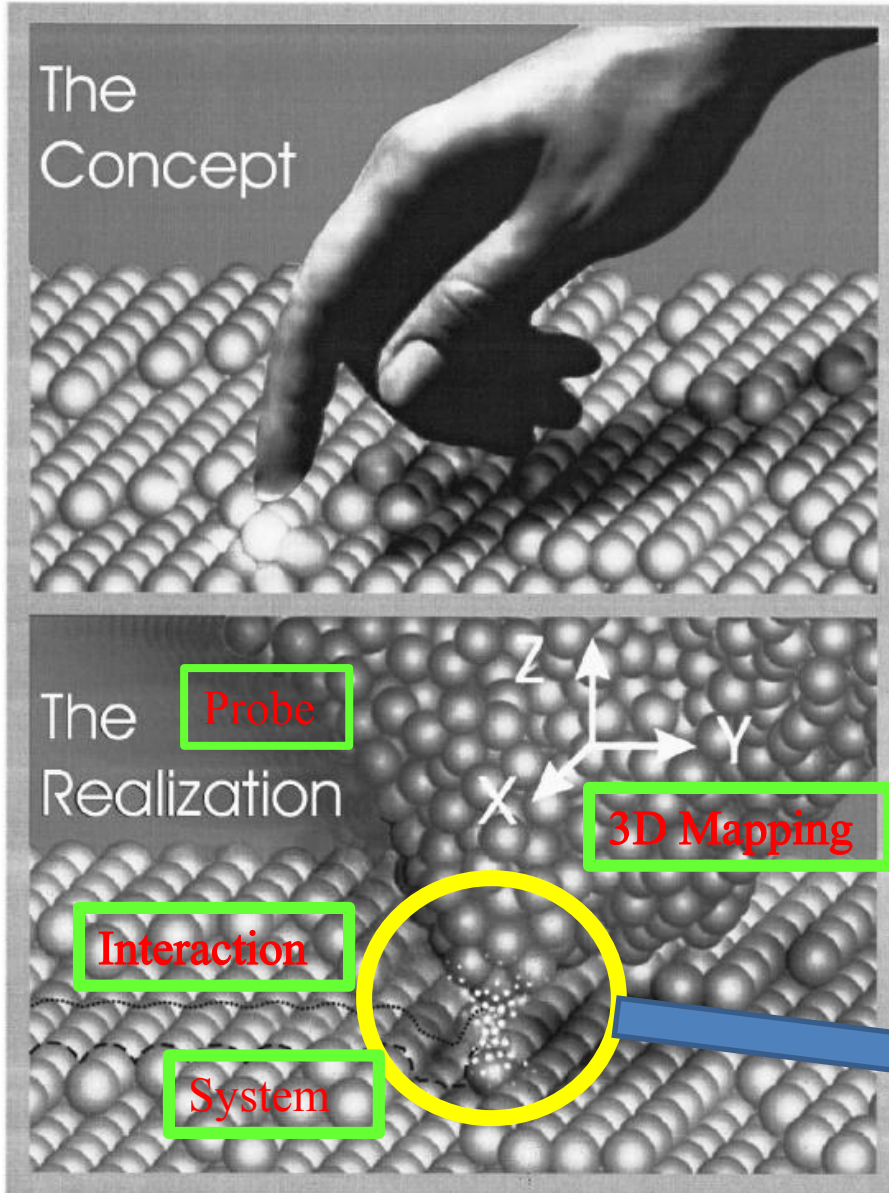
- 1) SPM: The principle of a **local probe**
- 2) Scanning Tunneling Microscopy (STM): the basis for the AFM
- 3) Atomic Force Microscopy (AFM): basic ideas and concepts

Part 2: Applications to Nanoscale Characterizations, Manipulation and Fabrications

- 1) “Physical Applications”:
- 2) “Chemical Applications”:
- 3) “Biological and medical Applications”:

Part 1: A Review of Scanning Probe Microscopy

1) SPM: The principle of a local probe



Needs for SPM:

- 1) Characterization of the basic properties of the matter at atomic and molecular scale:
 - Structural (imaging);
 - Electrical;
 - Mechanical;
 - Magnetic
- 2) Manipulation of the matter at atomic and molecular scale (Manipulation, Nanofabrication,....).

The “Touch” of a local probe with the nano-object is given by the type of interaction, which addresses a distinct property, process or function by the strength of the interaction.

The Interaction

$$B = f(A)$$

B: Macroscopic parameter

A: Microscopic parameter

2) History of Scanning Probe Microscopes

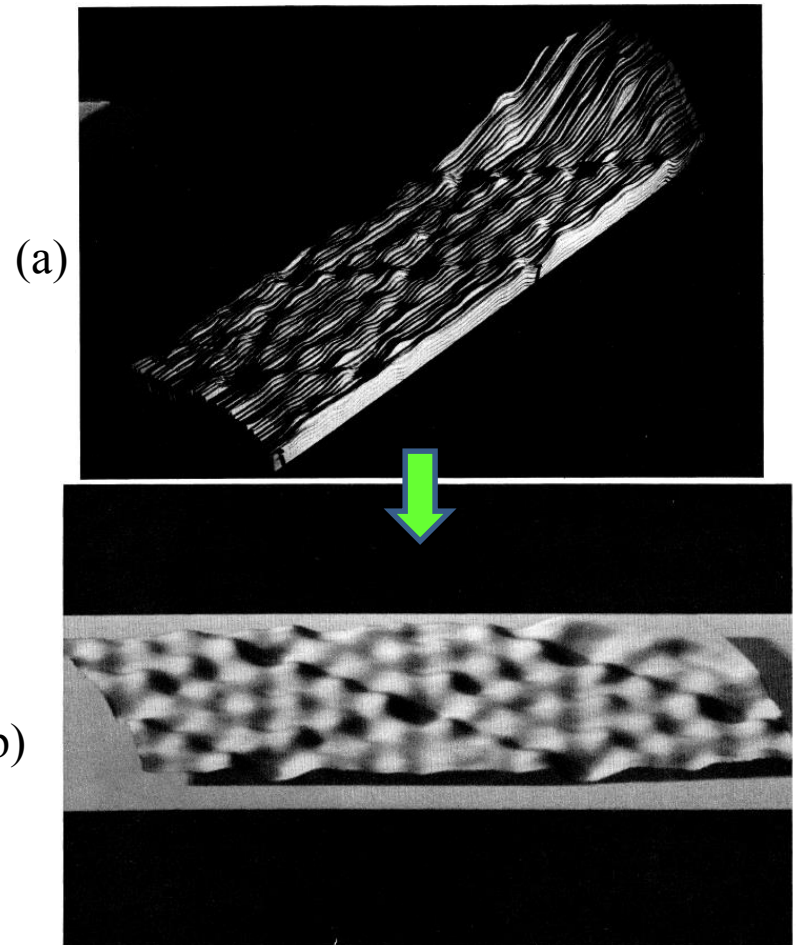
1981: Scanning Tunneling Microscope (STM) invented by Gerd Binnig & Heinrich Rohrer



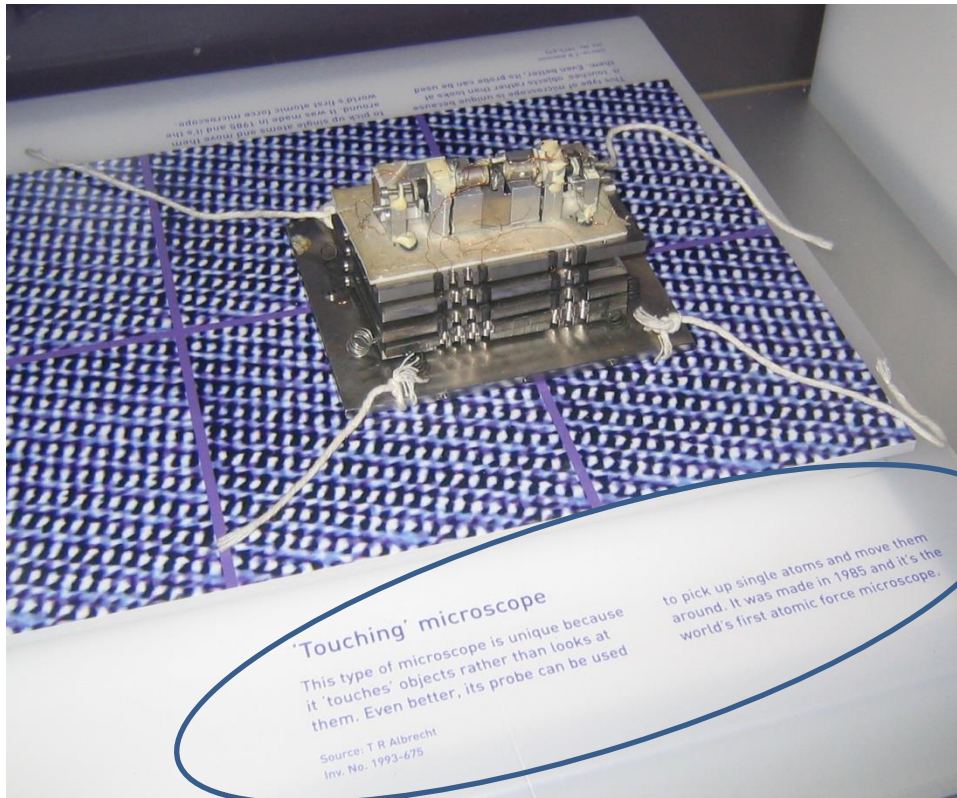
7x7 reconstruction of Si(111). (a) Relief assembled from the original recorder traces, from Binnig et al. (b) Processed image of the 7x7 reconstruction of Si(111).

Characteristic of the rhombohedral surface unit cell are the corner hole and the 12 maxima, the adatoms. In the processed images, the six adatoms in the right half of the rhombi appear higher.

(Phys. Rev. Lett. 50, 120, 1983)



1985: Atomic Force Microscope (AFM) invented by: Gerd Binnig, Calvin Quate & Christoph Gerber



This type of microscope is unique because it “touches” objects rather than looks at them. Even better, its probe can be used to pick up single atoms and move them around. It was made in 1985 and it’s the world’s first atomic force microscope.

Science Museum (London)

1986: Gerd Binnig and Heinrich Rohrer shared the Nobel Prize

3) Scanning Tunneling Microscope (STM)

3.1) System Components and Principles of Operation:

- Tunneling Current
- Scansion (Piezoelectric Tube)
 - Feedback system

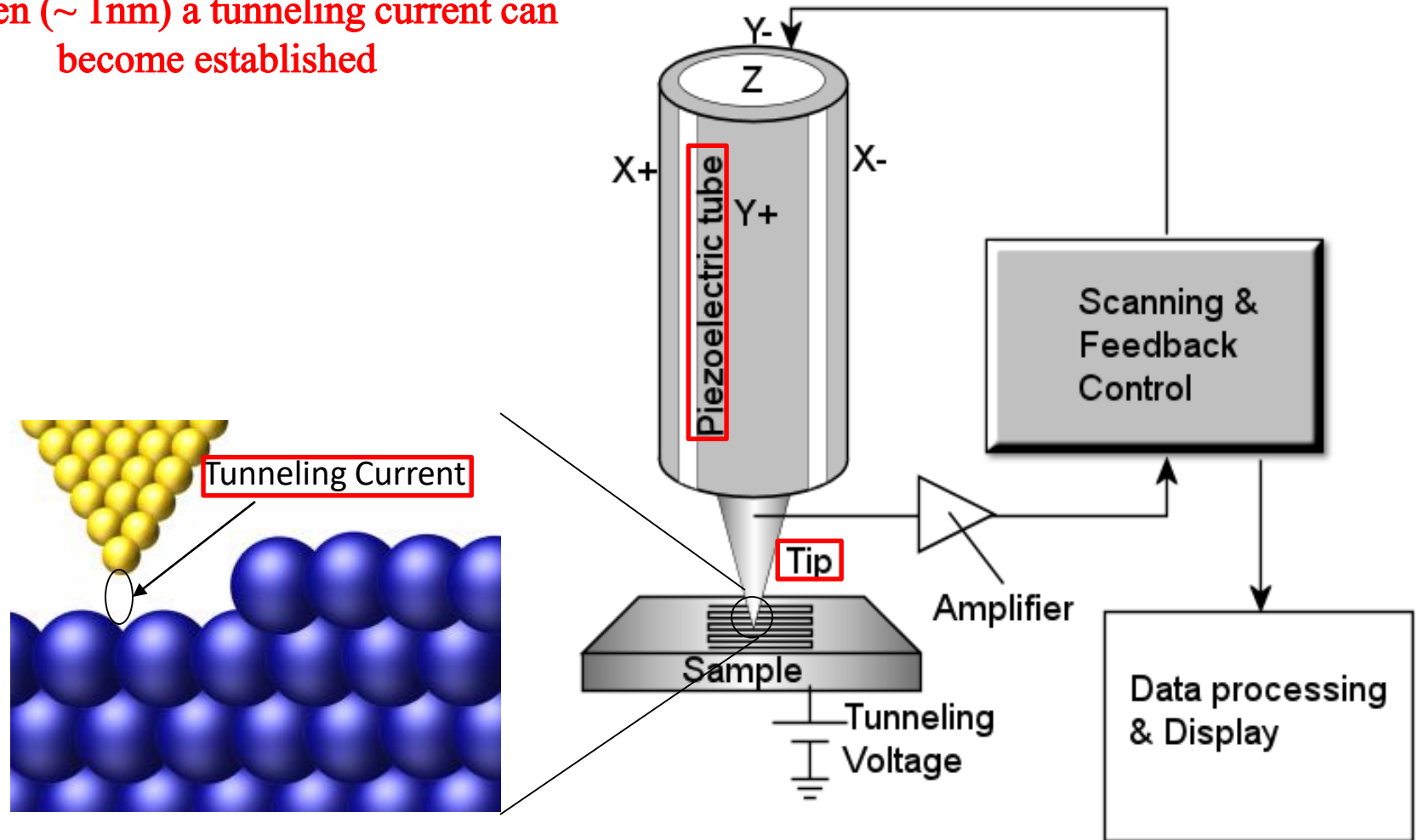
3.2) Operating modes

3.3) Applications

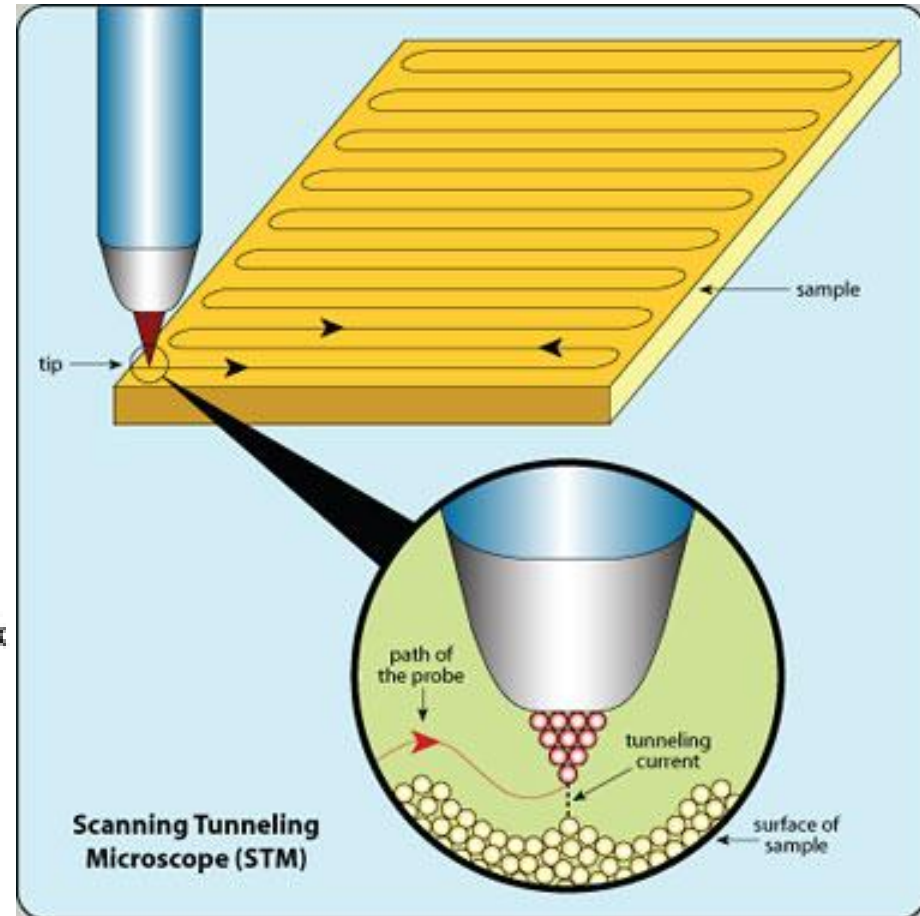
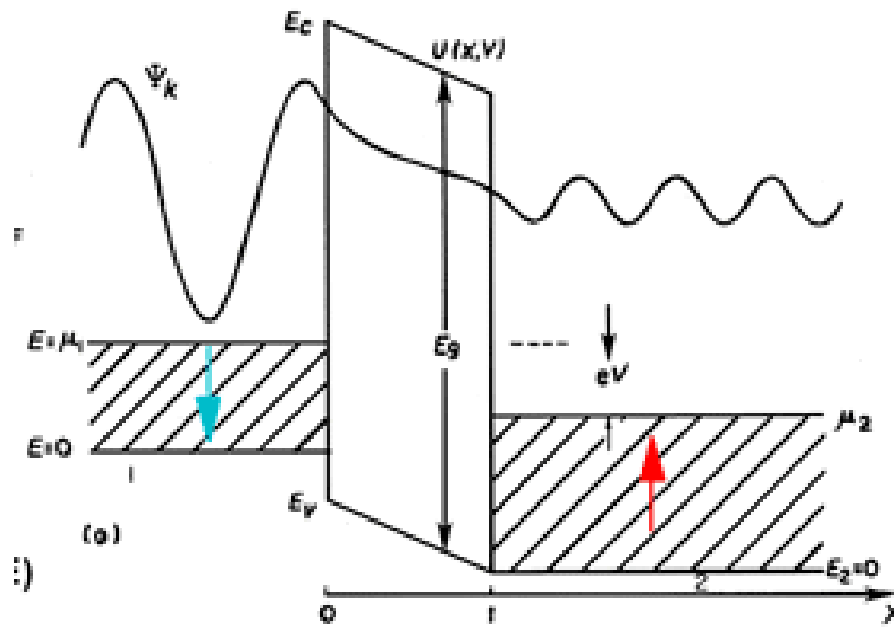
3.4) Advantages & Disadvantages

3.1) STM System Components and Principles of operation

When the tip of the STM probe is sufficiently close to the surface of the specimen ($\sim 1\text{nm}$) a tunneling current can become established



Principles of STM: A) Tunneling Current



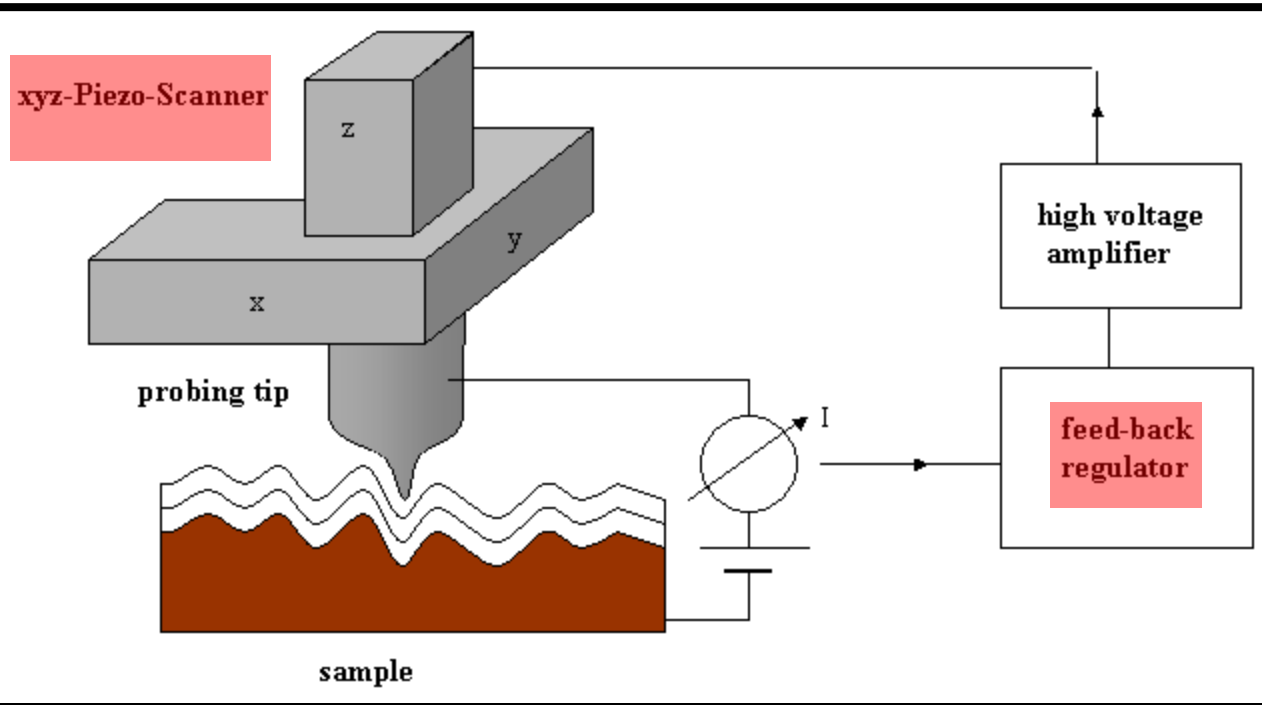
$$I(z) = I_0 e^{-2\kappa z}$$

$$\kappa = \frac{\sqrt{2m\phi}}{\hbar}$$

$$B = f(A)$$

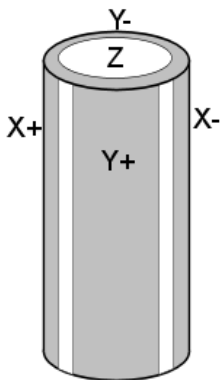
F. J. Giessibl, "Advances in Atomic Force Microscopy", Rev. Mod. Phys. 75, 949 (2003)

The probe is scanned over the surface in a raster pattern similar to that of a SEM. Each coordinate (X, Y, & Z) is recorded by a computer.



The ability to precisely position the probe of an STM is made possible by an XYZ Piezo-Scanner which coupled to a feedback regulator keeps track of the tunneling current and precisely positions the tip accordingly.

Piezoelectric tube scanner



Piezoelectric materials are used to create a tube scanner. This forms one of the basic components of scanning probe microscopes. These can be used to manipulate an object in three dimensions under electronic control.

Piezoelectric Effect

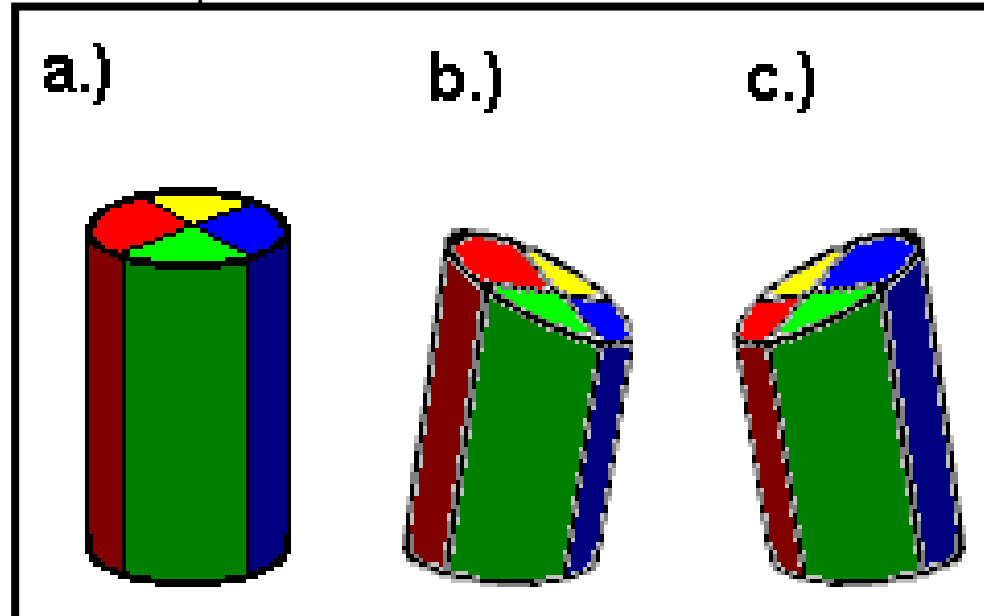
- Certain materials exhibit what is called the piezoelectric effect.
- This is an effect where changing the size of an object results in a voltage being generated by the object.
- Conversely when a voltage is applied to a piezoelectric object then the size of the object changes.

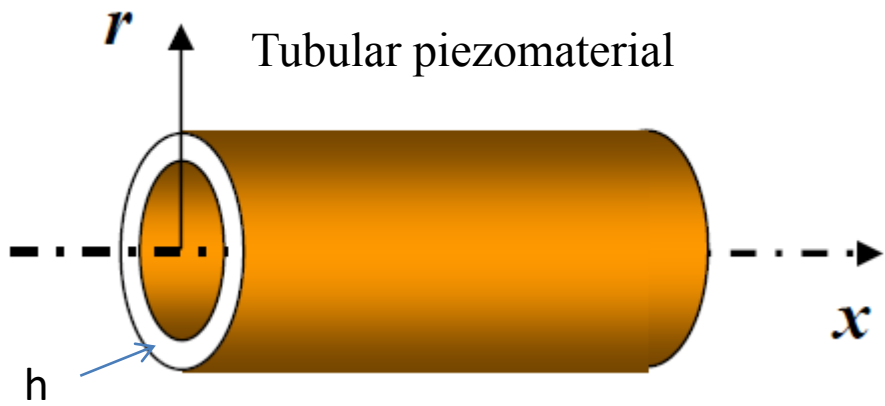
Crystals which acquire a charge when compressed, twisted or distorted are said to be piezoelectric. Piezoelectric ceramic materials have found use in producing motions on the order of nanometers in the control of STMs and other devices.

$$u_{ij} = d_{ijk} E_k$$

Deformation tensor Piezoelectric tensor components Electric field components

Lead zirconium titanate is one of the most common piezoelectric materials. Resolution: 1nm/V

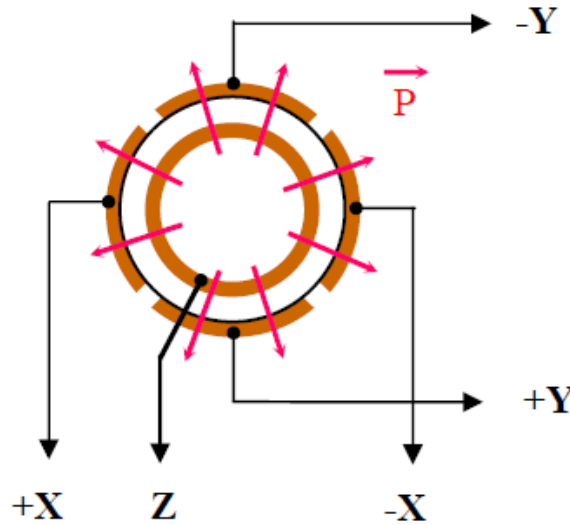
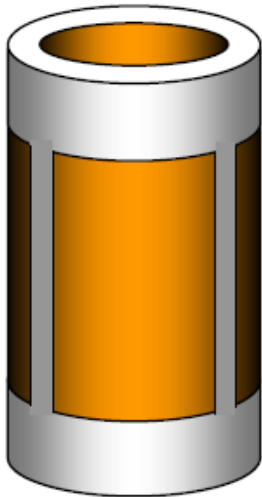




$$u_{xx} = \frac{\Delta x}{l_0} = d_{\perp} E_r$$

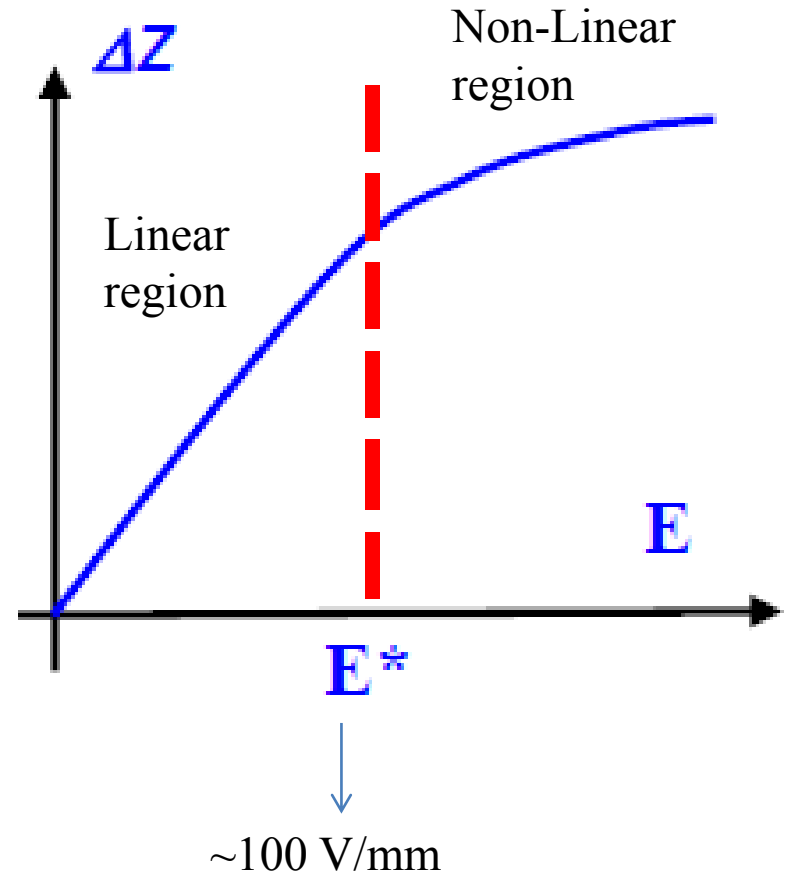
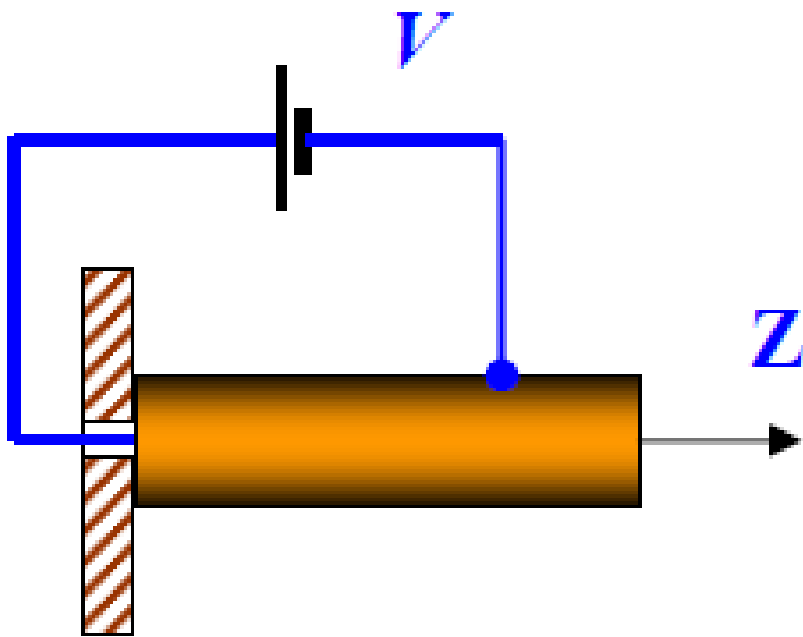
$$\Delta x = d_{\perp} \frac{l_0}{h} V$$

Tubular scanners (used in modern systems)



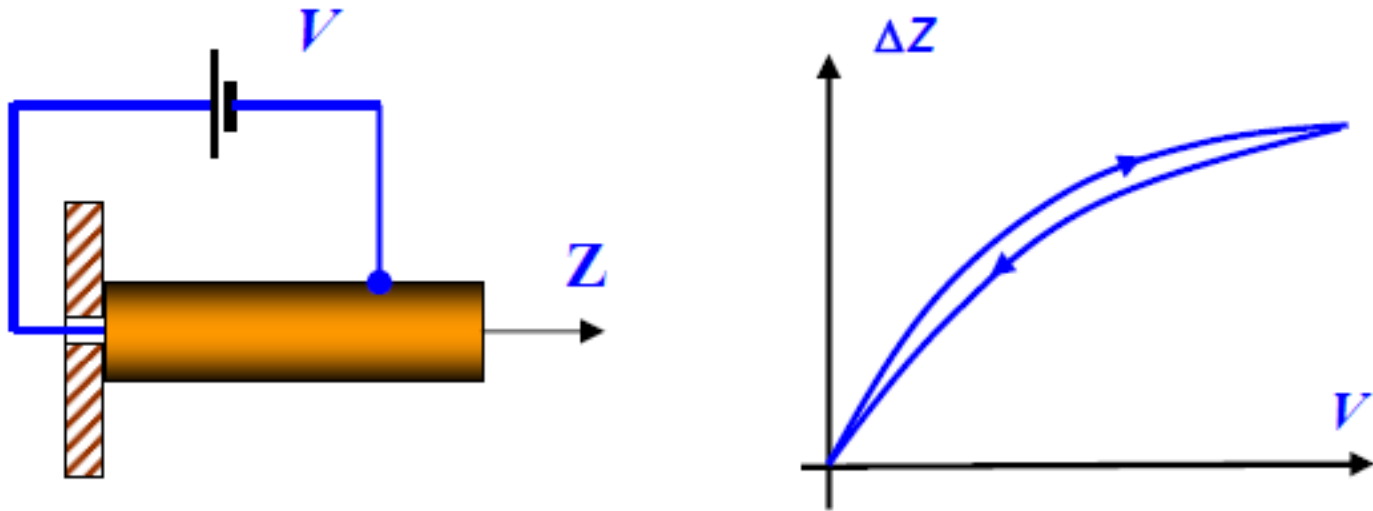
$$V_x, V_y, V_z$$

Drawback 1: non-linearity of the piezoelectric effect

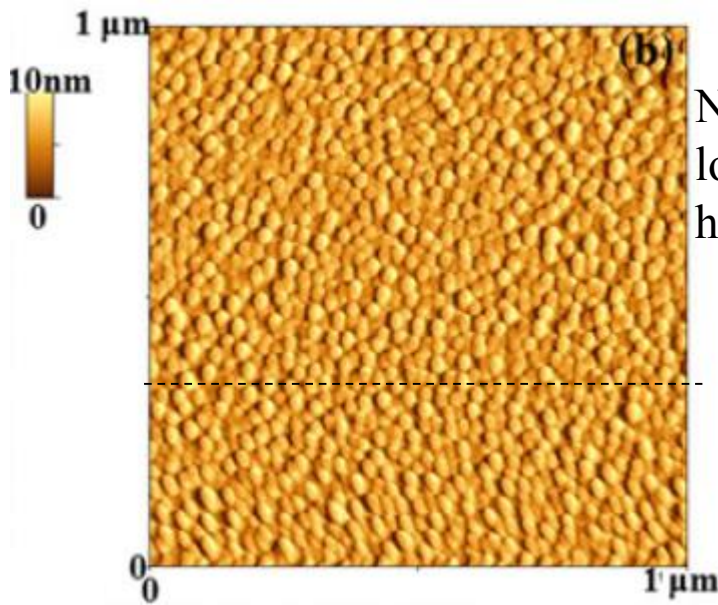


So, in general, real systems work at $E < E^*$

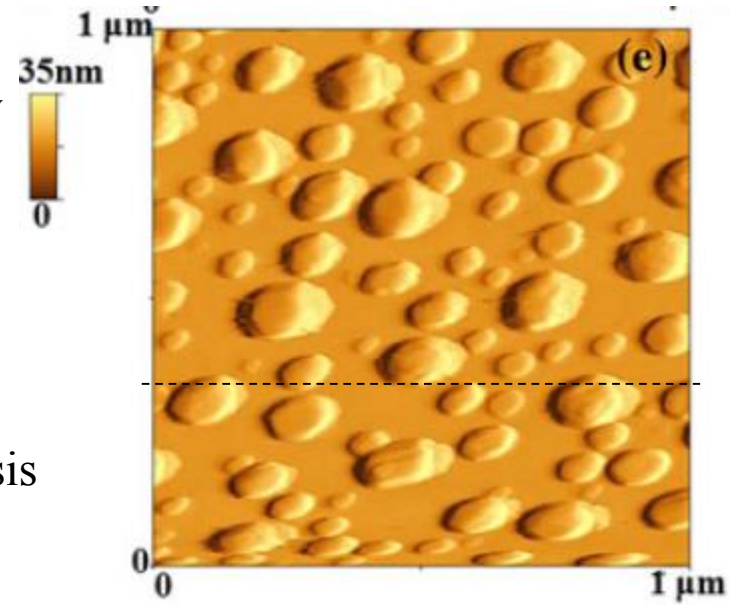
Drawback 2: Hysteresis



Z depends on the value and sign of the control signal $V \rightarrow$ distortion of the acquired image.
It is important to minimize the hysteresis effect



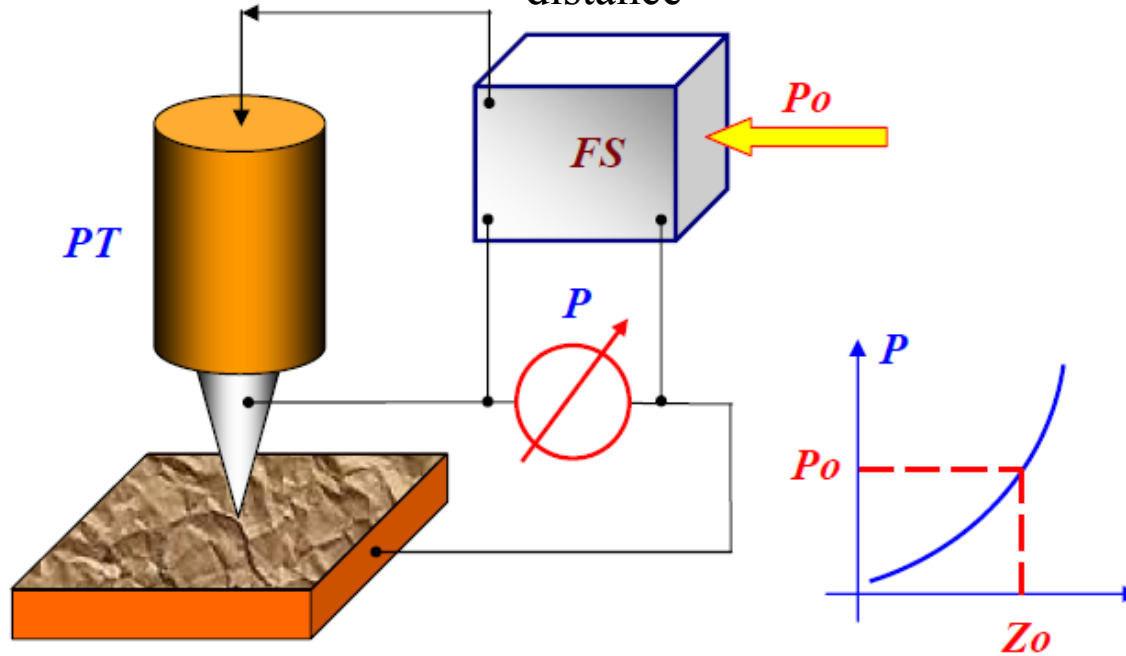
Not or very
low
hysteresis



hysteresis

Feedback system

Feedback system: it controls the tip-surface distance



The FS maintains constant the value of a P parameter (equal to a value P_0 chosen by the operator). If the tip-sample surface changes then P changes. In the FS the $\Delta P = P - P_0$ is amplified and transmitted (by a transducer) to the piezoelectric system (PT) which controls the tip-sample distance. The transducer exploits the ΔP signal to change the tip-sample distance in order to re-establish the condition $\Delta P = 0$. In such a way the tip-sample distance can be controlled, potentially, with $\sim 0.01 \bar{X}$.

3.2) Operating modes

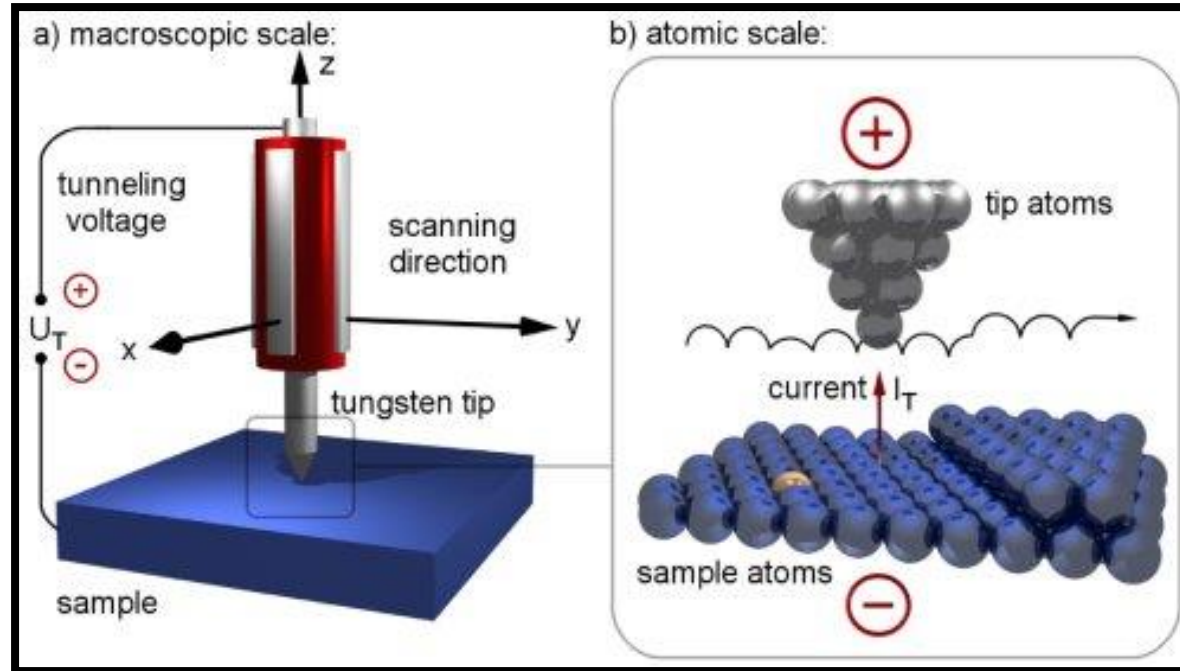
- **Constant height mode**
 - Current changes exponentially
 - Requires a smooth surface
- **Constant current mode**
 - Beware of insulators



Constant_height_mode_en_n.swf



Constant Current mode_en_n.swf



Constant Height mode:

If the Z position of the tip is kept constant the tunneling current will change as it moves across the surface. If the changes in current are recorded then the topography of the specimen can be inferred.

Constant Current mode:

If the tunneling current is kept constant the Z position of the tip must be moved up and down. If this movement is recorded then the topography of the specimen can be inferred.

3.4) STM Advantages & Disadvantages

- **Advantages**

- Able to obtain very high resolution images of conductors and semiconductors.
- Inexpensive to purchase

- **Disadvantages**

- Will not work with insulators.
- If there are insulating materials present on the sample you can crash the tip.
 - Often need to be used under vacuum.

4) Atomic Force Microscope

4.1) System Components and Principles of Operation:

- Tip, Laser, Piezoelectric Tube
 - Force vs Distance

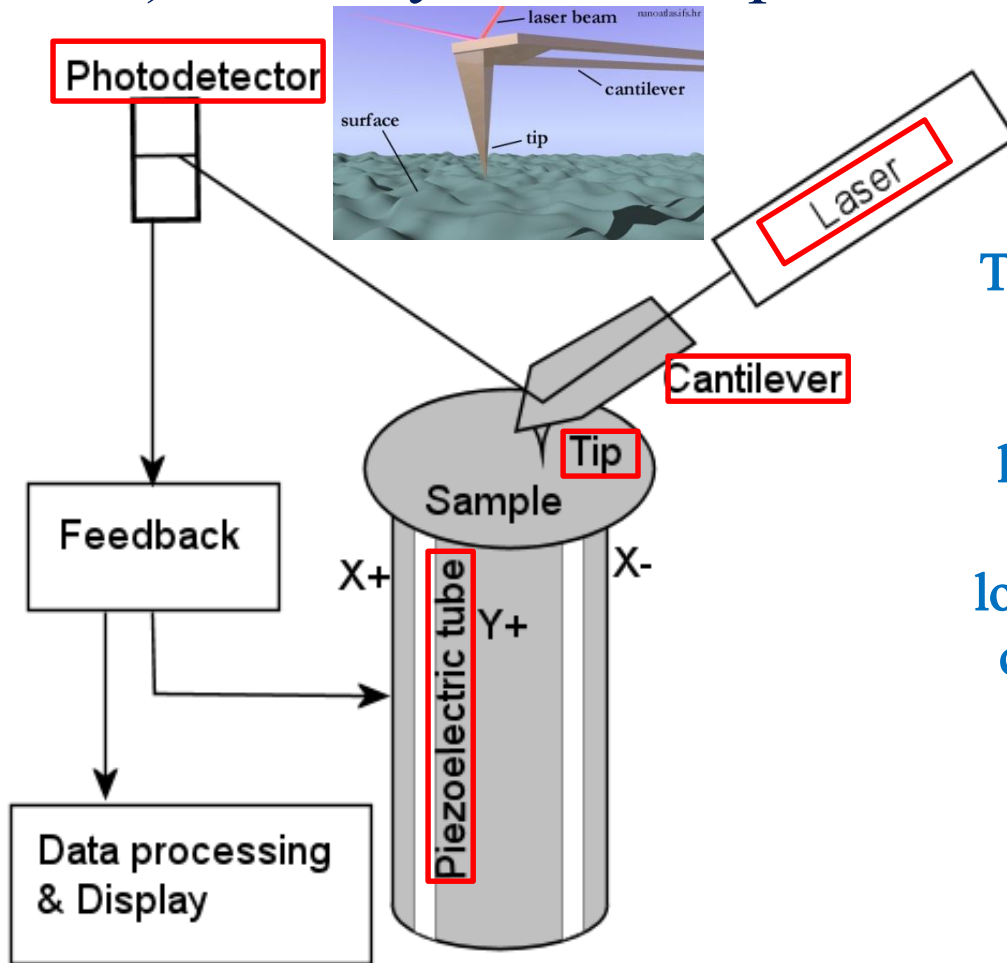
4.2) Operating modes

4.3) AFM Cantilevers and Tips

4.4) Applications

4.5) Advantages & Disadvantages

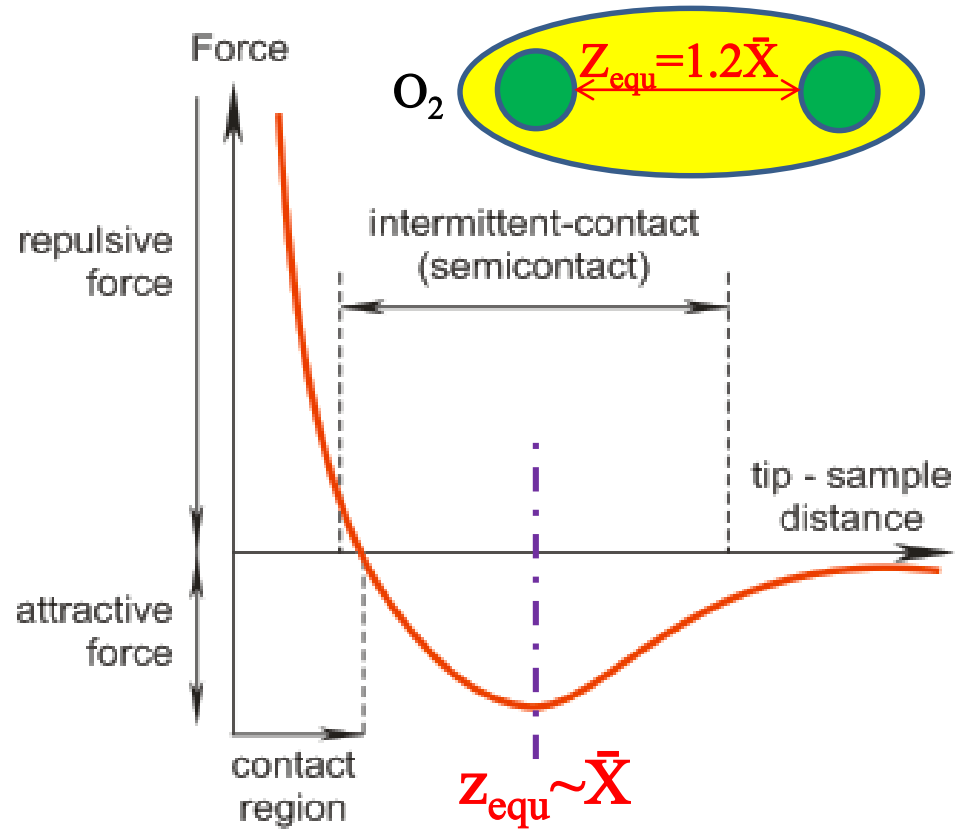
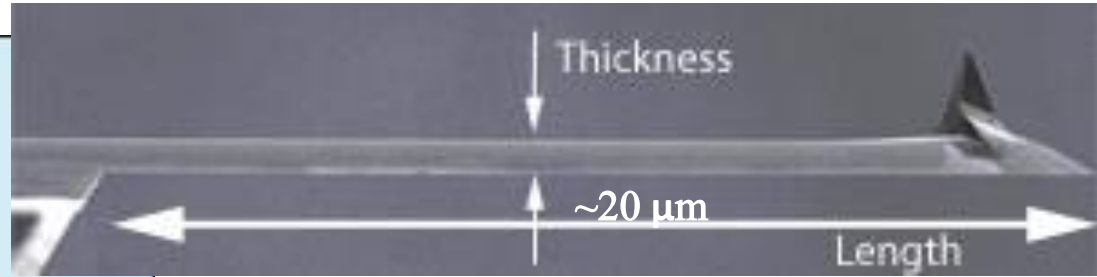
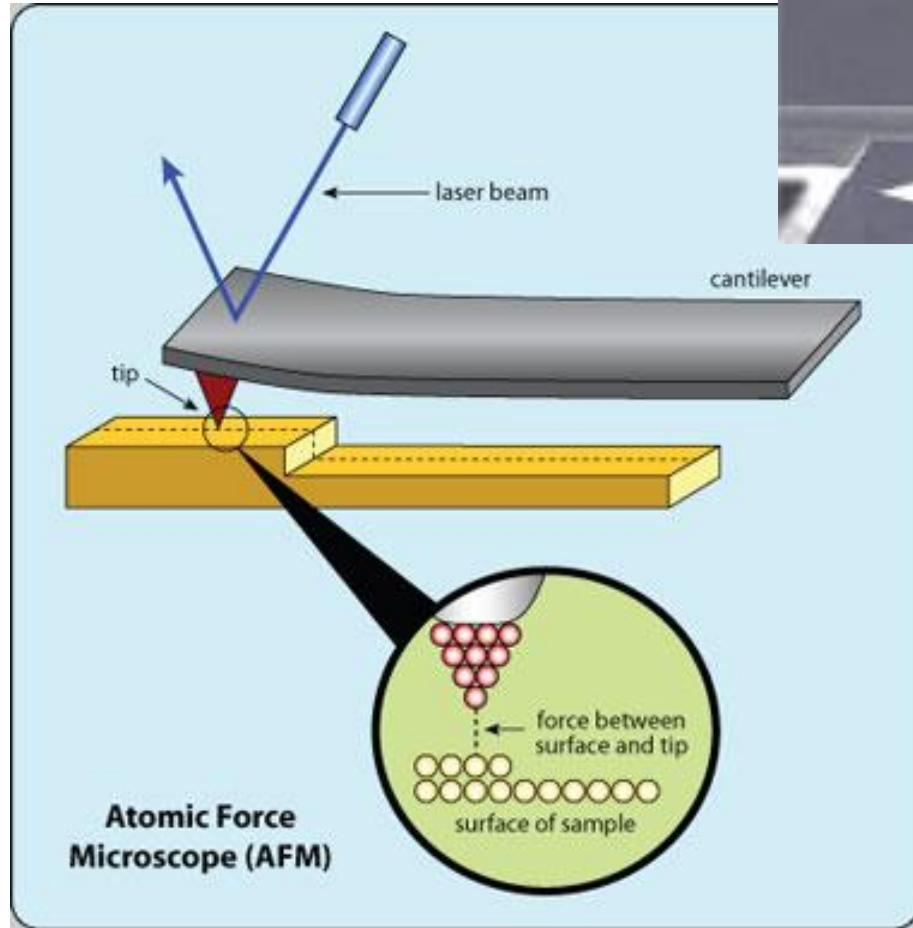
4.1) AFM System Components and Principles of Operation



The atomic force microscope (AFM), uses a sharp tip attached to the end of a cantilever rasters across an area while a laser and photodiode are used to monitor the tip force on the surface. A feedback loop between the photodiode and the piezo crystal maintains a constant force during contact mode imaging and constant amplitude during intermittent mode imaging.

As with STM the probe is rastered by the movement of a Piezo-electric device

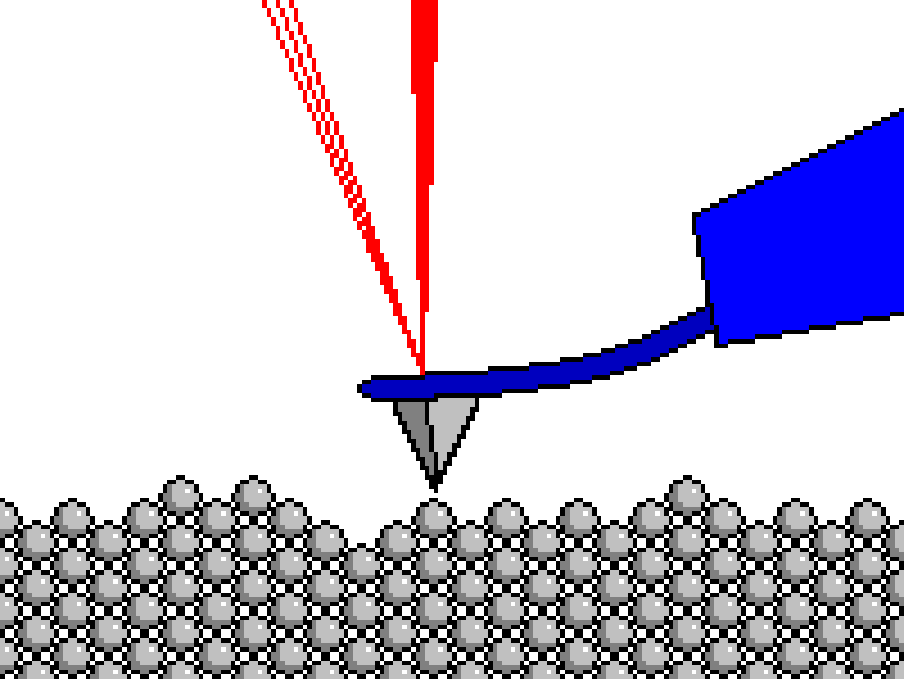
Force vs Distance



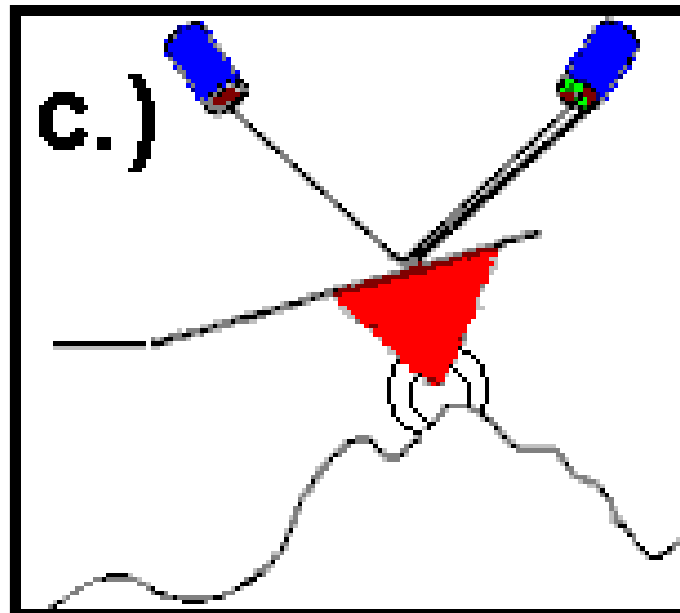
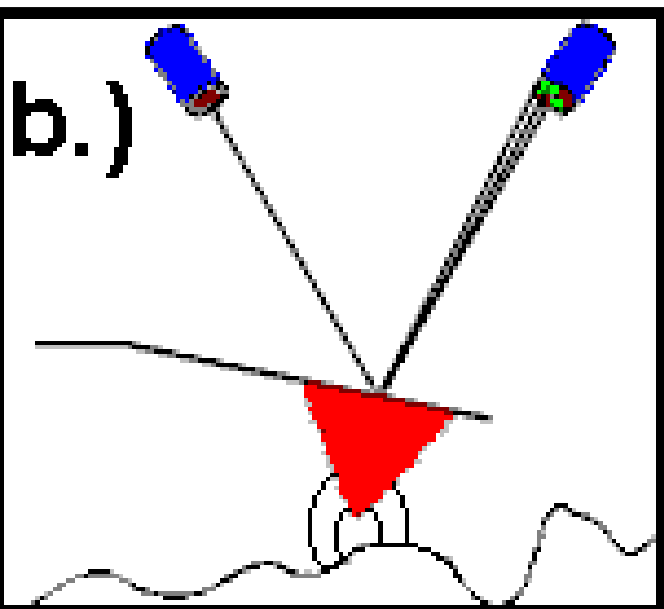
$$V(z) = -E_B \left(2 \frac{z^6}{z_0^6} - \frac{z^{12}}{z_0^{12}} \right)$$

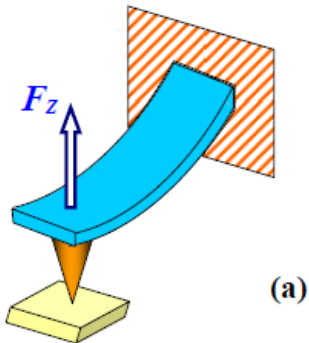
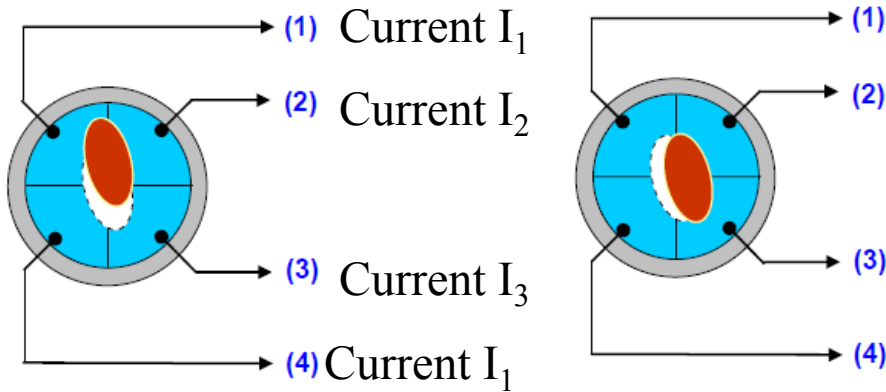
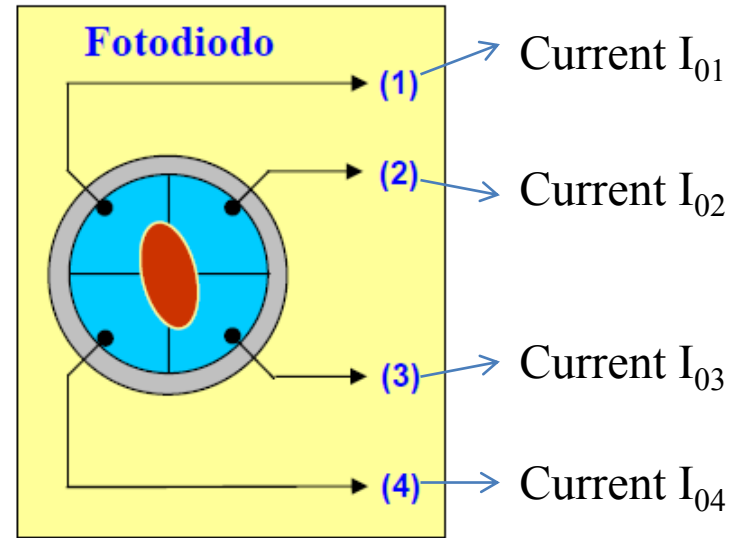
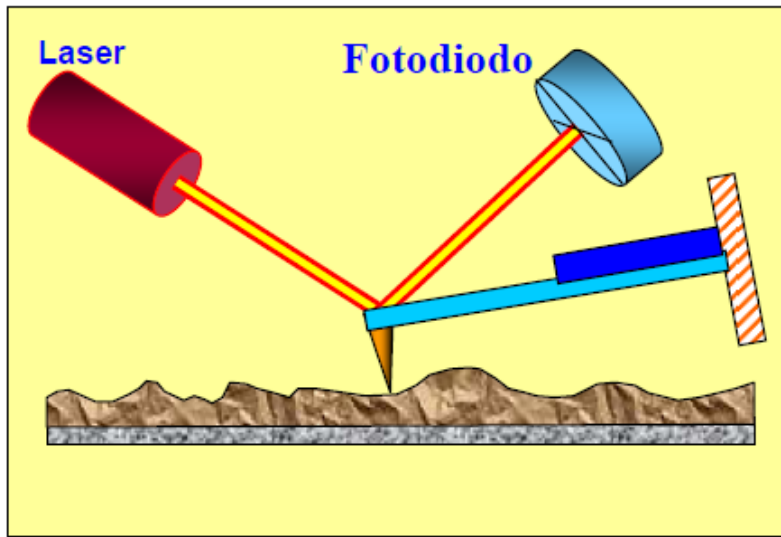
$$B = f(A)$$

F. J. Giessibl, "Advances in Atomic Force Microscopy", Rev. Mod. Phys. 75, 949 (2003)

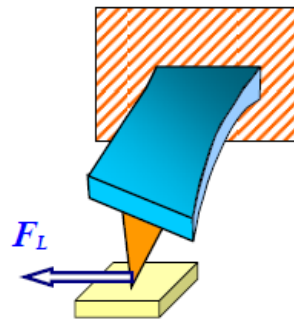


- The probe is actually in contact with the specimen and is physically moved up and down due to the repulsion of van der Waals forces
- As with the STM the probe tip of an AFM must be very small but because there is no need to establish a tunneling current one can use a variety of materials, not just those with a low workfunction.
- The AFM records the position of the probe by bouncing a laser off the back surface of the probe and recording how the light is deflected



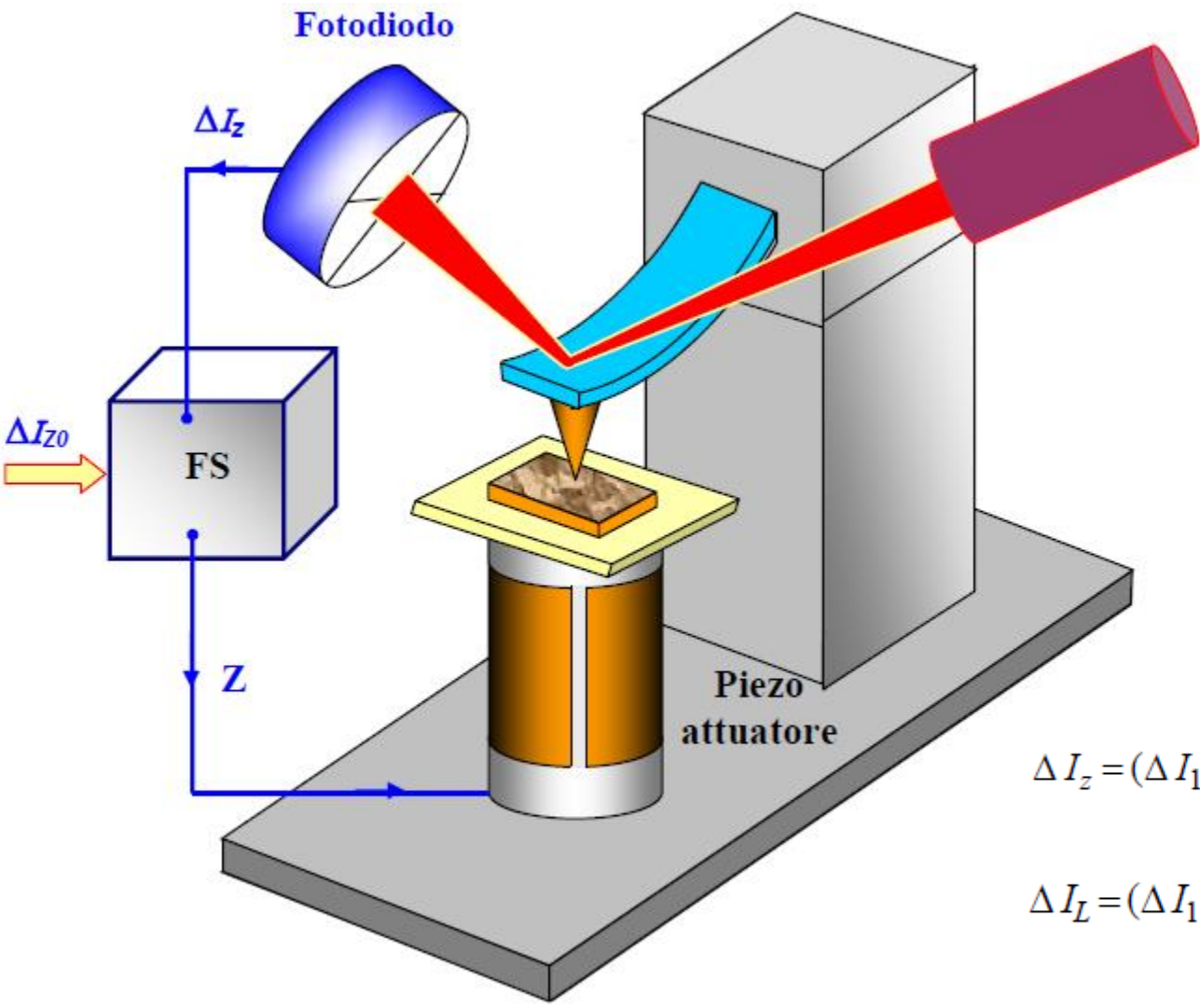


(a)



(b)

Two types of force can be recorded by this configuration: The attractive or repulsive force in the z-direction or the or the lateral force.



ΔI_z is used by the FS:
 FS maintain ΔI_z
 constant by the
 piezoelectric system
 which control the tip-
 sample distance
 variation Δz

$$\Delta I_z = (\Delta I_1 + \Delta I_2) - (\Delta I_3 + \Delta I_4) \longrightarrow F_z$$

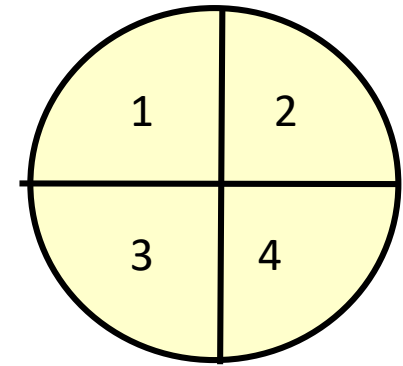
$$\Delta I_L = (\Delta I_1 + \Delta I_4) - (\Delta I_2 + \Delta I_3) \longrightarrow F_L$$

$$V(z) = -E_B \left(2 \frac{z^6}{z_0^6} - \frac{z^{12}}{z_0^{12}} \right)$$

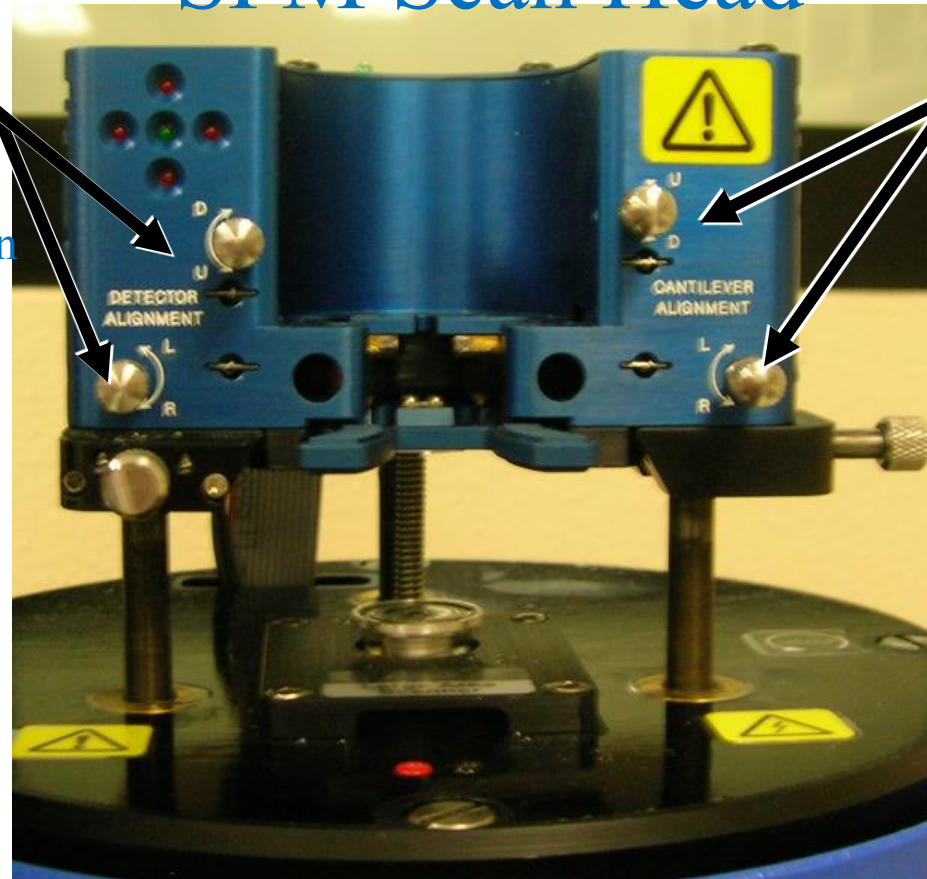
By using a four quadrant detector the relative amount of laser light hitting each quadrant can be used to determine how the tip has been deflected as it moves over the surface of the specimen



Photodetector



SPM Scan Head

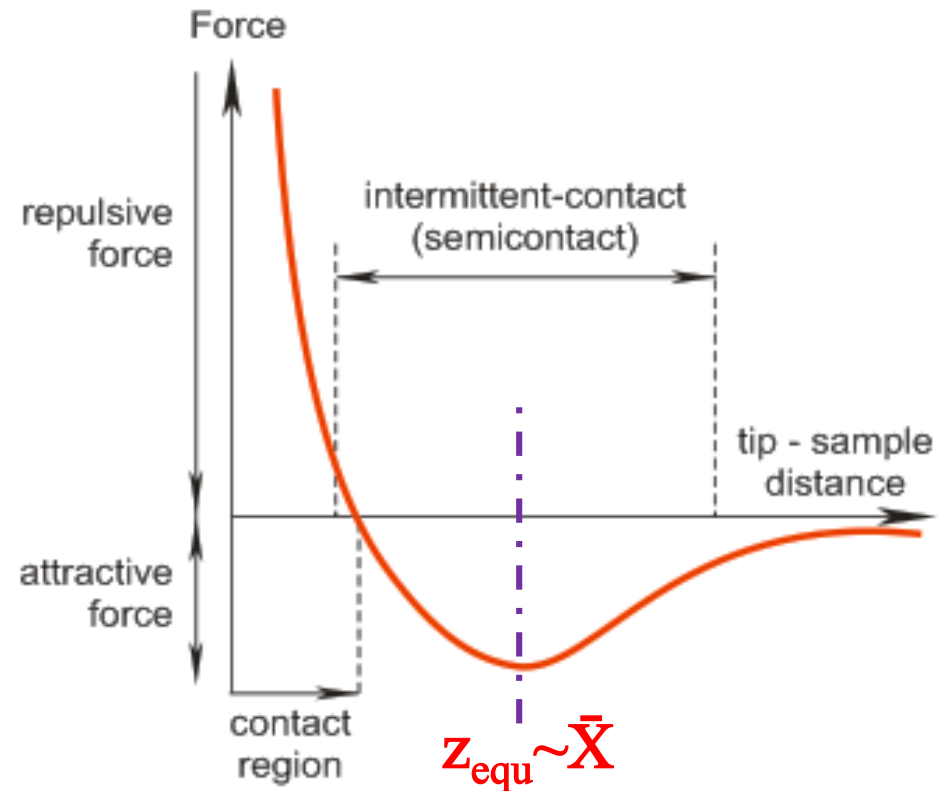
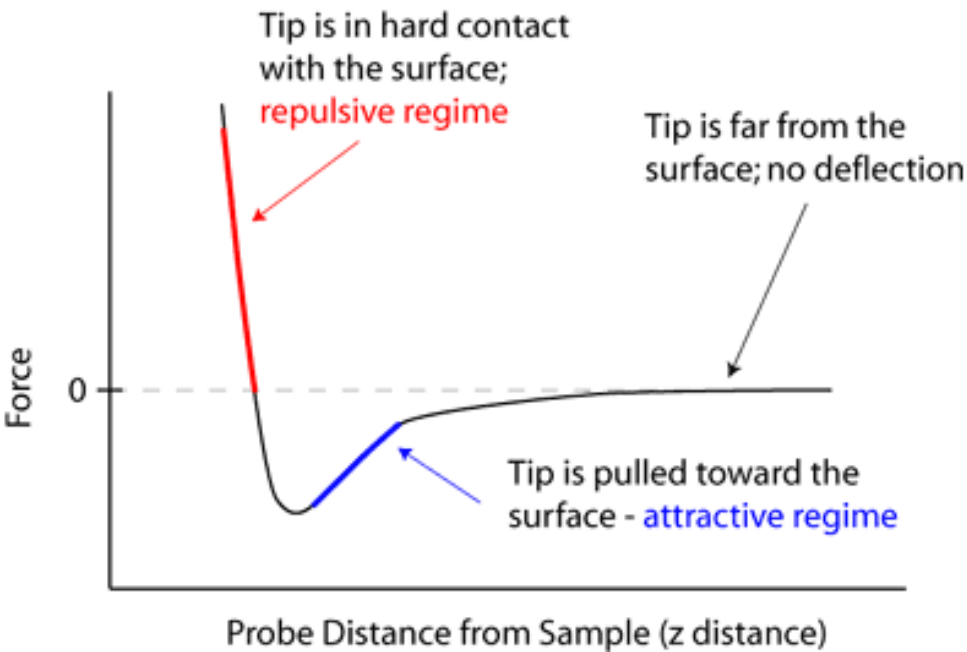


Second:
Adjust detector alignment until red lights are out and green light is on.

First:
Adjust cantilever alignment so laser is aligned on the cantilever



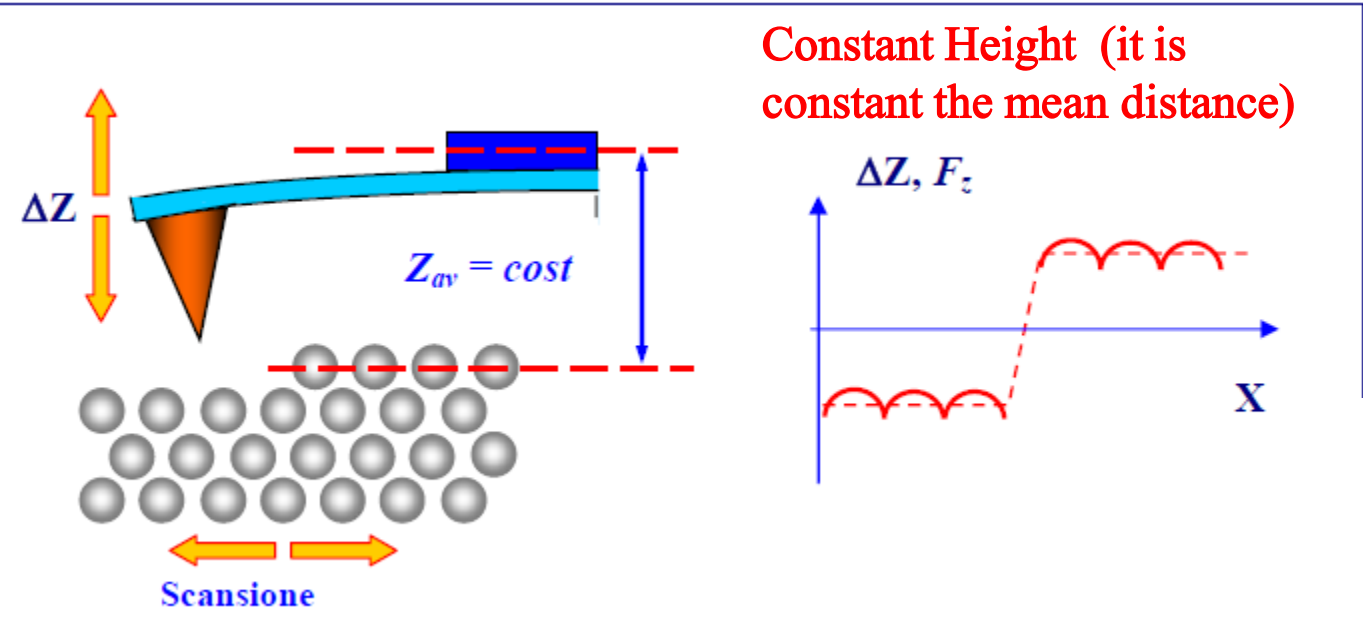
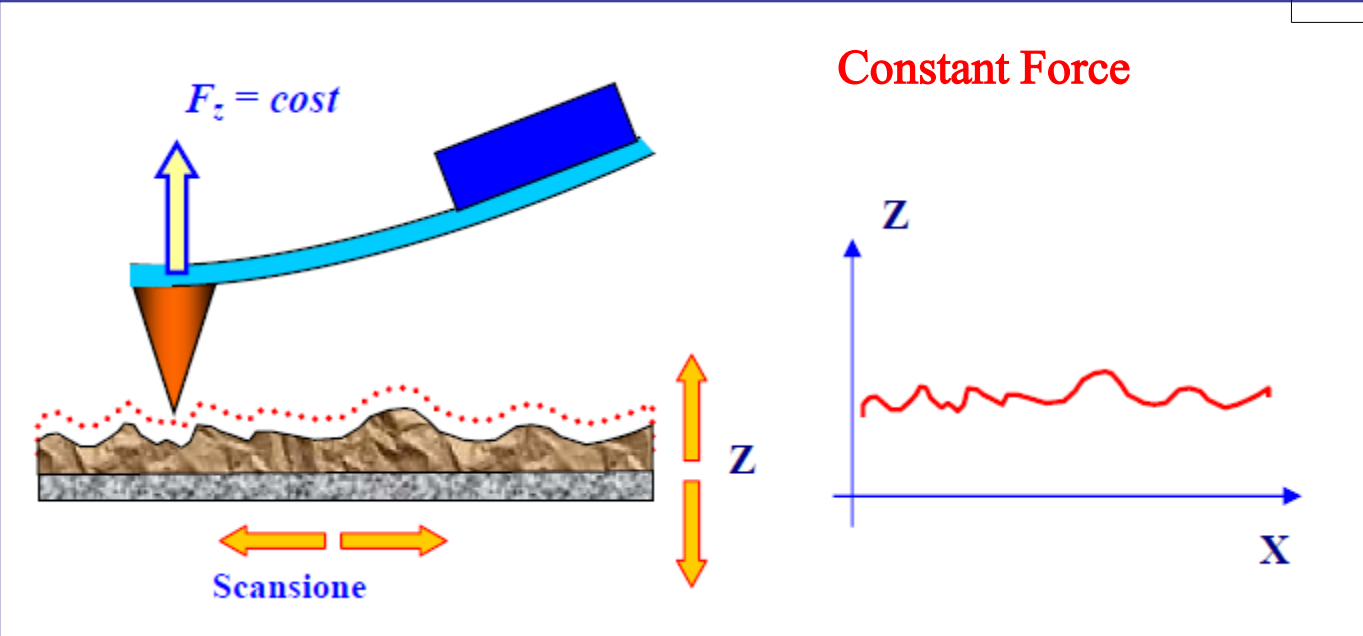
4.2) Operation modes



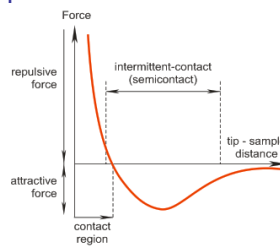
Contact mode

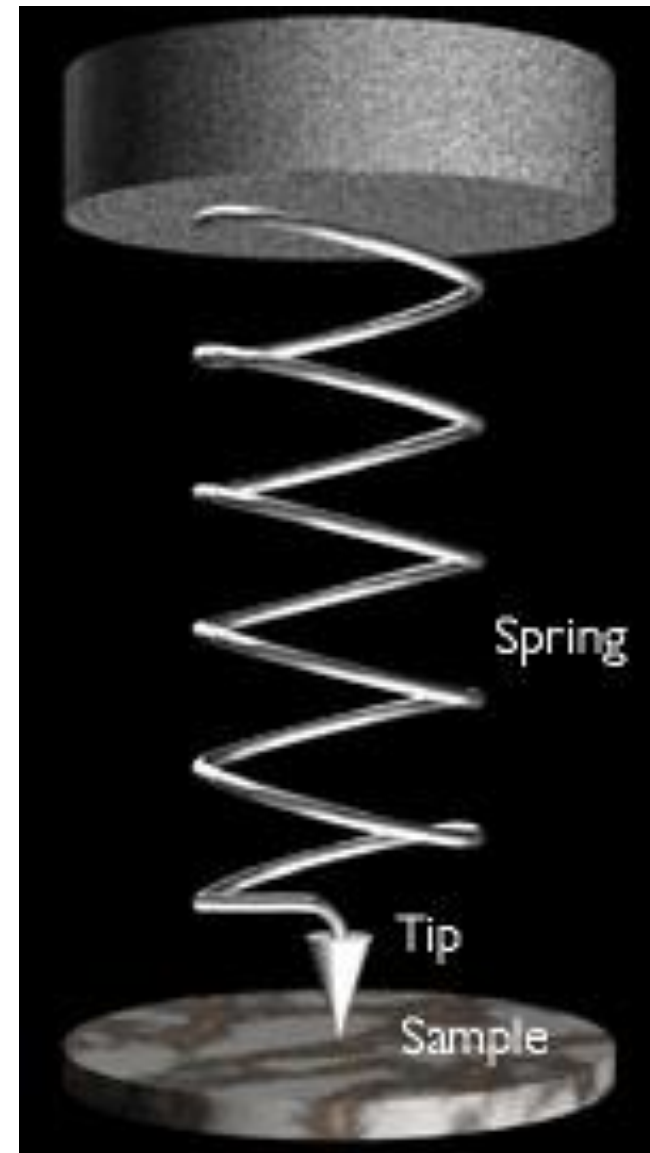
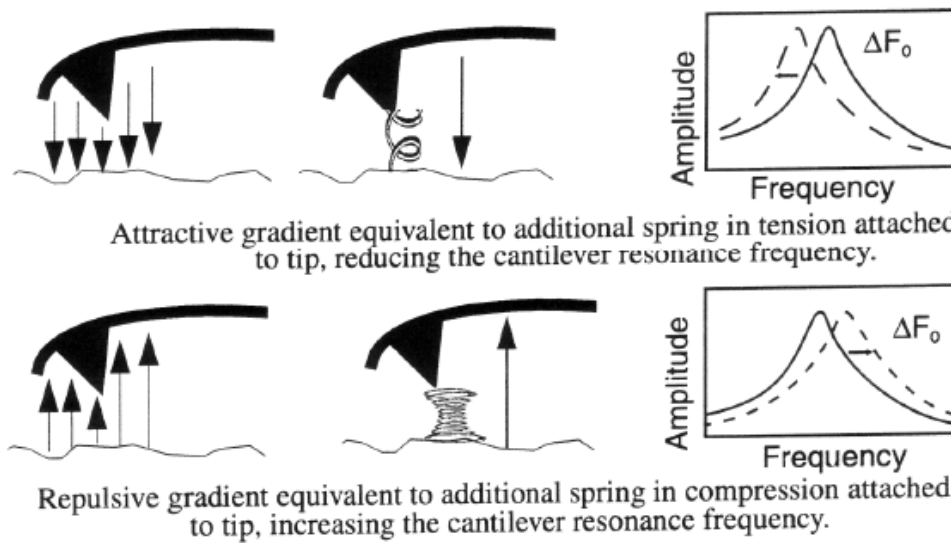
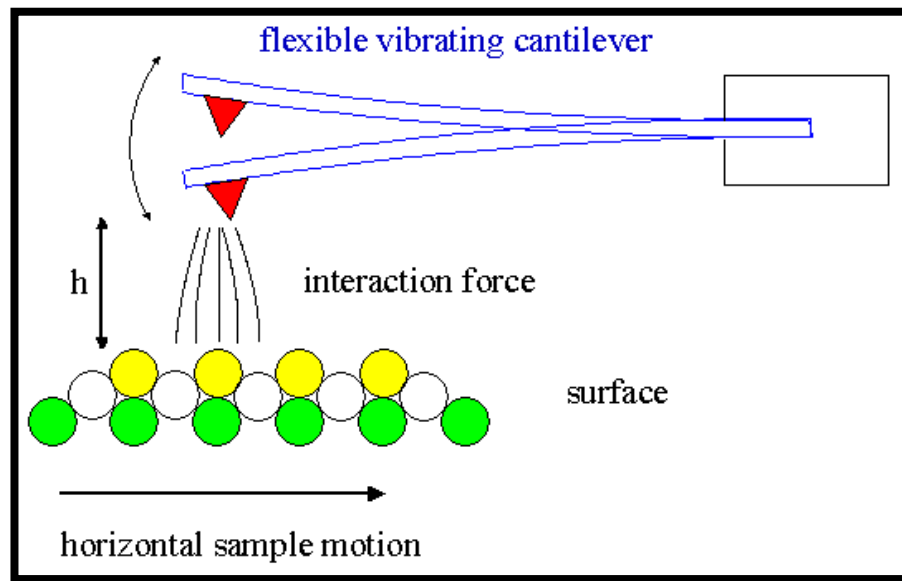


The direct mechanical interaction between tip and surface can induce a damage of the tip or sample surface. So, this mode is often unsuited for soft, organic and biological samples. In this case the non-contact mode is used.

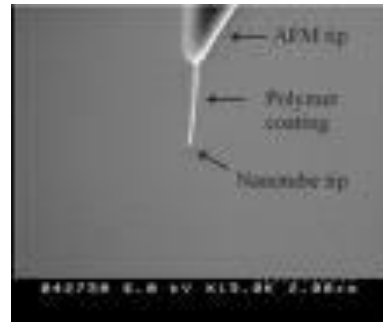
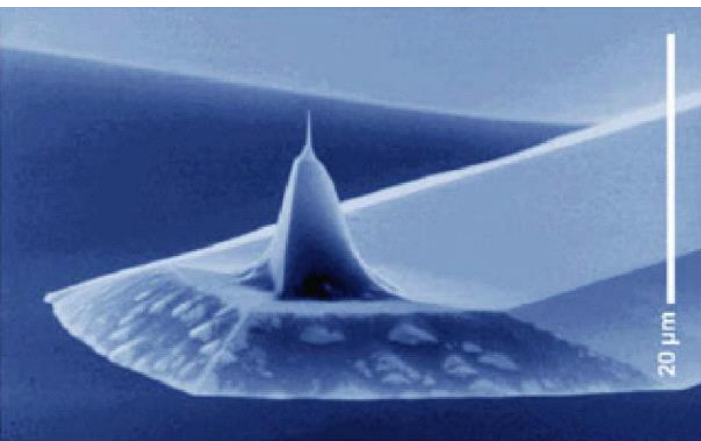
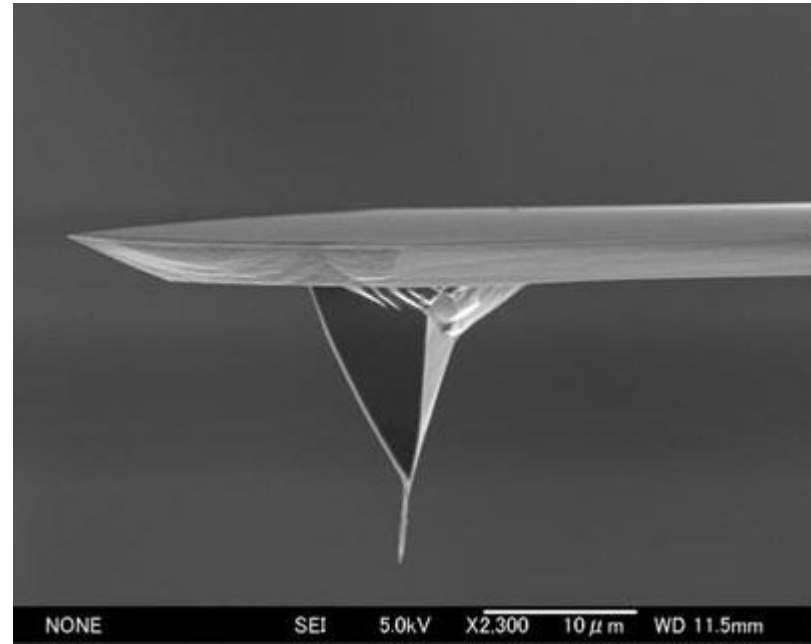
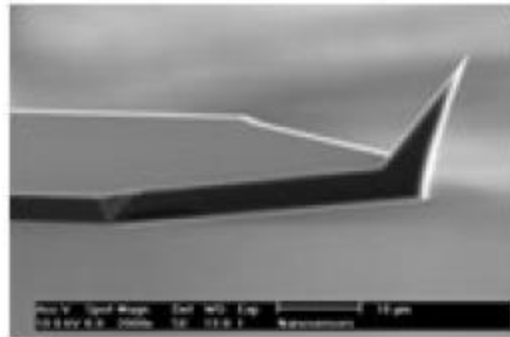
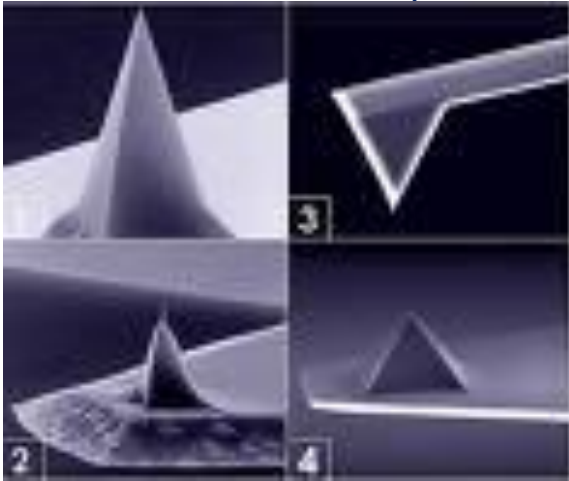


non-contact_mode_en_n.swf





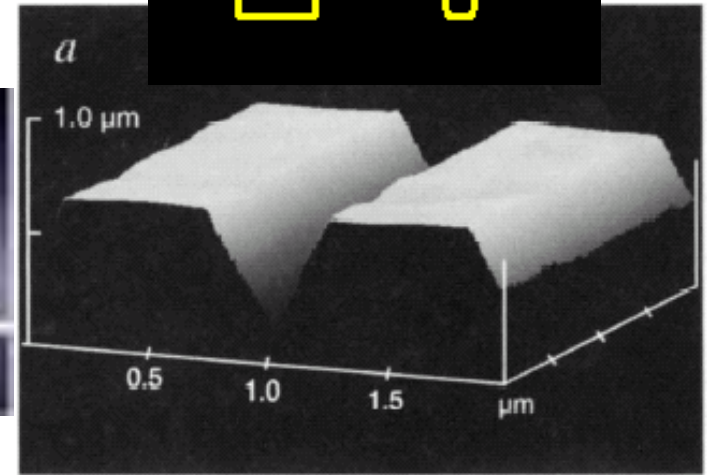
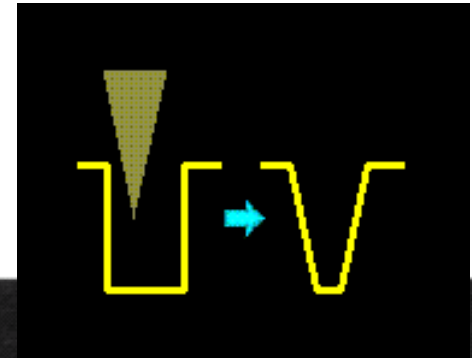
4.3) AFM cantilevers and tips



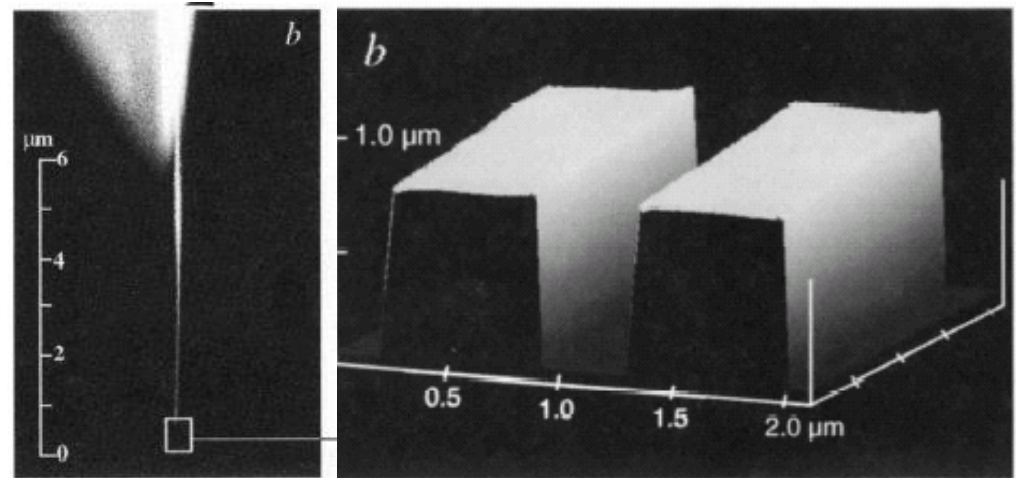
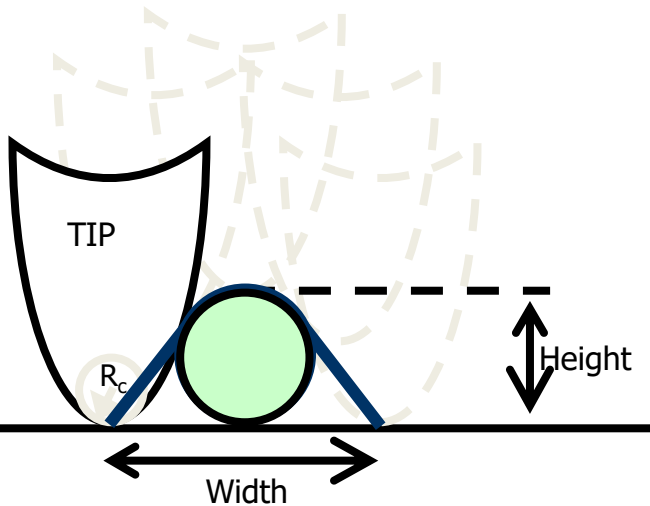
Influence of the tip shape and dimension



ProbeSimulator.exe

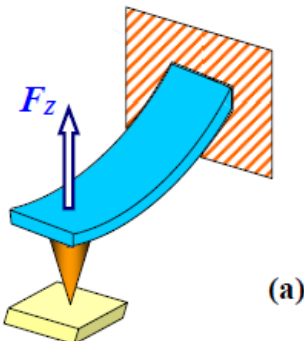
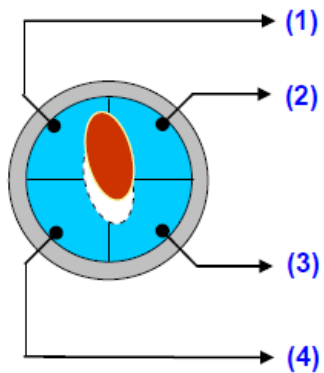
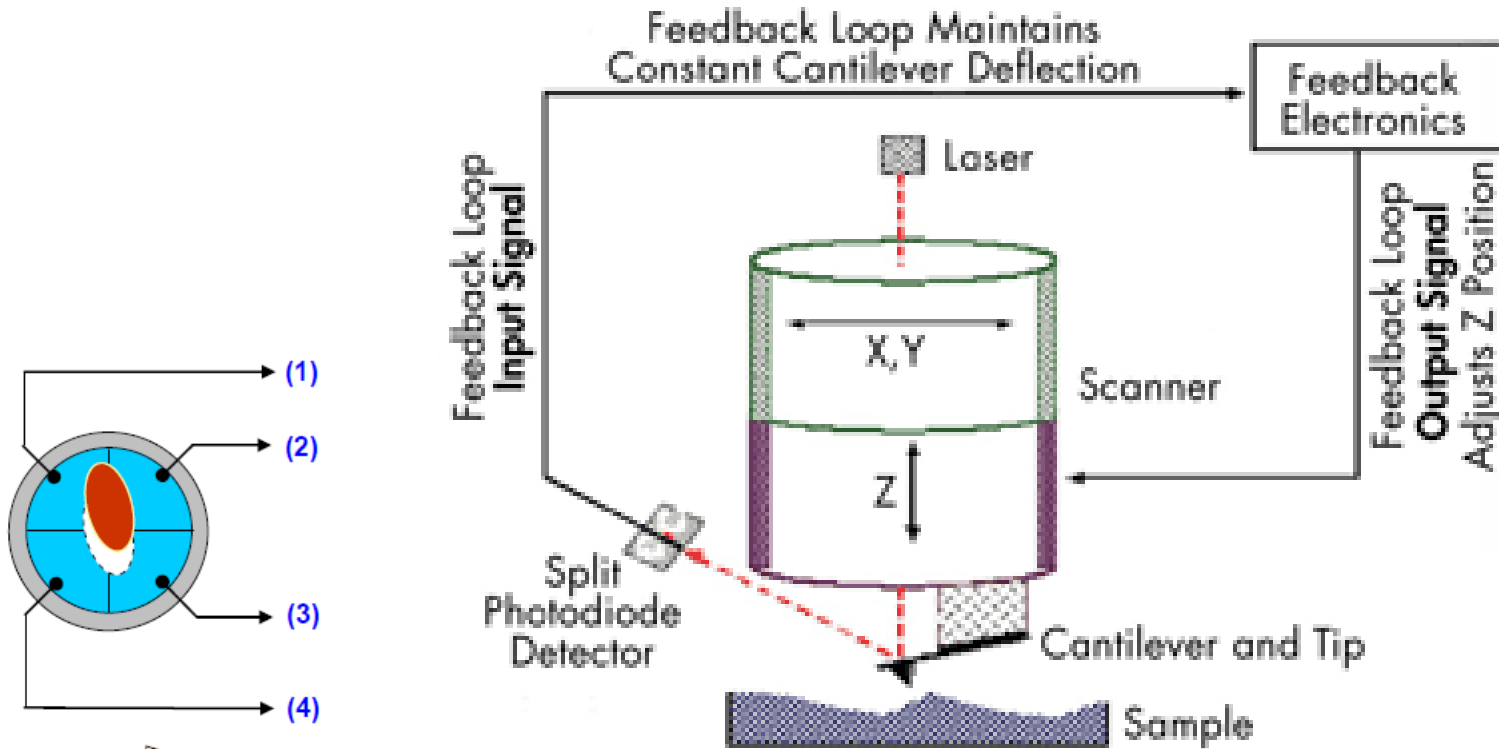


Imaging direction \longrightarrow



4.4) AFM Applications

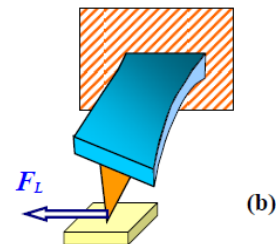
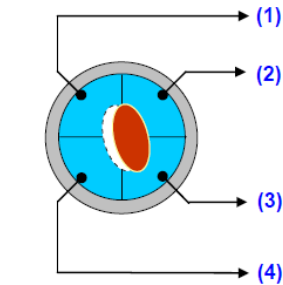
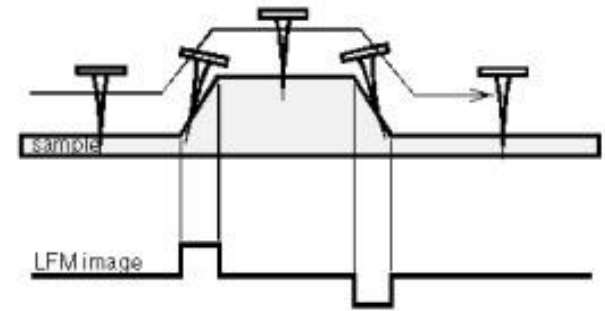
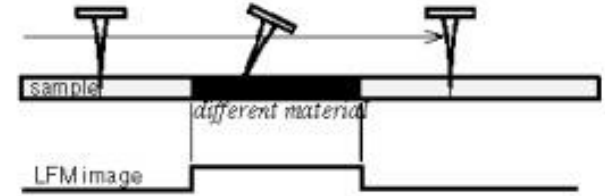
a) High resolution (atomic) topography: Contact and Non-contact



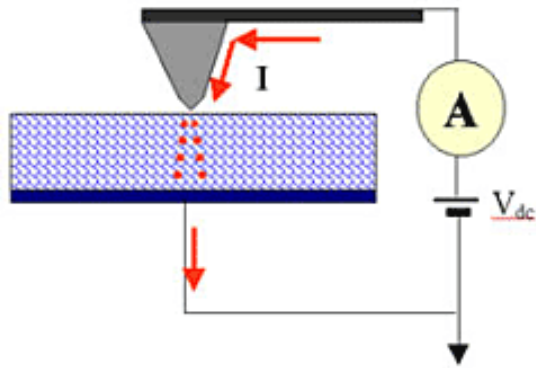
b) Lateral Force Microscopy (or Phase Imaging)

- Lateral Force Microscopy (LFM) is a secondary contact AFM mode that **detects and maps relative differences in the frictional forces** between the probe tip and the sample surface. In LFM, the scanning is always perpendicular to the long axis of the cantilever. Forces on the cantilever that are parallel to the plane of the sample surface cause twisting of the cantilever around its long axis. This twisting is measured by a quad-cell Position Sensitive PhotoDetector (PSPD).

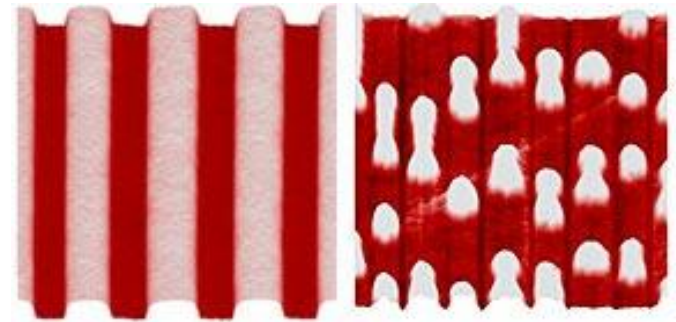
- This mode goes beyond topographical data to detect variations in composition, adhesion, friction, viscoelasticity, and other properties, including electric and magnetic. Applications include contaminant identification, mapping of components in composite materials, differentiating regions of high and low surface adhesion or hardness and regions of different electrical or magnetic properties.



c) Conductive Atomic Force Microscopy

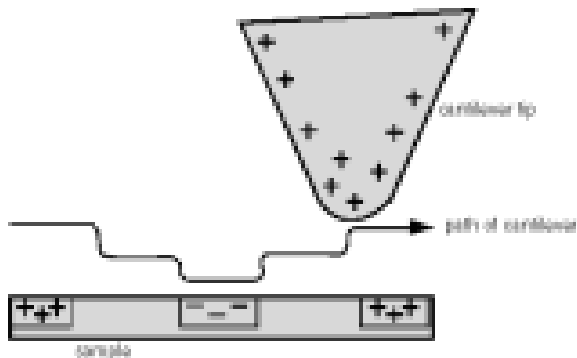


d) Surface Potential Microscopy

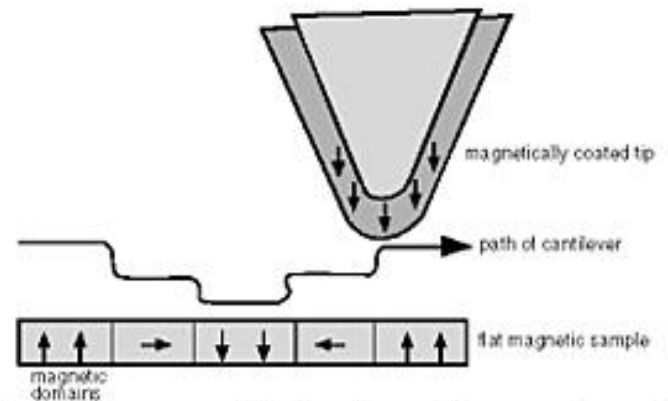


Tapping Mode Topography (left) and Surface Potential (Right) images of an area on a CD-RW. The bits are depicted only in the Surface Potential image. 5 μ m scans

e) Electric Force Microscopy

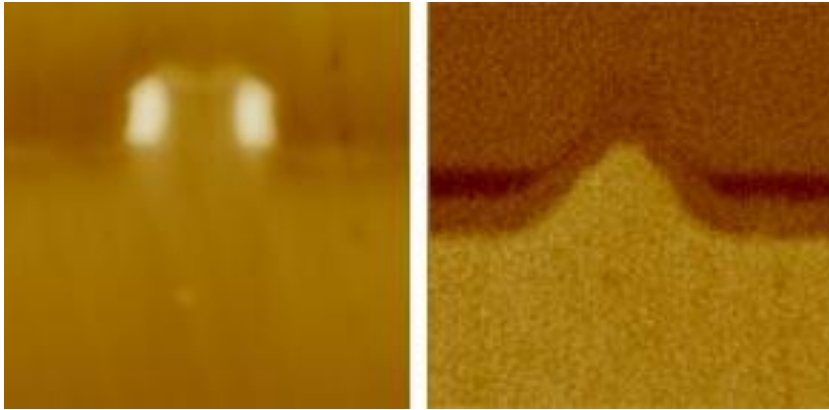


f) Magnetic Force Microscopy



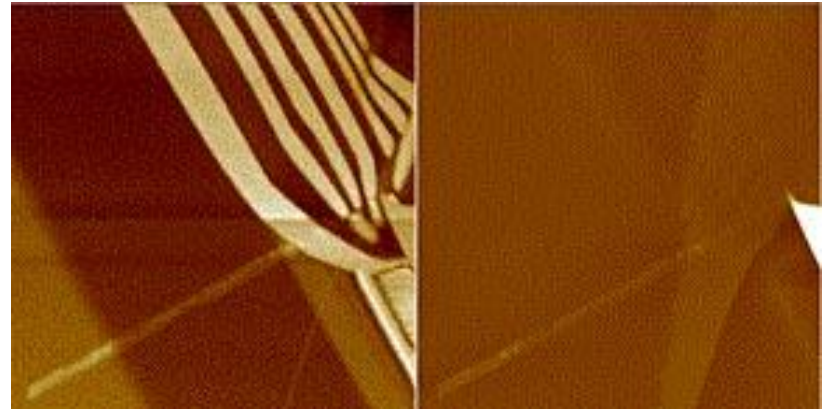
MFM maps the magnetic domains of the sample surface.

g) Scanning Capacitance Microscopy



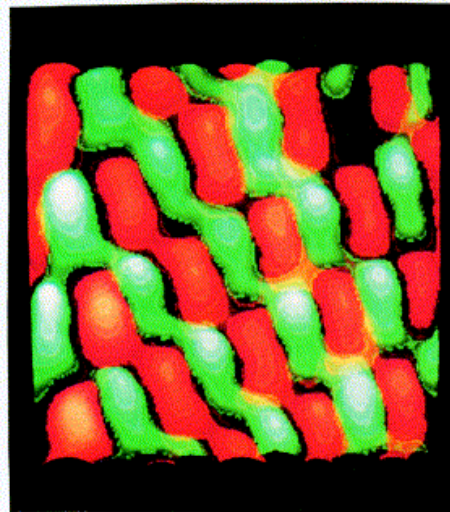
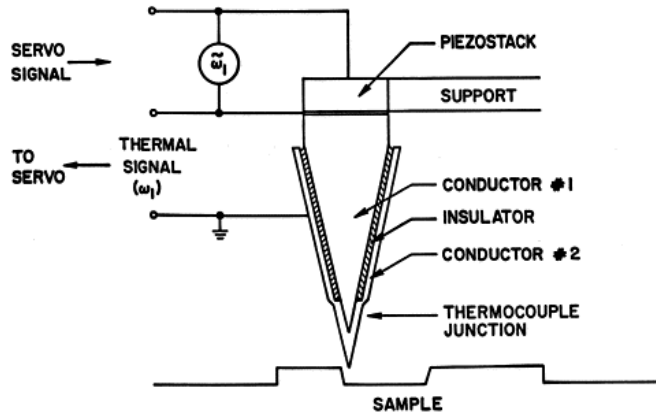
Contact Mode topography (left) and SCM dC/dV images of a cross-sectioned transistor in a Pentium-II chip. 1.25 μ m scans.

h) Scanning Spreading Microscopy



SSRM (left) and contact mode topography (right) scans of an InP based heterostructure. 7 μ m scans. The contrast in the SSRM image shows the different regions of the heterostructure: alternating Zn-doped p-type and S-doped n-type layers.

i) Scanning probe thermal microscopy



3.4) AFM Advantages & Disadvantages

- The piezoelectric tubes have a movement resolution of 1 nm/volt (Resolution of 10 pm).
- Can operate in air and under liquids
- Atomic force microscopes can be used on many different surfaces (conductive, non-conductive, hard, soft,....)
- AFM is a versatile tool.
- In all three resolution is largely dependent on probe size and the ability to control scanning.
- AFM is, mainly, a surface technique.



Watch the AFM tip at work, with the DME BRR, a fully integrated hybrid SEM AFM system.mp4

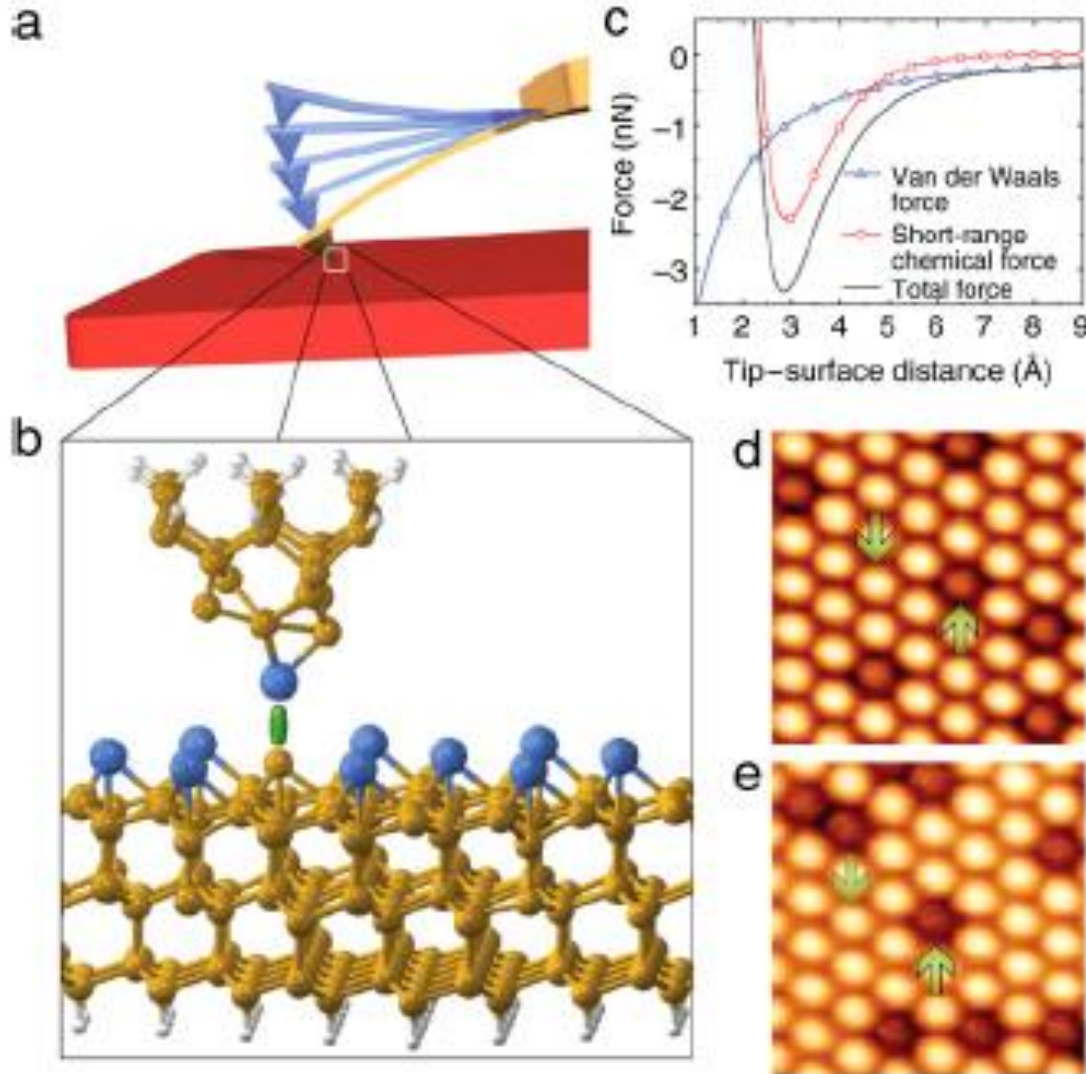
<http://www.youtube.com/watch?v=yvZleHfF364>

Part 2: Applications to Nanoscale Characterization of Surfaces and Interfaces

- Materials and manufacturing
- Nanoelectronics and computer technology
- Medicine and health
- Aeronautics and space exploration
- Environment and energy
- Biotechnology and agriculture
- National security and other government applications
- Science and education
- Global and trade competitiveness

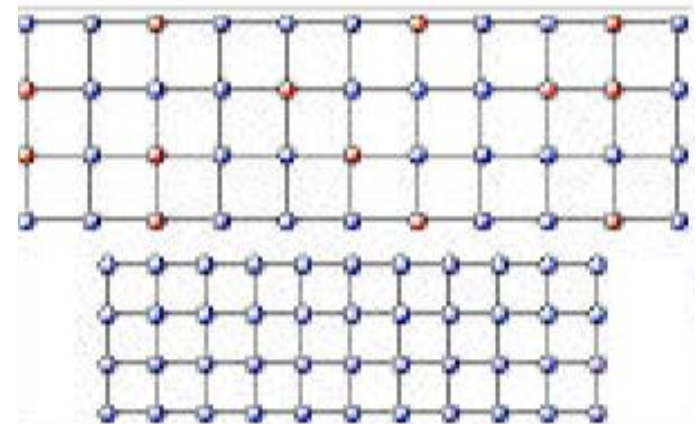
1) “Physical Applications”

a) Atomic resolution imaging of metal, semiconductors and insulator surfaces

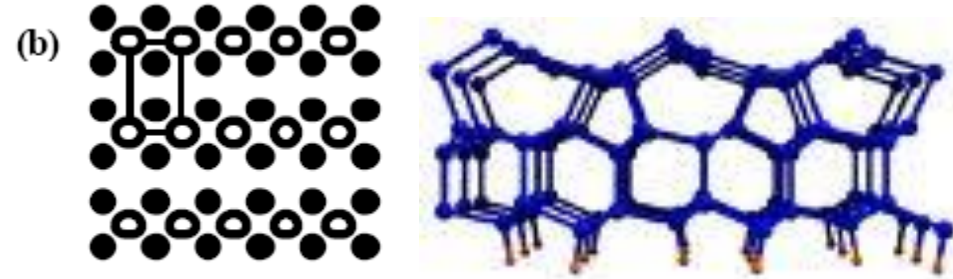
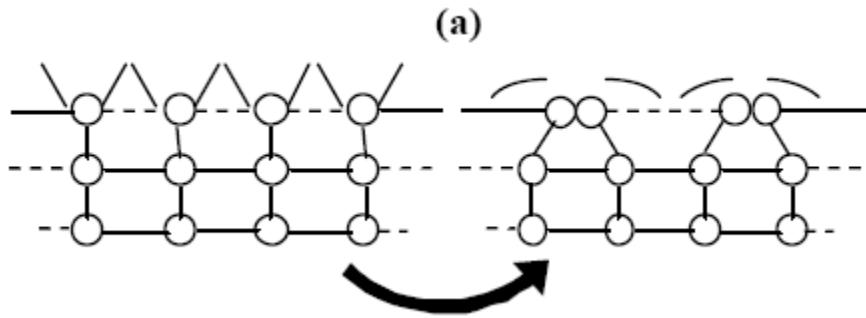


Atom recognition using AFM:

(a) Schematic illustration of the dynamic AFM; (b) The atomic contrast originates from the chemical bonding between the outermost tip atom and the surface atom; (c) Force curves showing the calculated vdW force, the measured short-range chemical force and the total force. (d) The topographic image of a single atom layer of Sn grown over a Si (111) substrate. The Pb layer. The diminished topographic contrast indicate substitutional Si defects. Image size 4.3 nm.

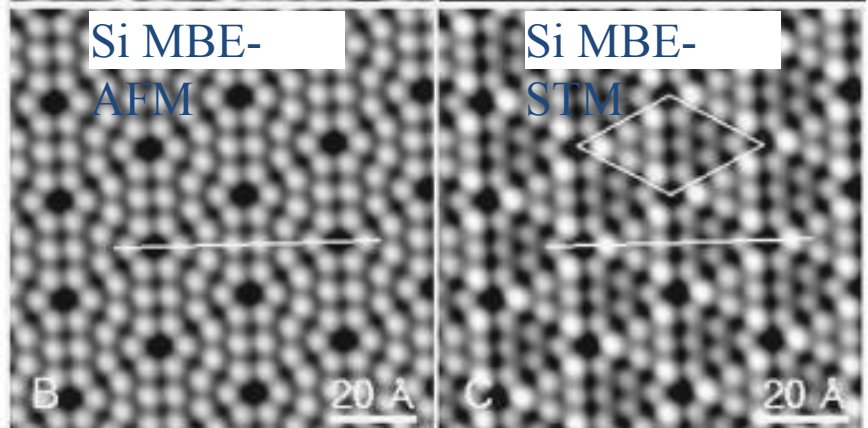
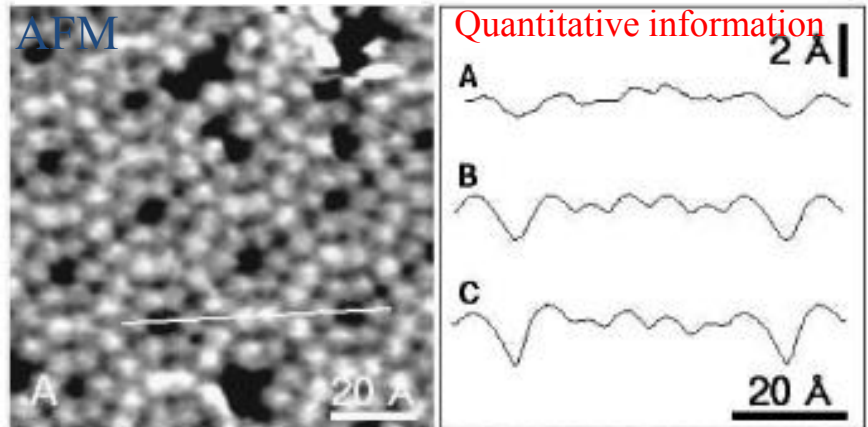
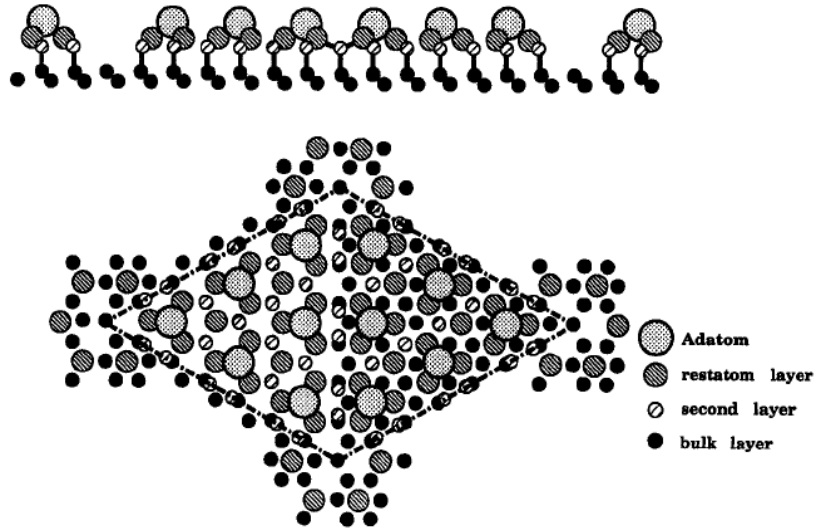


2x1 reconstruction of Si(001)



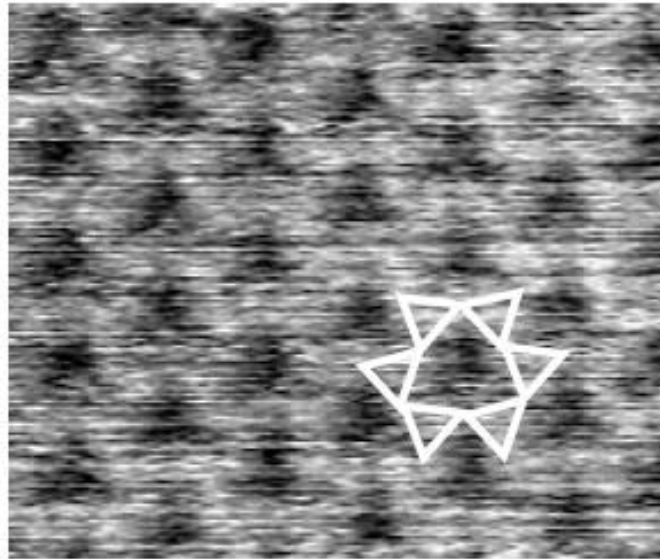
7x7 reconstruction of Si(001)

Commercial Si-AFM



1 monoatomic layer of Ag on Si(111)

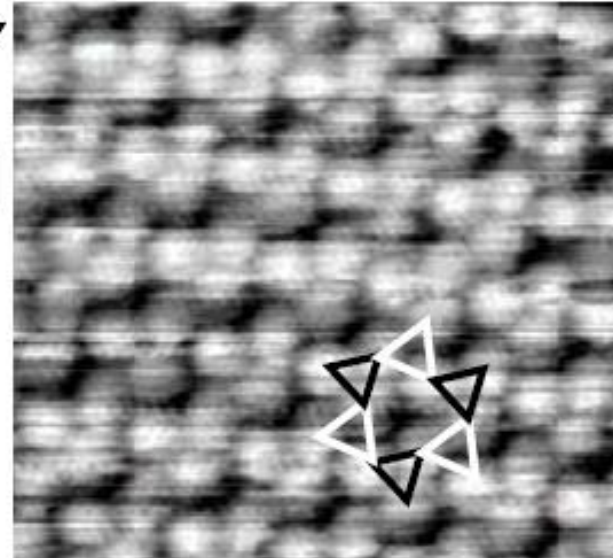
RT(Room Temperature)



1nm

(a)

LT(Low Temperature)

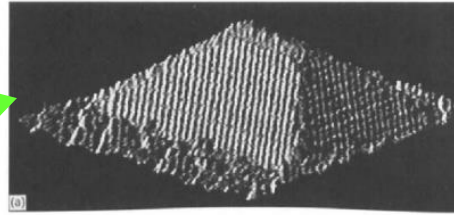
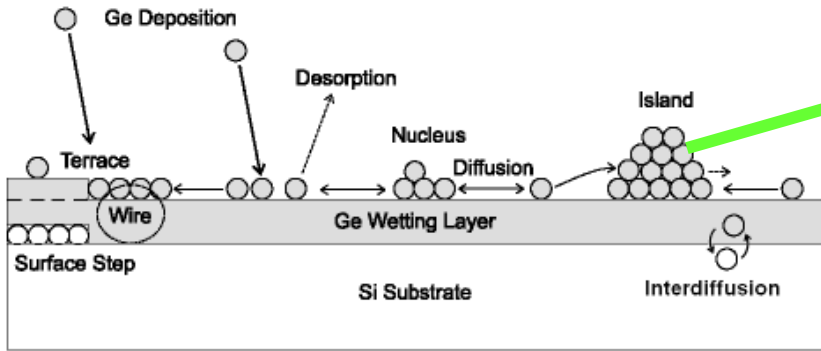


6K

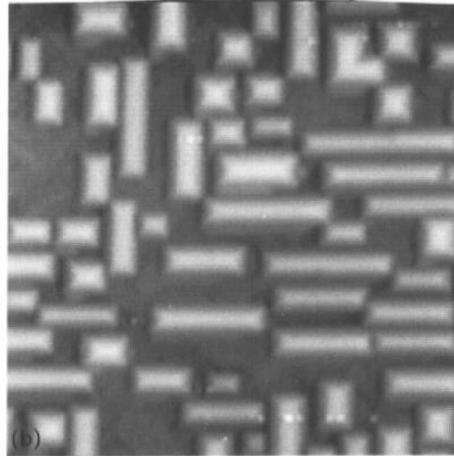
4.3nm×4.3nm

(b)

b) Imaging of nanostructures on surfaces



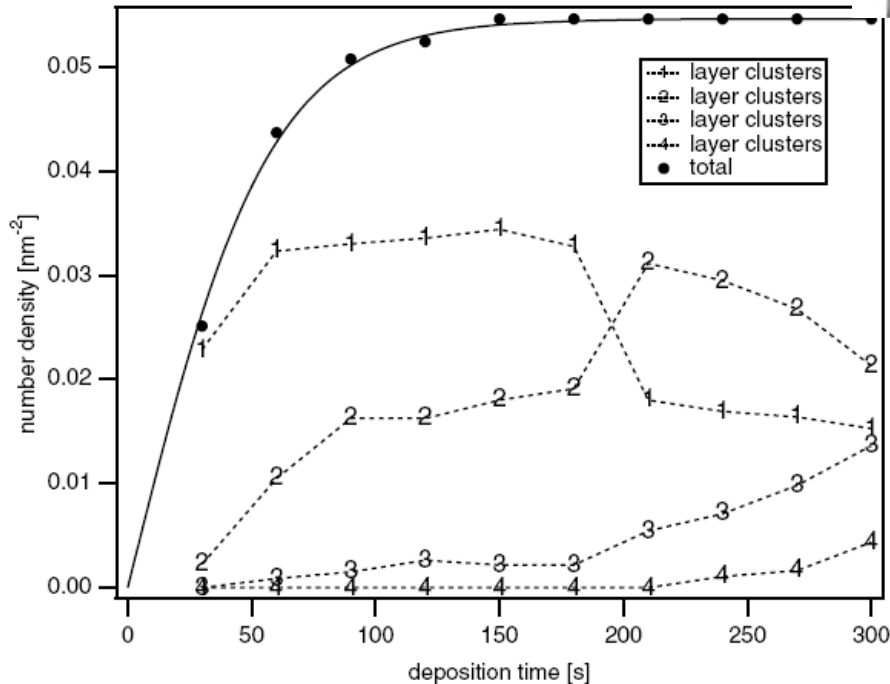
Ge on Si
STM: 40x40 nm



Ge on Si
STM: 250x250 nm

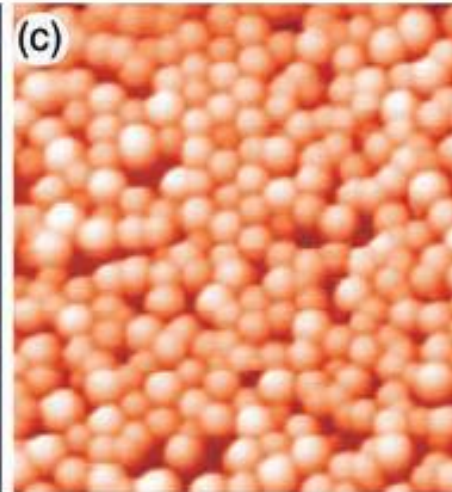
K. S. Birdi, Scanning probe microscopes: application in science and technology, CRC Press 2003

Quantitative information

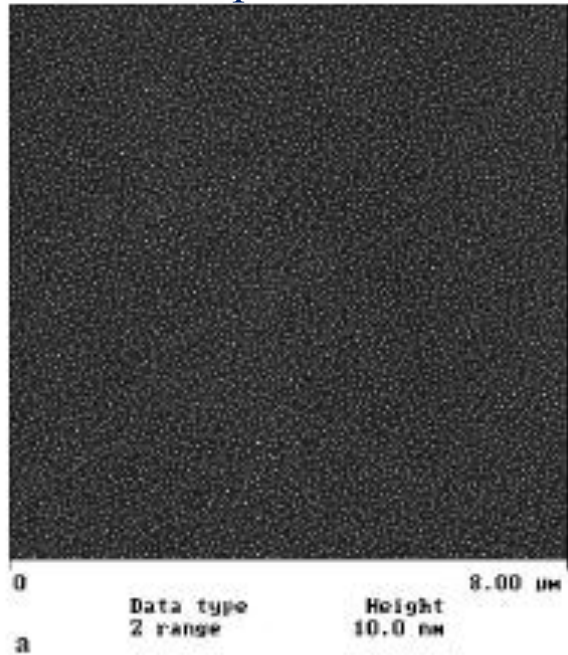


in
im

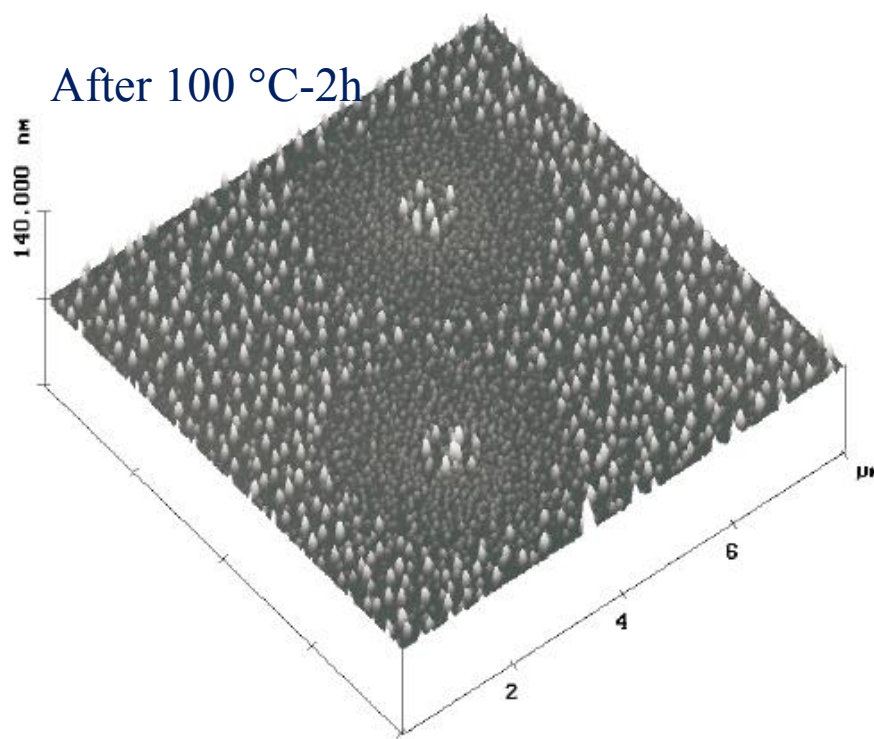
Au clusters on
 Al_2O_3 80x80 nm



Au as-deposited on Si



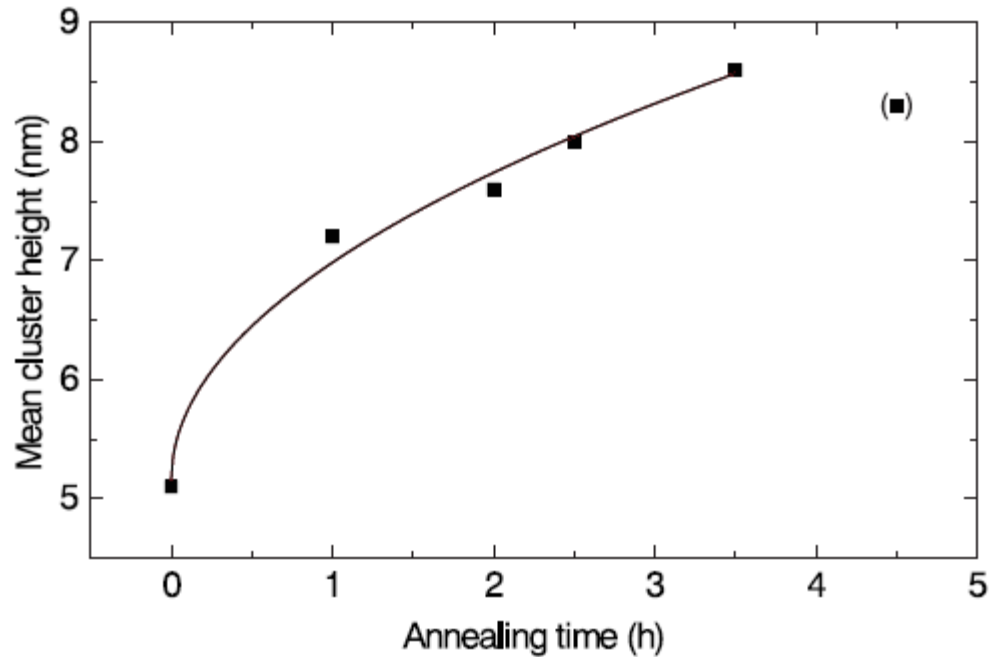
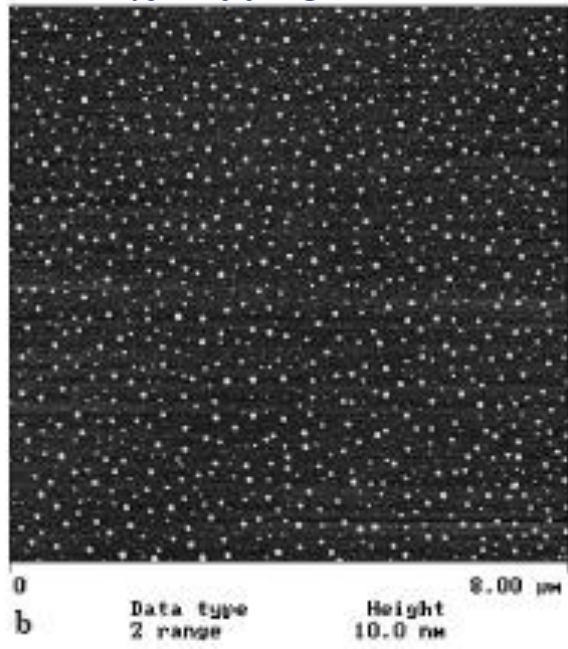
After 100 °C-2h



AFM study of dynamic kinetics of nanostructures on surfaces

*T.F. Young et al.,
Thin Solid Films
322, 319 (1998)*

After 100 °C-1h



c) Probing nanoscale electrical properties and single electron phenomena

Electric probe of quantum confined systems



I(V)_spectroscopy_en_n.swf

$$I=VG$$

Macroscopic physics (macroscopic electron transport)



I(z) Spectroscopy_en_n.swf

$$I \sim VG$$

$$G = (2\pi / h)T$$

Mesoscopic physics (nanoscopic electron transport)

E. Bar-Sadeh et al., Phys. Rev. B 50, 8961(R) (1994)

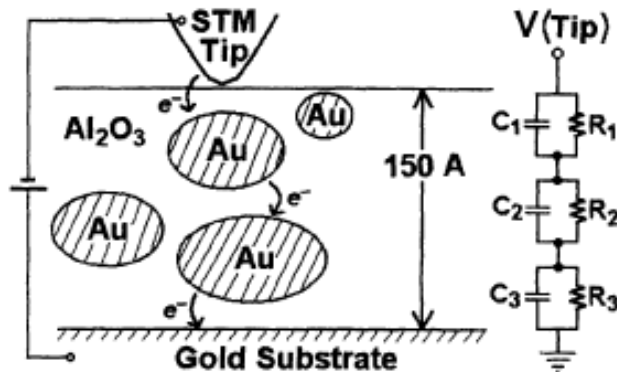
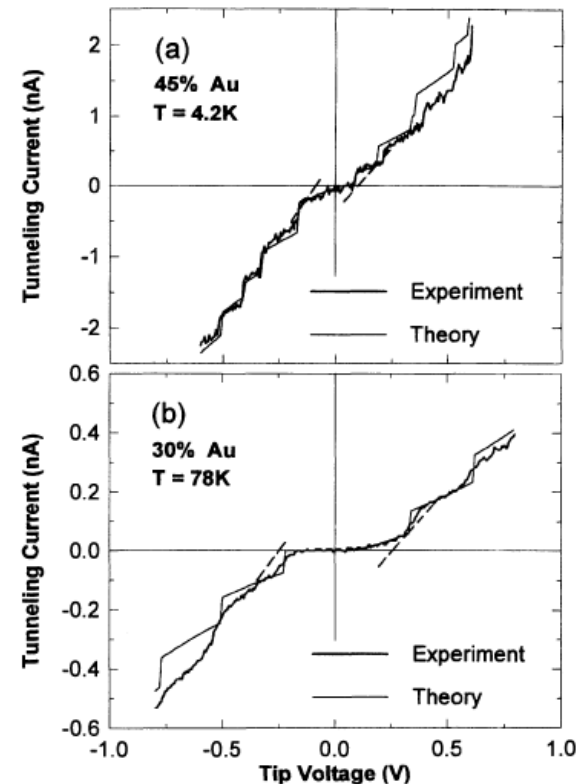
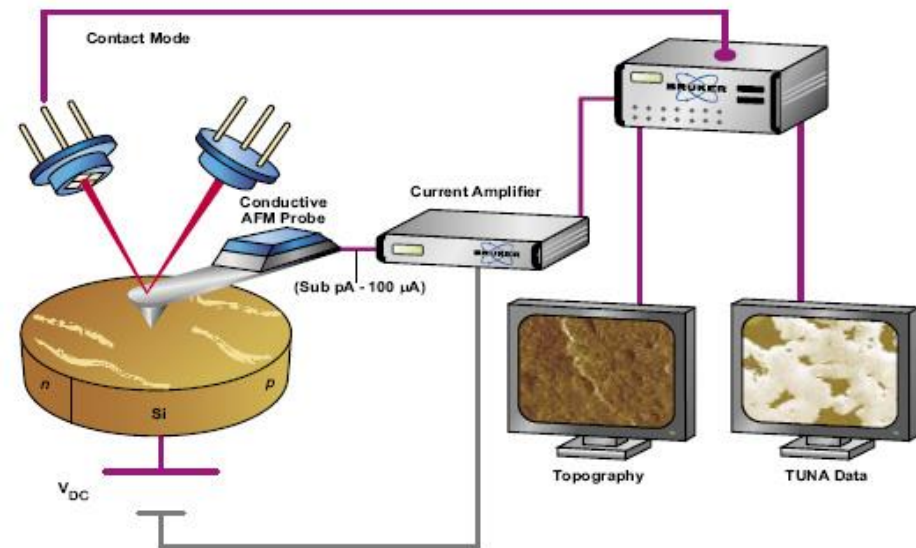
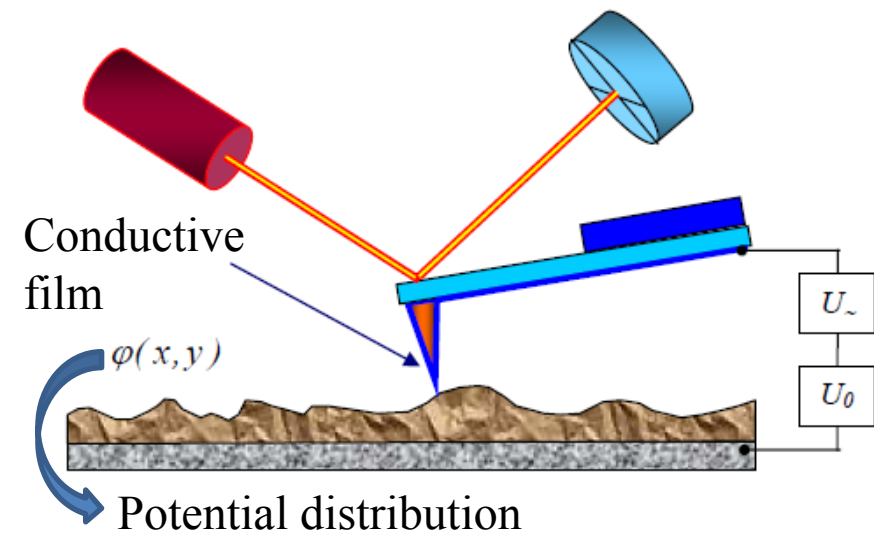


FIG. 1. A schematic of the experimental setup; a granular Au/Al₂O₃ film sandwiched between a STM tip and a metal substrate. A tunneling path across a triple-barrier tunnel junction is indicated by arrows. The equivalent electrical circuit is shown to the right.



Conductive AFM (C-AFM)



$$U = U_0 + U_1 \cdot \sin(\omega t) - \varphi(x, y) \quad \text{Potential difference between tip and sample}$$

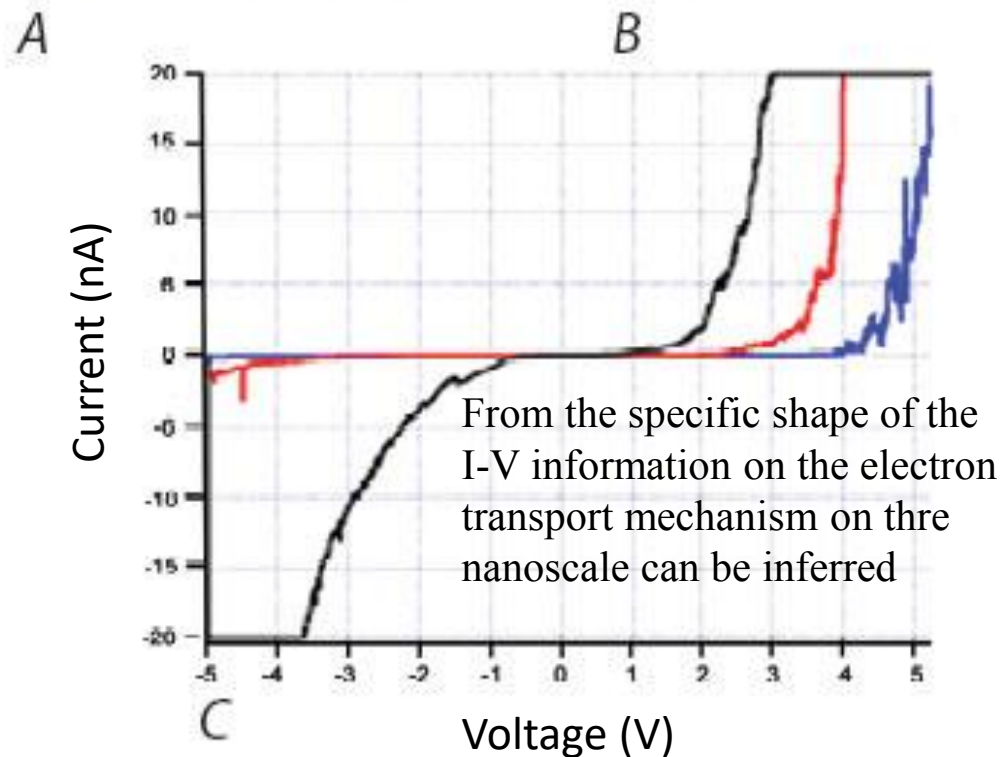
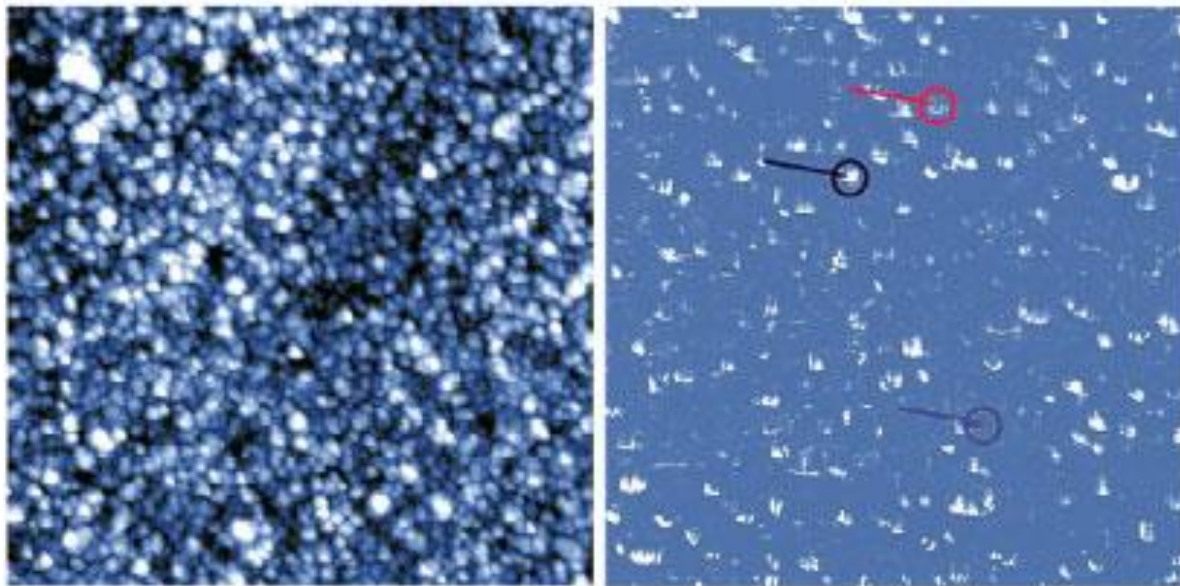
$$E = \frac{CU^2}{2} \quad \text{Electrostatic energy (C=tip-sample capacitance)}$$

$$F_z = -\frac{1}{2} \left\{ [U_0 - \varphi(x, y)]^2 + 2[U_0 - \varphi(x, y)]U_1 \sin(\omega t) + \frac{1}{2}U_1^2 [1 - \cos^2(\omega t)] \right\} \frac{\partial C}{\partial z} \quad \text{Electrostatic force in the z-direction}$$

$$F_{z(\omega=0)} = -\left\{ \frac{1}{2} \left((U_0 - \varphi(x, y))^2 + \frac{1}{2}U_1^2 \right) \right\} \frac{\partial C}{\partial z}$$

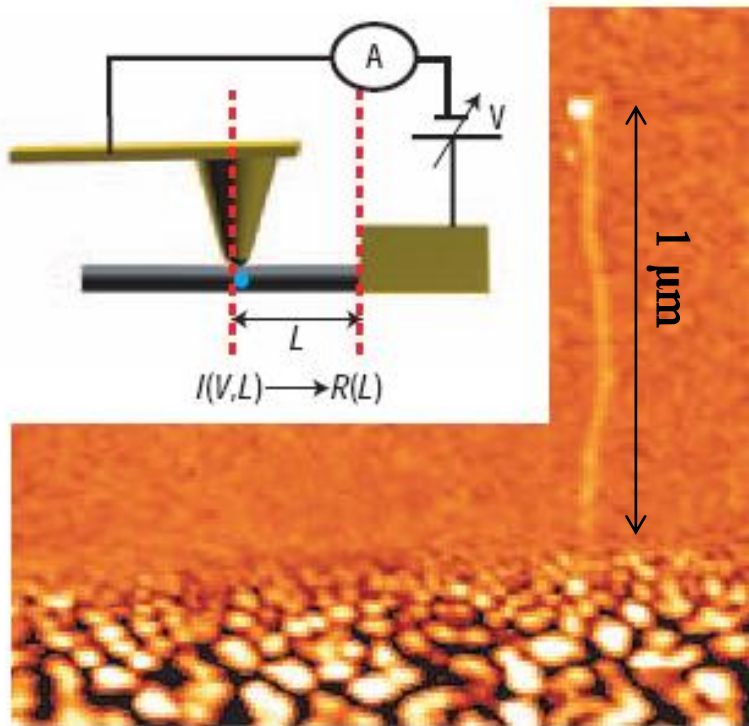
$$F_{z(\omega)} = -\left[(U_0 - \varphi(x, y)) \cdot U_1 \sin(\omega t) \right] \frac{\partial C}{\partial z}$$

$$F_{z(2\omega)} = \left\{ \frac{1}{4}U_1^2 \cos(2\omega t) \right\} \frac{\partial C}{\partial z}$$



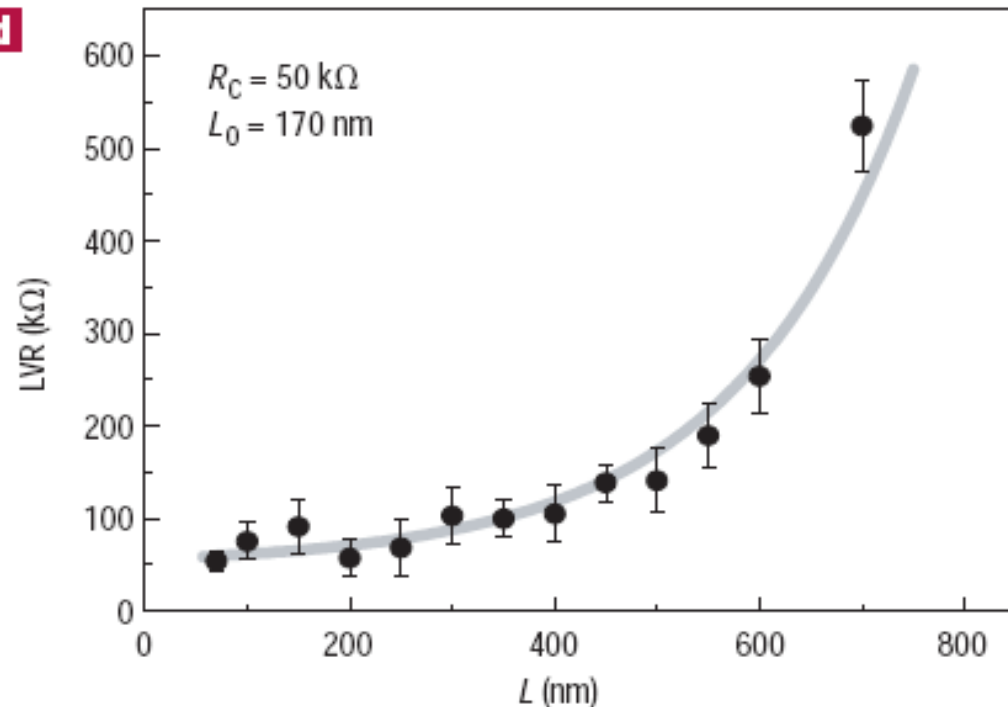
Topography (A) and current (B) image of a Europium-doped ZnO sample at a bias of 1.5 volts, $2\mu\text{m}$ scan. Corresponding IV curves (C) recorded at three specific positions from those indicated in B. The curves are consistent with the current contrast observed in 2B. Specifically, the conductance is highest at the black location, in between at the red, and lowest at the blue.

Electrical characterization of single nanotubes, nanowires and bundles



Resistance scale exponentially with the nanotube length and not linearly as expected by the classical Ohm law

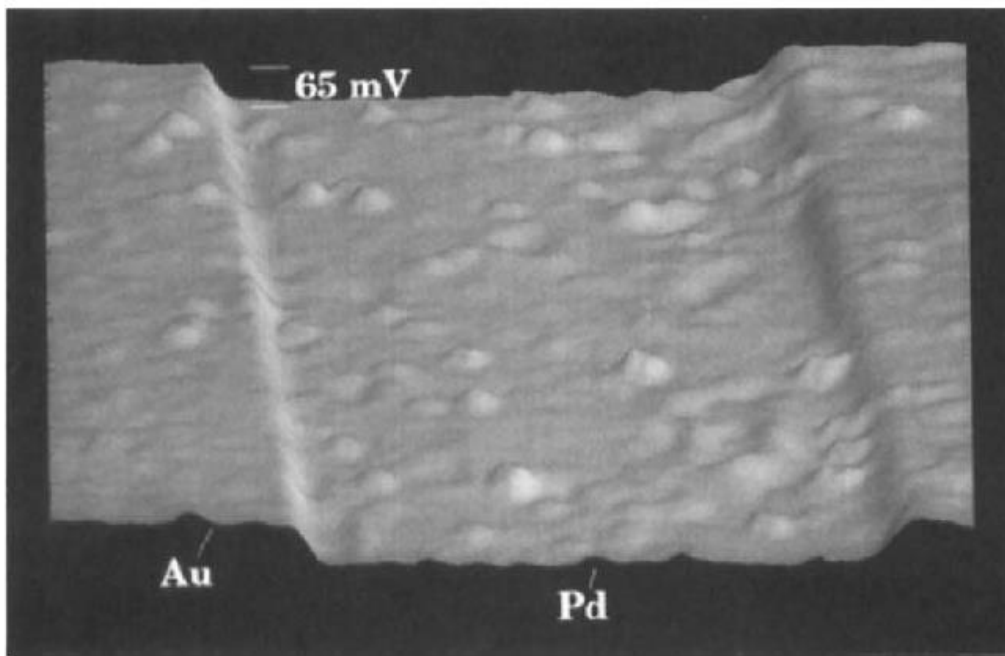
d



B. Biel et al., Phys. Rev. Lett. 95, 266801 (2005)

C. Gómez-Navarro et al., Nature Materials 4, 534 (2005)

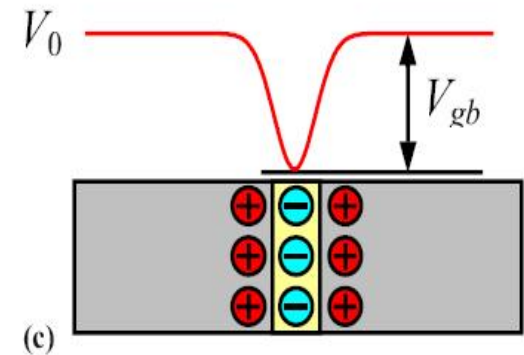
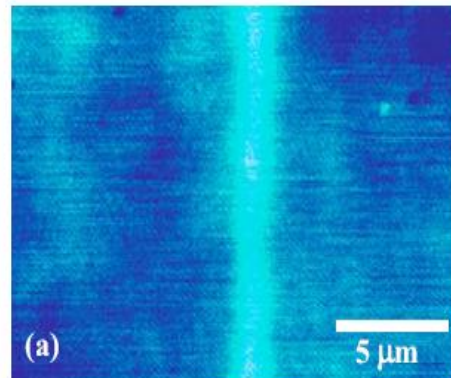
Surface potential imaging



*S. Kalinin, A. Gruverman
(Eds.), Scanning probe
microscopy: electrical and
electromechanical
phenomena at the
nanoscale, Springer 2007*

FIG. 10. Contact potential image of a palladium line on gold showing a 65 mV difference in contact potential between palladium and gold; field of view is $8\ \mu\text{m} \times 6\ \mu\text{m}$.

oxide



Electric_Force_Microscopy_en_n.swf

d) Nanoscale capacitive mapping (scanning capacitance microscopy)

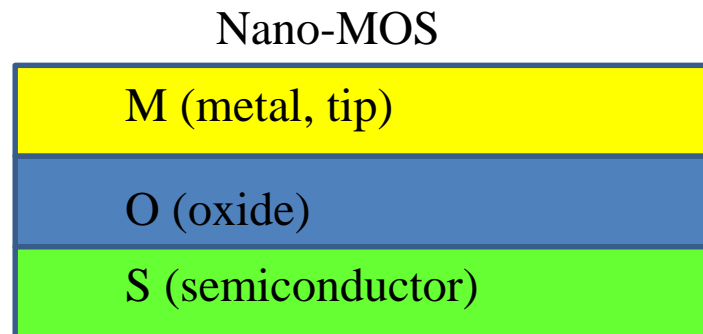
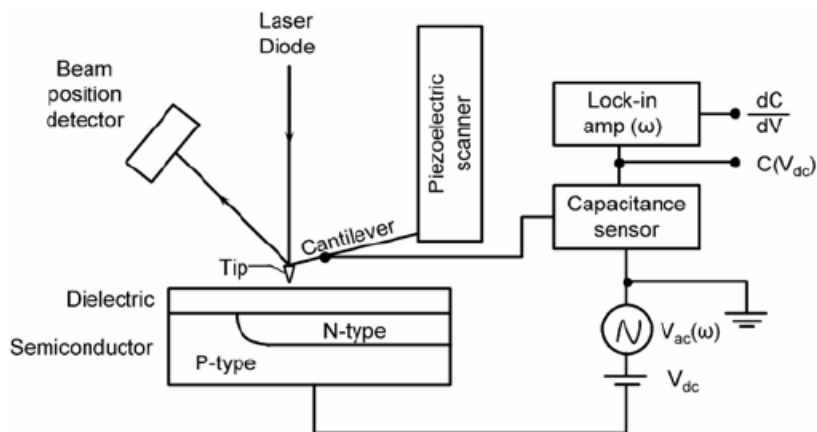
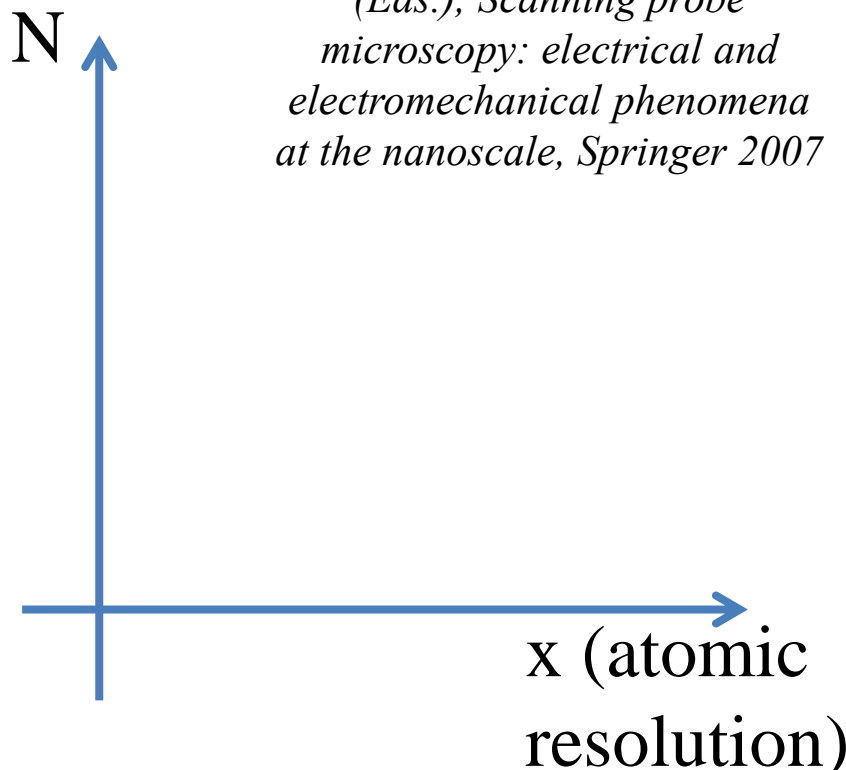
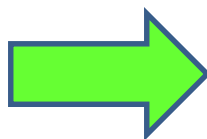
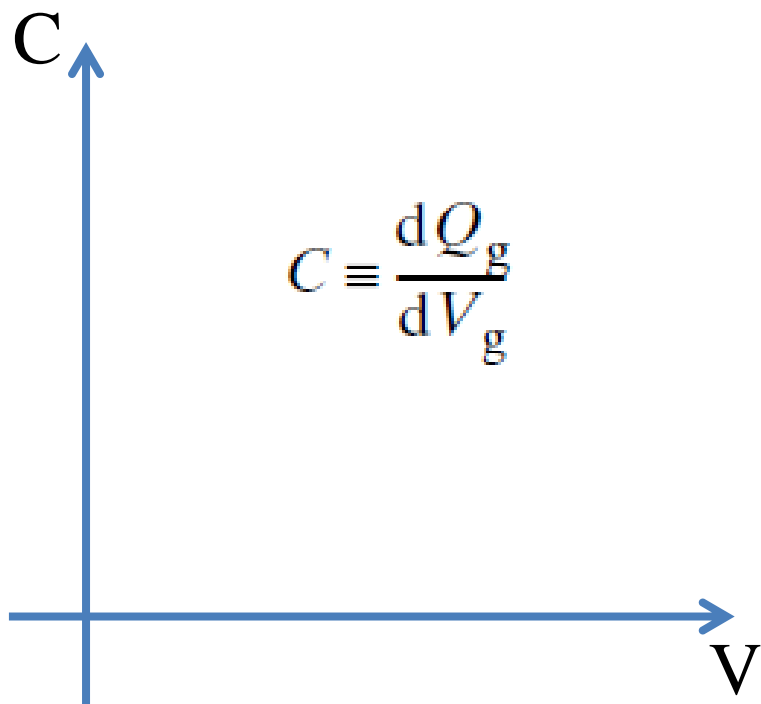


FIGURE 1. Block diagram of a scanning capacitance microscope configured for constant ΔV mode operation [16]. (Copyright American Institute of Physics 1996, used with permission.)

*S. Kalinin, A. Gruverman
(Eds.), Scanning probe
microscopy: electrical and
electromechanical phenomena
at the nanoscale, Springer 2007*



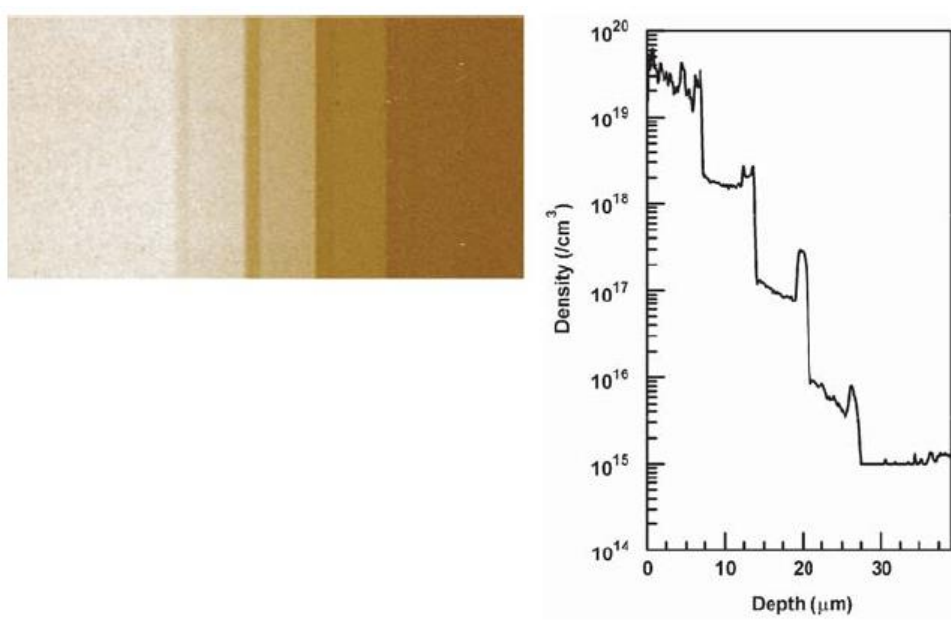


FIGURE 10. (a) SCM image of the IMEC n-step staircase structure. Lowest dopant concentration is on the right side of the image [57]. (b) One-dimensional dopant profile extracted from the center of the SCM image of the staircase structure [57].

S. Kalinin, A. Gruverman (Eds.), Scanning probe microscopy: electrical and electromechanical phenomena at the nanoscale, Springer 2007

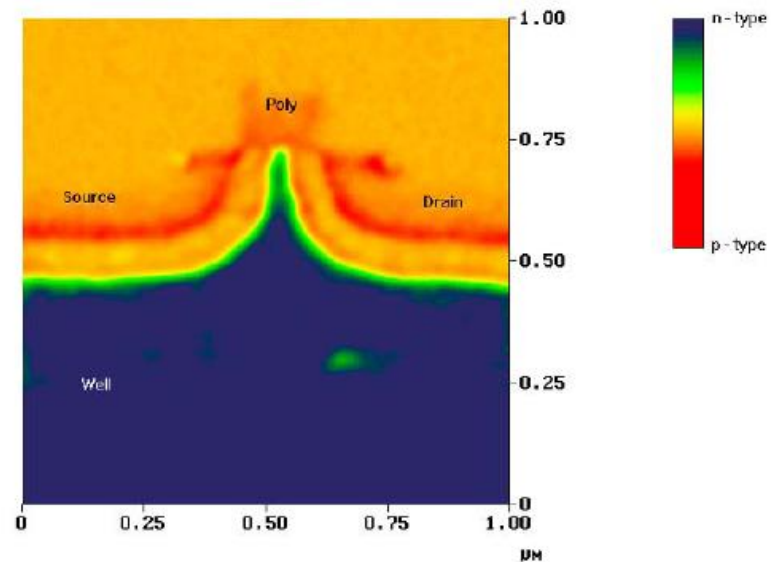
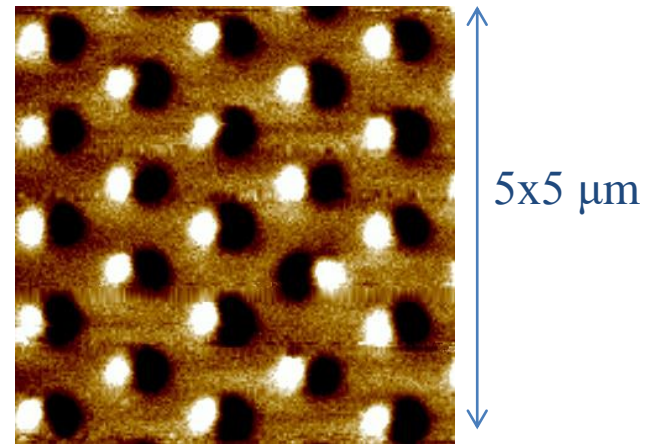
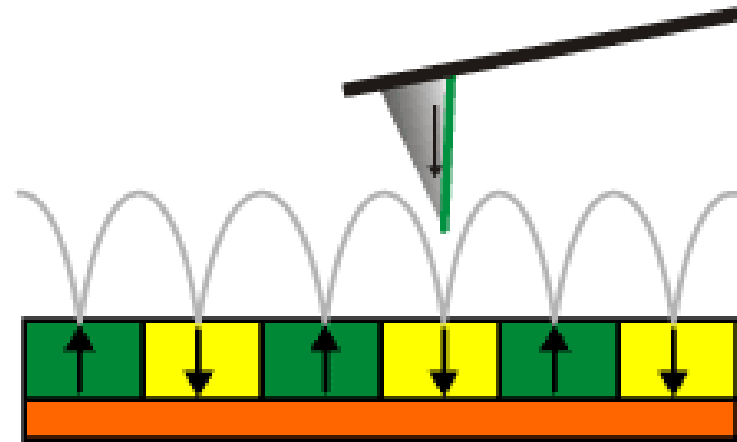
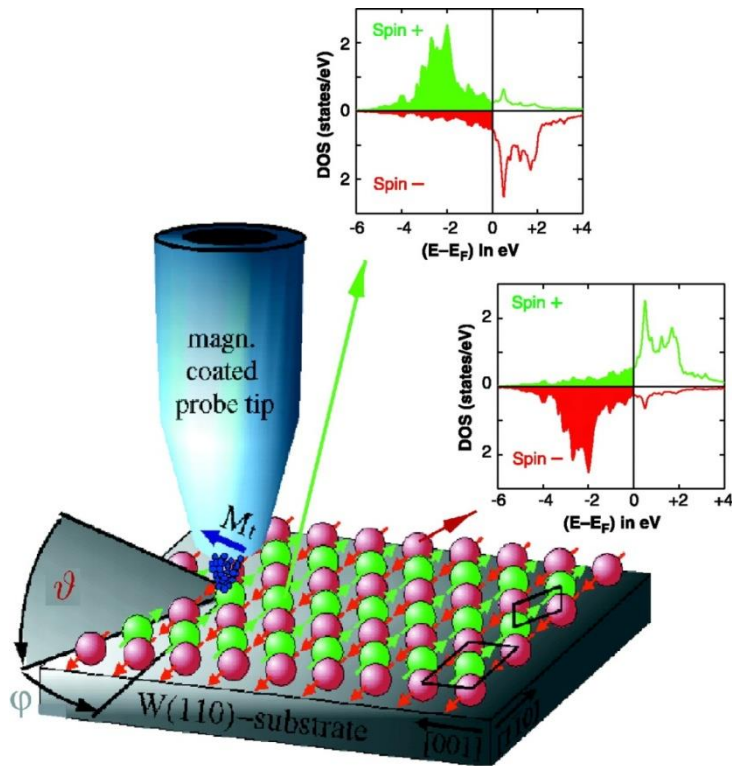


Figure 2. Scanning Capacitance Microscopy of a 0.18 nm FET. Contrast in capacitance is related to local dopant concentration. Source, drain and gate are indicated, along with the channel. This data demonstrates that spatial resolution on the order of tens of nms is necessary to characterize variations in this device. (courtesy of C. C. Williams)

e) Nanoscale probing of magnetic and spin-dependent properties



DC MFM_en_wn.swf

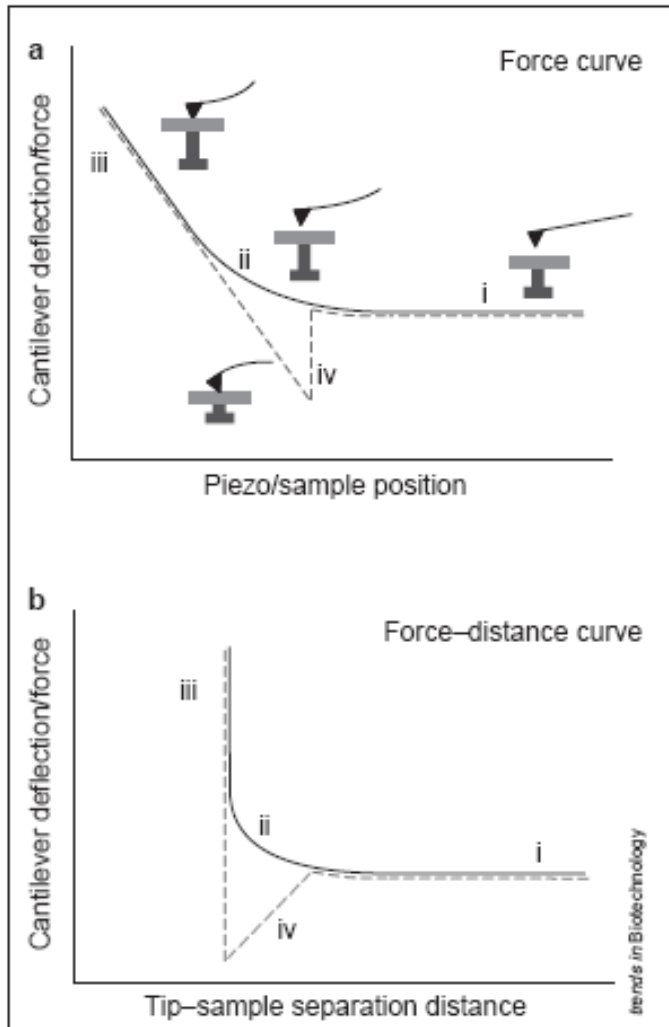
An array of nanomagnets (Co) as seen by a magnetic force microscope. This is a false-color image of the magnetic fields, rather than of the actual dots of magnetic material. White areas indicate magnetic field lines coming up out of the plane of the image, and dark areas indicate field lines going down into the plane. Each magnet appears as a dipole with a pole at each end and field lines curving up and around between the poles. All the dipoles here are aligned in the same direction except one.

f) Nanoscale probing of mechanical properties: force-distance spectroscopy

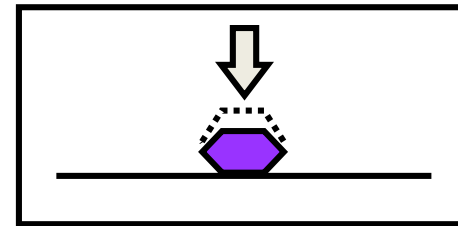
$$F_{ts}(z) = \underbrace{-\frac{A_H R}{6z^2}}_{\text{long-range}} + \underbrace{\frac{12E_0}{r_0} \left(\left(\frac{r_0}{z}\right)^{13} - \left(\frac{r_0}{z}\right)^7 \right)}_{\text{short-range}}$$



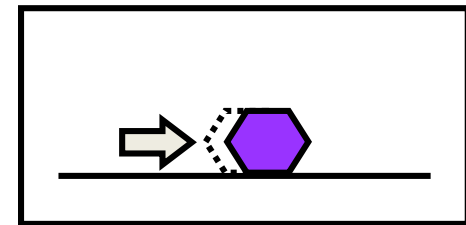
adhesion force imaging_en_n.swf



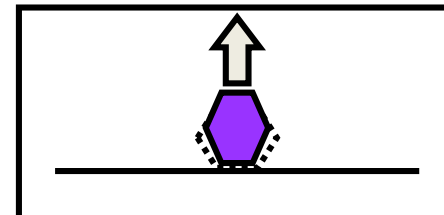
Mechanical Properties



Elasticity



Friction



Binding

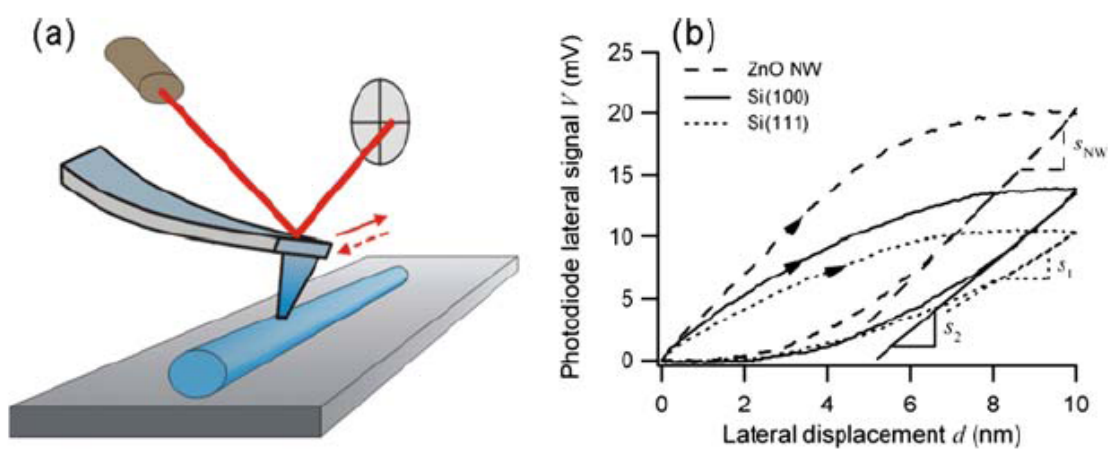
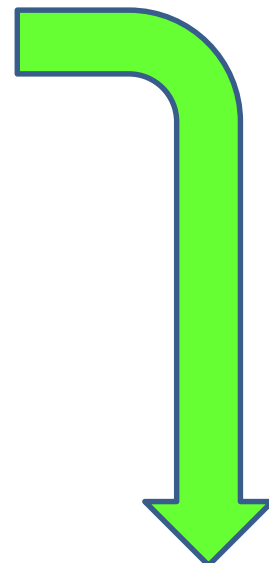


Fig. 16.10. (a) Friction-type measurements on top of a ZnO NW. (b) The initial slope of lateral force-displacement curves is used to calculate the tangential shear modulus. The arrows on the friction loops indicate the scan direction. As illustrated in (a), the lateral force is proportional to the lateral signal from the photodiode (Reprinted with permission from Stan et al. [41]. Copyright 2007 American Chemical Society)



G. Stan et al., Nano Lett. 7, 3691 (2007)

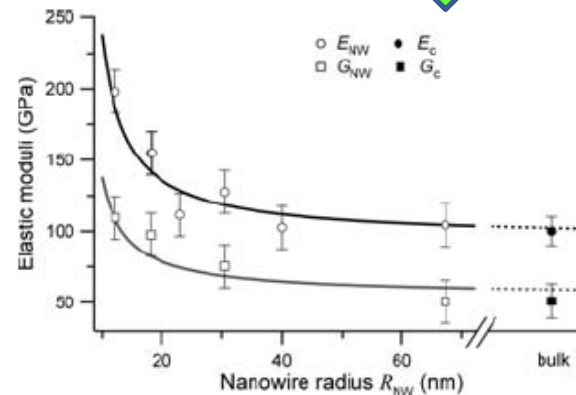


Fig. 16.11. Elastic moduli E_{NW} and G_{NW} as determined from CR-AFM and friction-type measurements on ZnO NWs of various diameters. The fitting curves were obtained by modeling the NW structure as composed of two coaxial cylindrical parts: a core made of bulk material and a shell of stiffer material relative to the bulk (Reprinted with permission from Stan et al. [41]. Copyright 2007 American Chemical Society)

g) Manipulation of atoms and nanostructures

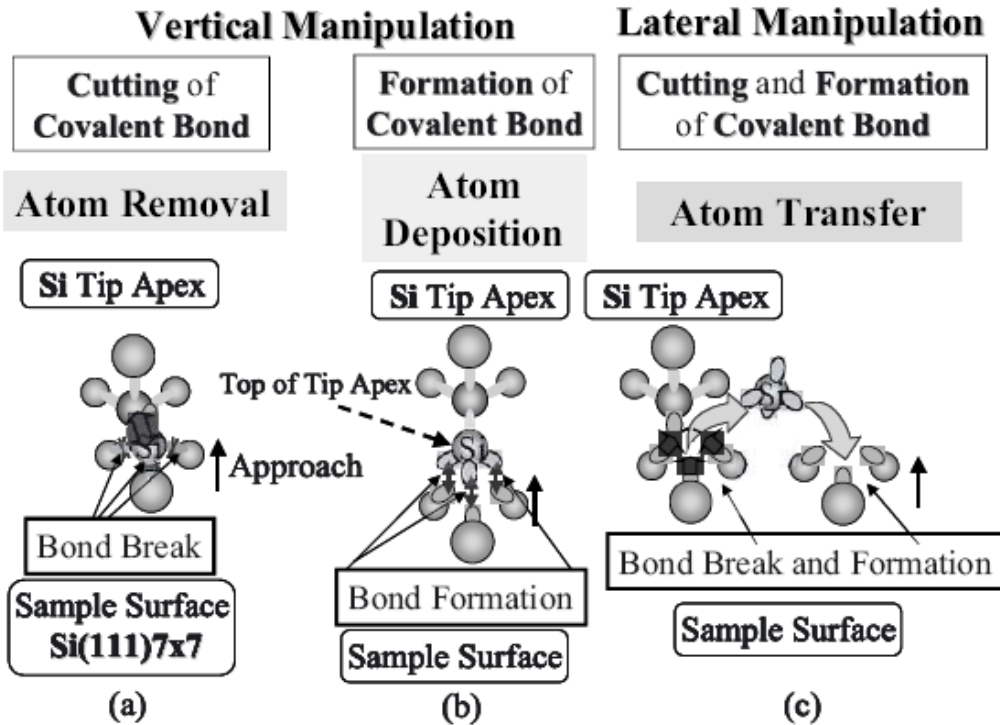


Figure 20. Schematic models of elementary processes of (a) atom extraction, (b) atom deposition, and (c) lateral manipulation of Si adatom on Si(111)7x7 sample by mechanical contact.

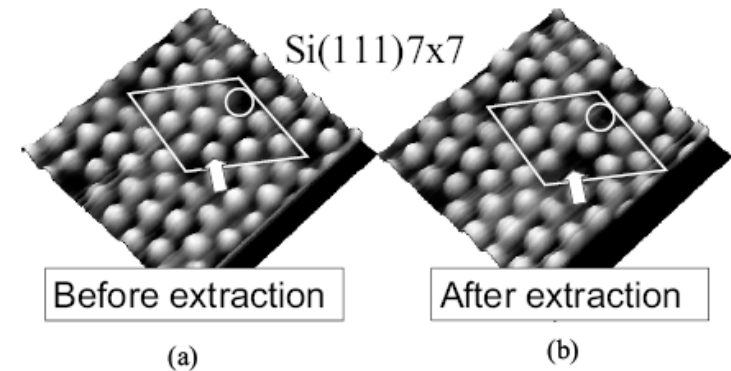


Figure 15. NC-AFM images of Si(111)7x7 at 9.3 K (a) before Si and (b) after Si adatom extraction by mechanical contact.

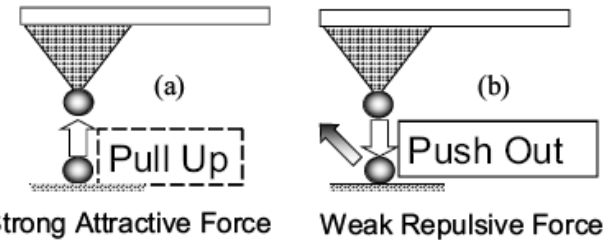


Figure 16. Elementary processes of vertical atom manipulation by mechanical contact. (a) Pull up process under strong attractive force and (b) push out process under weak attractive force.

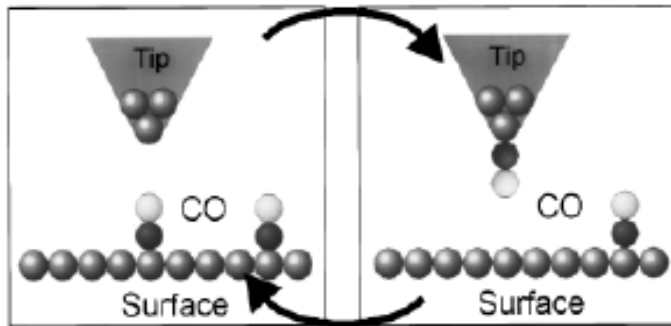
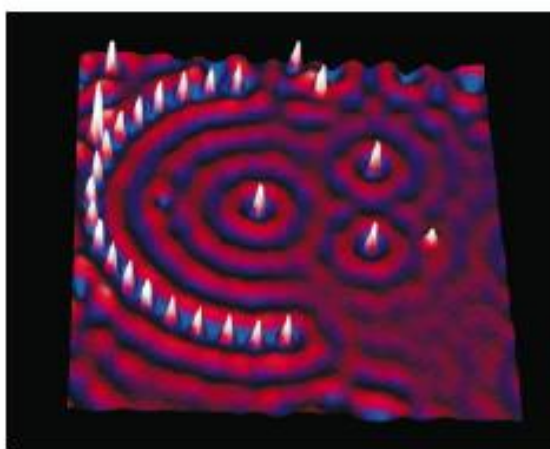
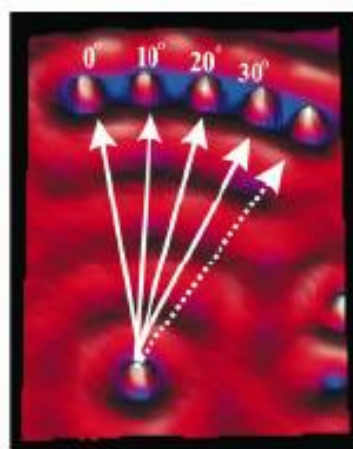


Fig. 2. Sketch of the picking up and putting down procedures of CO molecules on Cu(111). Notice that the CO stands upright on the surface and has to switch its orientation when being transferred to the tip. Reprinted with permission from Ref. 14, © 1997, American Institute of Physics.

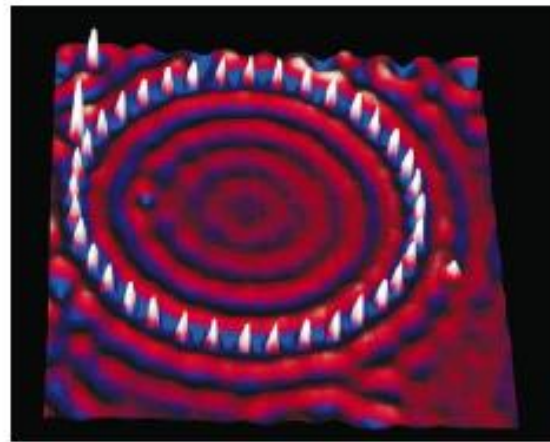
K. S. Birdi, Scanning probe microscopes: application in science and technology, CRC Press 2003



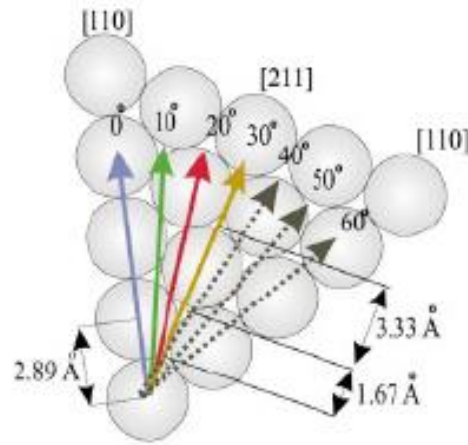
(a)



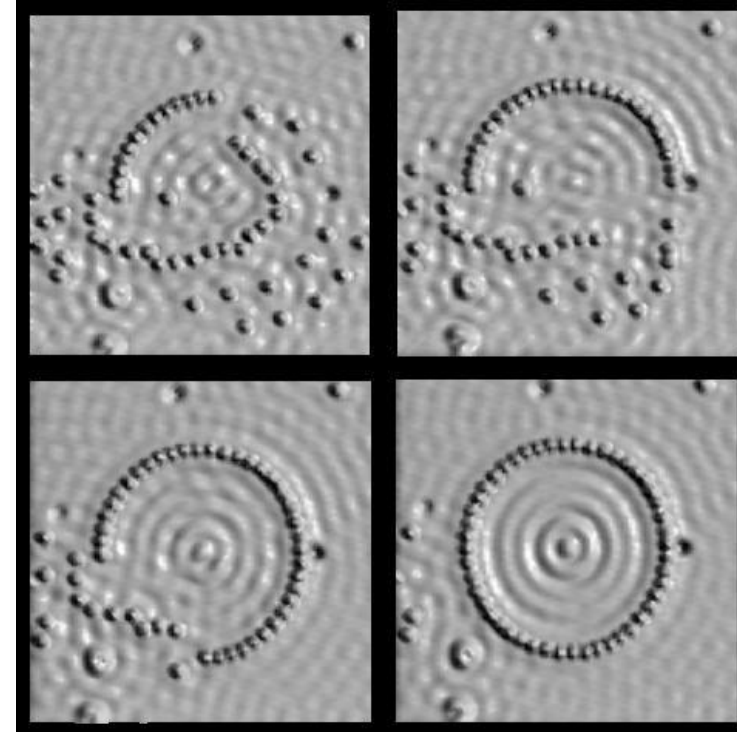
(c)



(b)



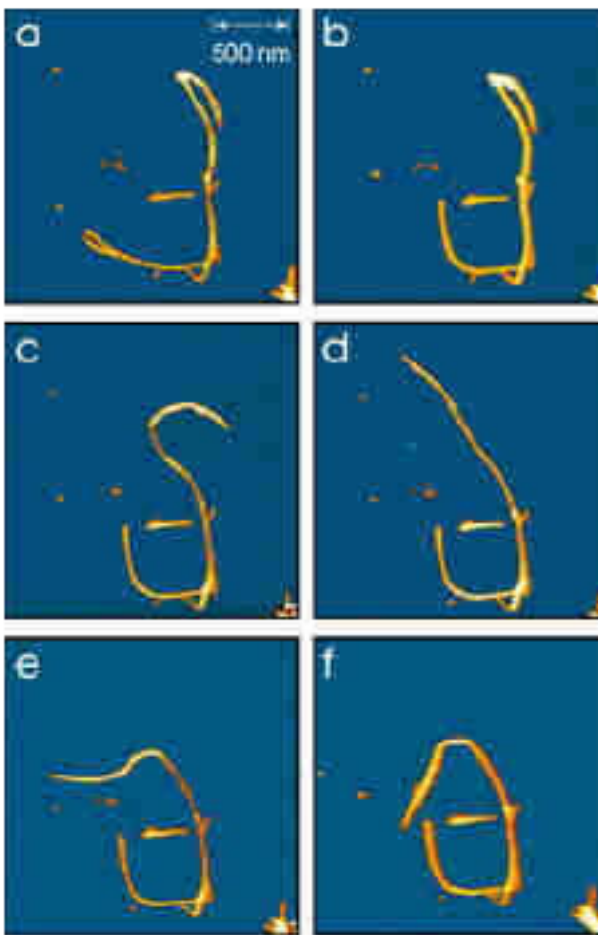
(d)



Xe atoms on Ni

Fig. 1. Quantum corral construction. 3D STM images show (a) during construction and (b) after completion of the corral. 36 Ag atoms (white protrusions) are used (diameter = 31.2 nm). A STM image (c) and a sphere model (d) demonstrate the tip-paths and the surface geometry encountered during manipulations. Reprinted with permission from Ref. 13, © 2003, The American Physical Society.

A. S. Foster, W. A. Hofer, Scanning probe microscopy: atomic scale engineering by j and currents, Springer 2007



A. S. Foster, W. A. Hofer, Scanning probe microscopy: atomic scale engineering by forces and currents, Springer 2007

Left image: Manipulation of a nanotube on a silicon substrate. The AFM tip is used to create the Greek letter "theta" from a 2.5 micron long nanotube.

h) Nanofabrication: Scanning Probe Litography

A. S. Foster, W. A. Hofer, Scanning probe microscopy: atomic scale engineering by forces and currents, Springer 2007

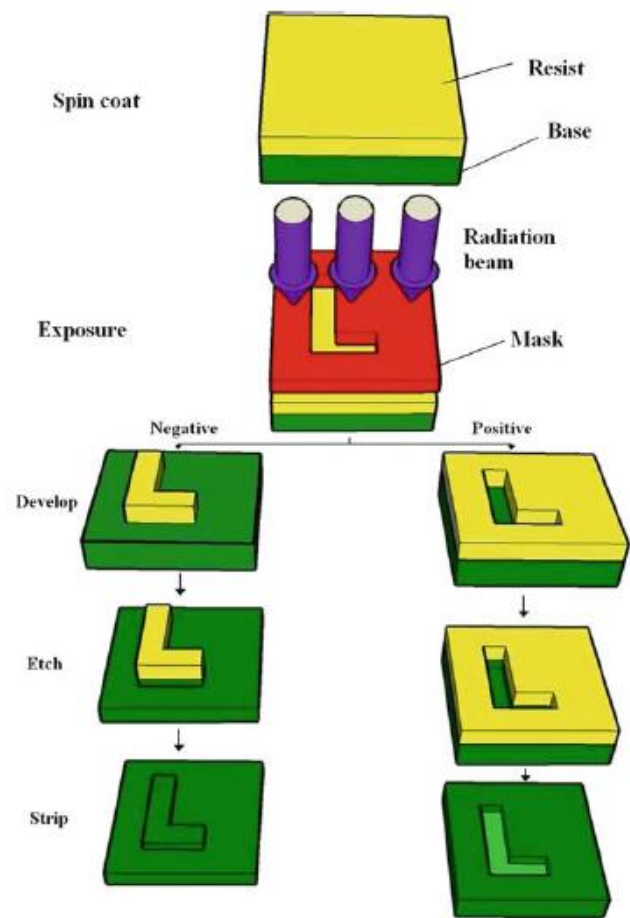


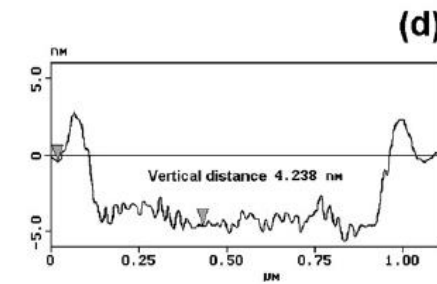
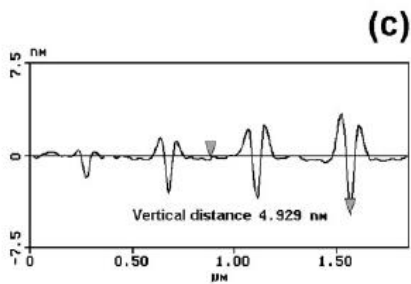
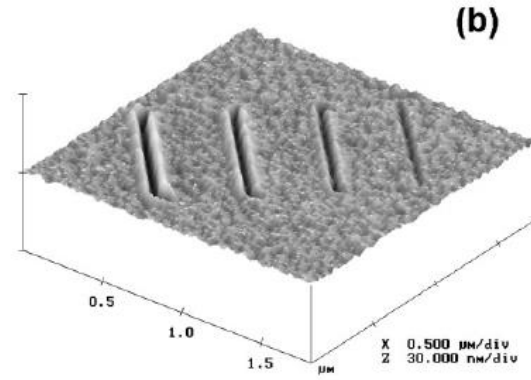
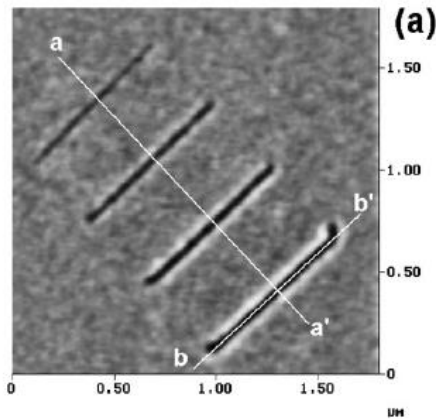
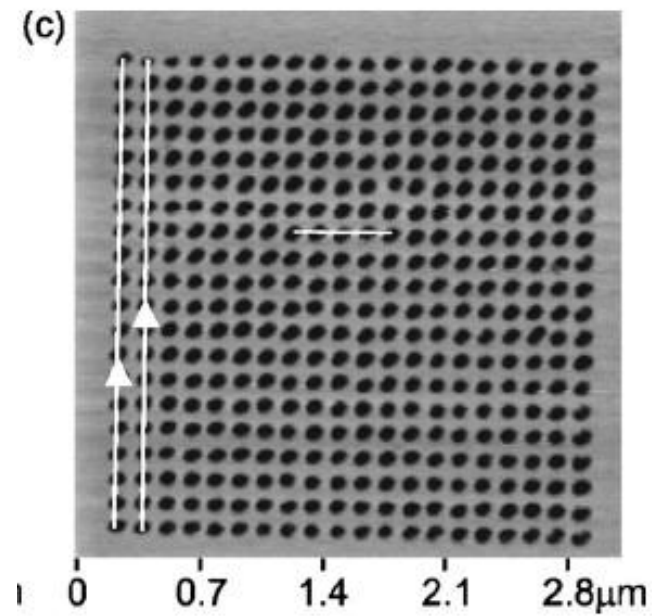
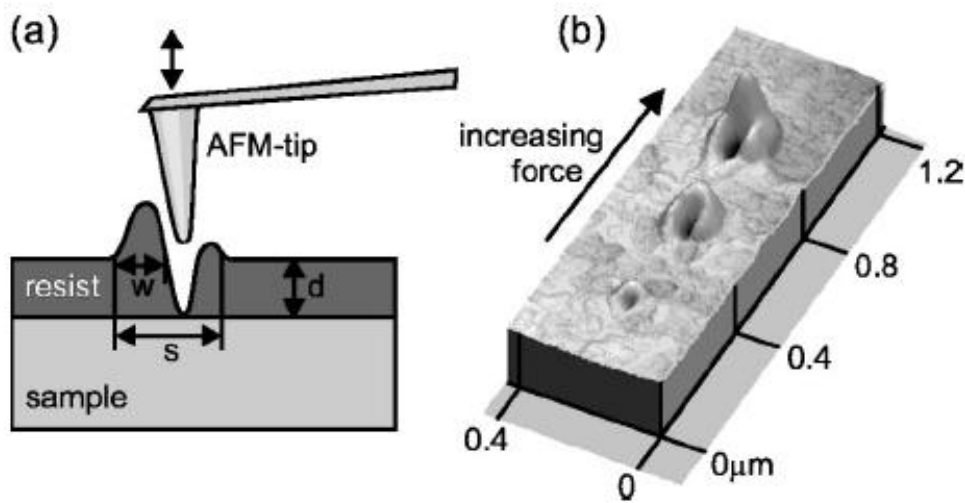
Fig. 21.1. Schematic representation of the lithography process

Table 1. Comparison of SPM nanolithography with other lithographic techniques.

Lithographic techniques	Patterning methods	Operation conditions	Resolution	Advantages	Limitations
SPM	Based on tip-sample interaction	Ambient vacuum or liquid phase	Single atom, A few Å	<ul style="list-style-type: none"> — Easy to operate — Low cost — Applicable to wide range of materials — High sensitivity and site-specific 	<ul style="list-style-type: none"> — Serial patterning — Controllability and accessibility for large scale production
Photolithography	Selectively exposing parts of substrate to light (often Ultraviolet)	Vacuum	Usually sub 100 nm ⁴	<ul style="list-style-type: none"> — Parallel patterning — Good controllability 	<ul style="list-style-type: none"> — High operation cost — Multiple process steps — Poor accessibility
Electron-beam lithography	Interaction between e-beam and substrate	Vacuum	≤ 50 nm ⁵	<ul style="list-style-type: none"> — Well developed for research — Good controllability 	<ul style="list-style-type: none"> — High operation cost — Multiple process steps — Poor accessibility
Focus ion beam (FIB) lithography	Interaction between ion-beam and substrate	Vacuum	~ 50 nm ⁶	<ul style="list-style-type: none"> — High sensitivity — Good controllability — Well developed for research 	<ul style="list-style-type: none"> — High operation cost — Multiple process steps — Poor accessibility
Nanoimprint lithography (NIL)	Mechanical deformation of imprint resist	Vacuum or ambient	~ 100 nm ⁷	<ul style="list-style-type: none"> — Low cost — High throughput — Parallel writing 	<ul style="list-style-type: none"> — Precision issue — Multiple steps for large scale production

Table 5. Applications of AFM nanooxidation on different substrates.^{1,24-33}

Type of substrate	Nanostructures fabricated
Semiconductors	<ul style="list-style-type: none"> — Fabrication of nanometer-scale side-gated silicon field-effect transistors — High speed and large area writing, e.g. fabrication of 0.1 mm metal oxide semiconductor field effect transistors on amorphous silicon (α-Si) films — Fabrication of high quality antidot lattices, e.g. 20 × 20 antidot array with a lattice period of 300 nm — Electrical conduction on hydrogenated diamond
Metals	<ul style="list-style-type: none"> — Fabrication of metal-oxide devices on thin Ti films (~ 7 nm) — Probe-grown nickel oxide as a catalytic template for selective growth of CNTs — Oxidation of molybdenum (Mo) film to form MoO₃ patterns
Molecularly functionalized/passivated surfaces	<ul style="list-style-type: none"> — Oxidation of Si covered by organosilane TMS monolayer. — Poly(benzylether) dendrimers terminated with both benzyl and tert-butylidiphenylsilyl ether groups as resists for AFM oxidation lithography — Oxidation of surfaces passivated by mixed SAM layer comprising 1,12-diaminododecane dihydrochloride (DAD · 2HCl) and <i>n</i>-tridecylaminehydrochloride (TDA · HCl)



*A. Notargai et al.,
Nanotechnology 10, 458
(1999)*

*K. Wiesaur, J. Appl.
Phys. 88, 7289 (200)*



AFM lithography-scratching_en_n.swf



AFM lithography-dynamic_plowing_en_n.swf

Figure 6. AFM topography (a) and three-dimensional view (b) of a series of lines patterned on the aluminium mask with different amount of force applied. The section profile along the *aa'* direction (c) shows the increasing average depth of the grooves. In the section profile along the *bb'* direction (d) a well-defined depth with small roughness is the main feature of AFM lithographed lines.

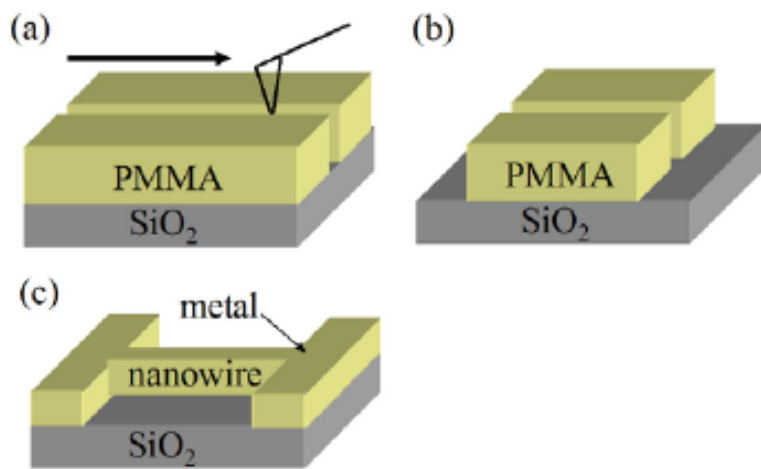


Figure 1. Schematic diagram of the experimental procedure. Note that the contact pads can also be defined first if a specific wire length is not required.

*Y. -J. Chen et al,
Nanotechnology 16, 1112
(2005)*

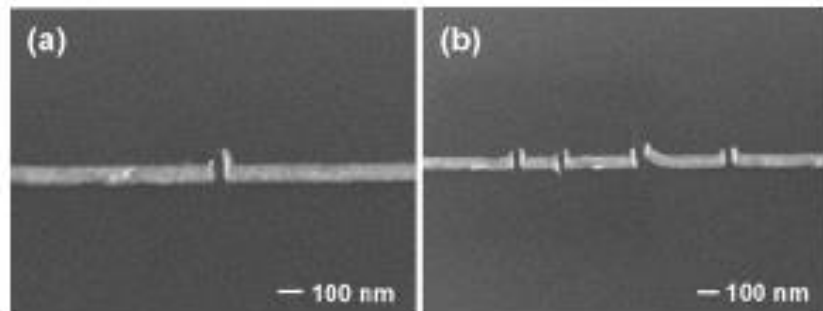


Figure 4. SEM images of (a) a pair of Au nanoelectrodes with a gap of 40 nm made by a cutting on an Au nanowire, and (b) rectangular nanostructures made by repeated cuttings.

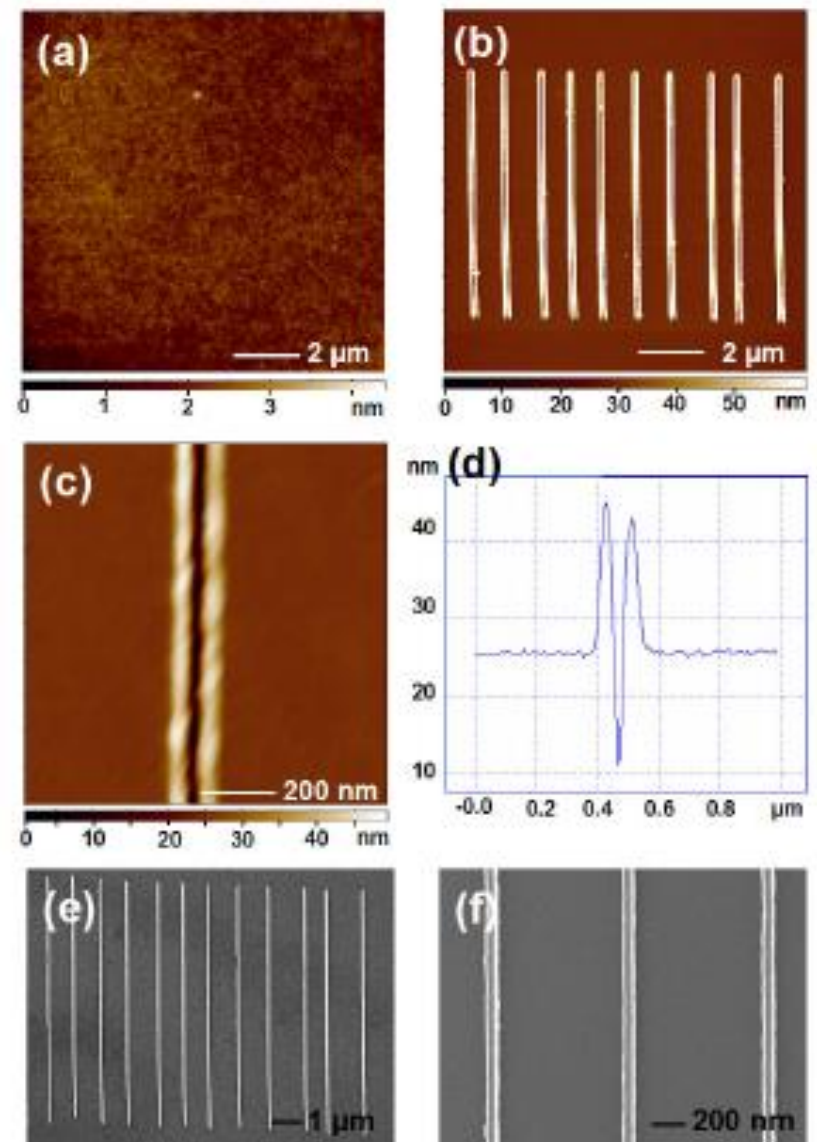


Figure 2. (a) AFM images of the PMMA film, and (b) the result of a nanogroove array after nanoscratching. (c) A zoomed image of a nanogroove, and (d) the corresponding cross-section plot. (e) The SEM image of the Au nanowires fabricated from the pattern, and (f) a zoomed image showing that the width is around 70 nm.



AFM Oxidation Lithography_en_n.swf

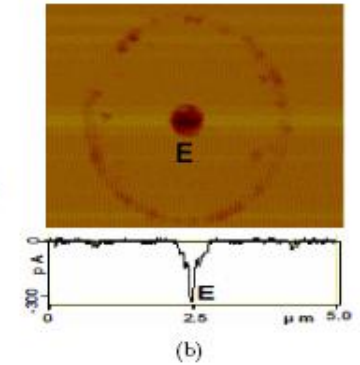
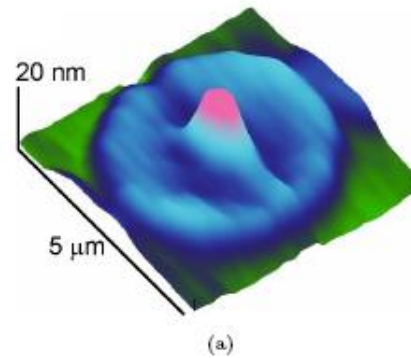
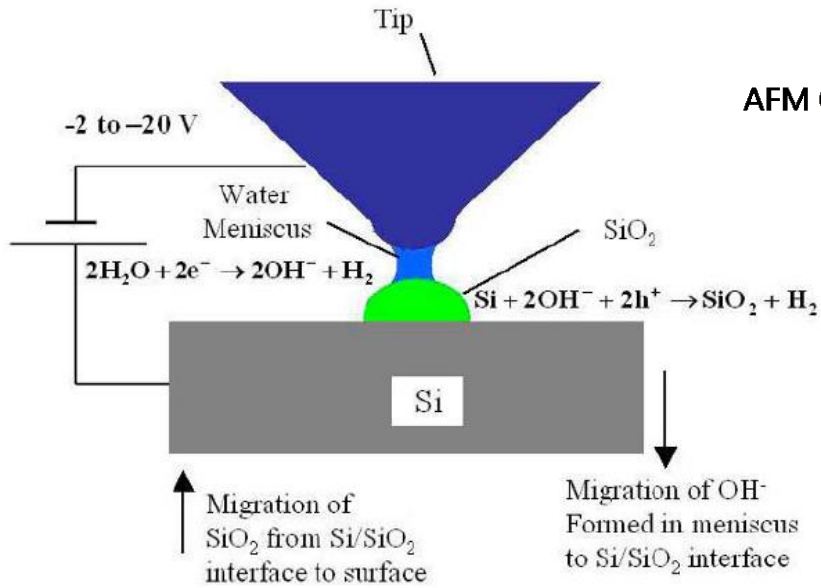
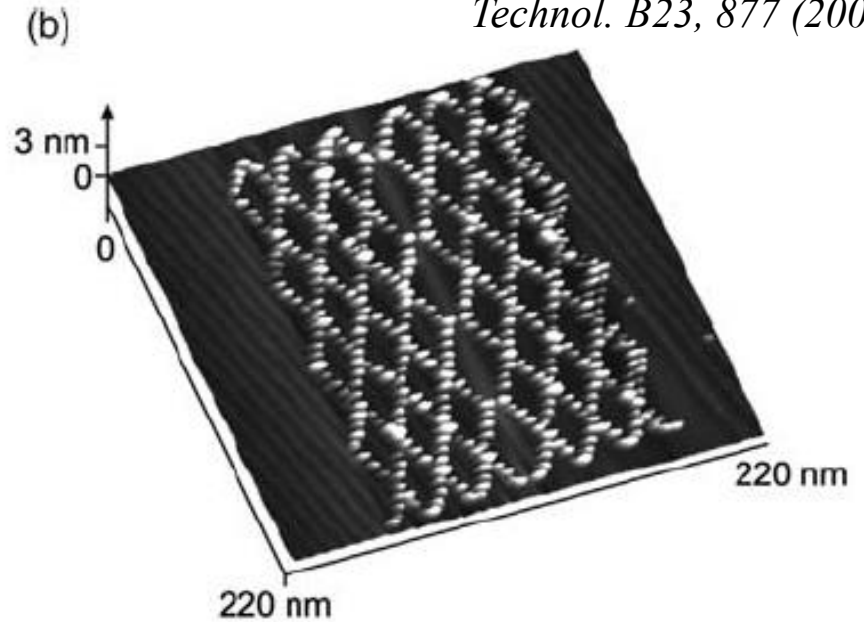
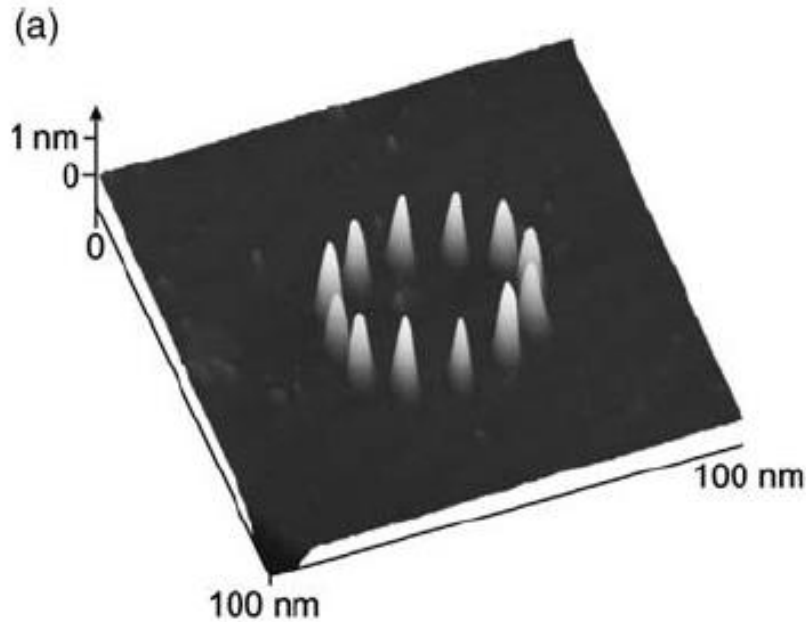


Figure 2. Schematic of SPM-Based oxidation of Si, showing growing SiO₂ dot, and relevant processes.

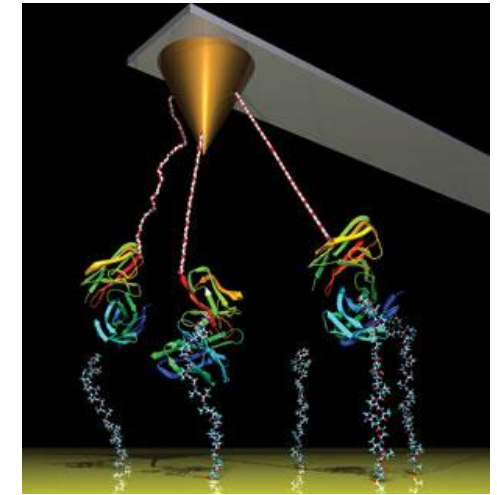
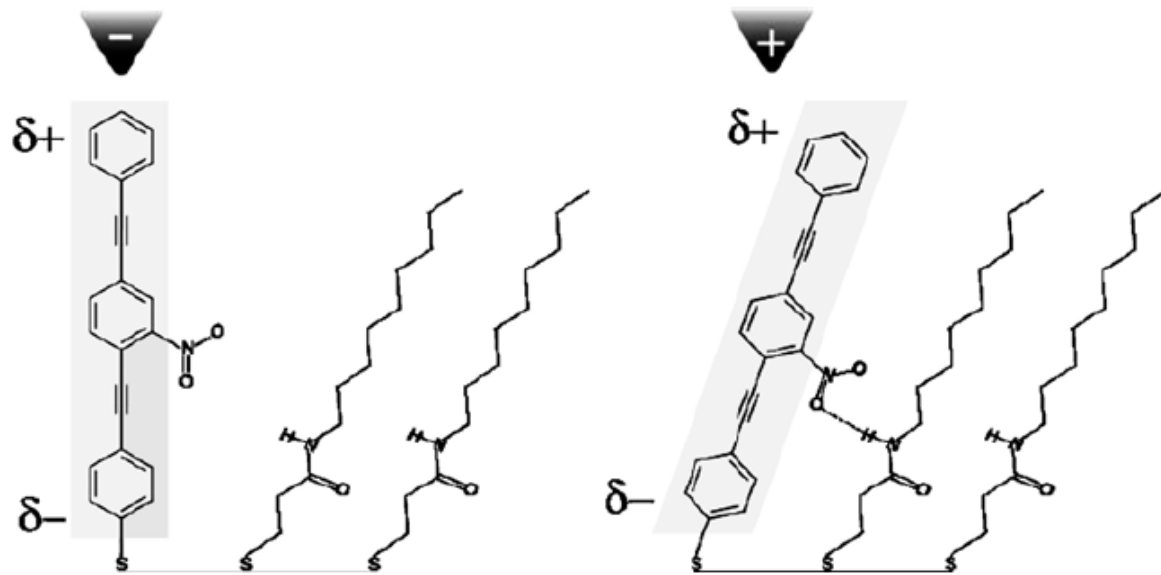
P. Avouris et al, Appl. Phys. Lett. 71, 285 (1997)

A. A. Tseng et al., J. Vac. Sci. Technol. B23, 877 (2005)



2) Chemical Applications

a) Molecules imaging and manipulation



W. Richard Bowen, Nidal Hilal, Atomic Force Microscopy in Process Engineering: An Introduction to AFM for improved processes and products, Elsevier 2009

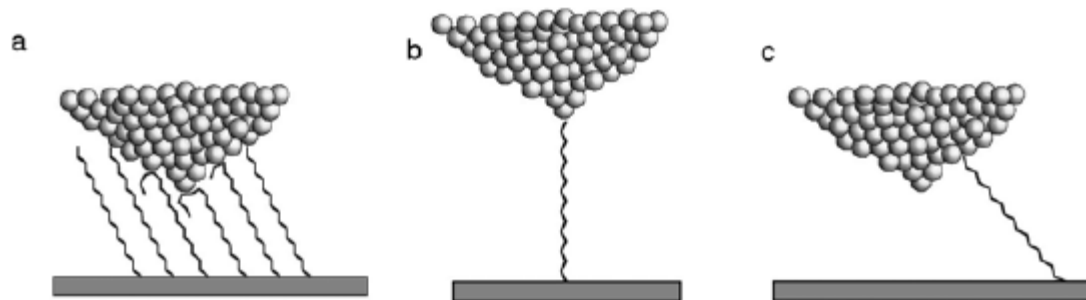
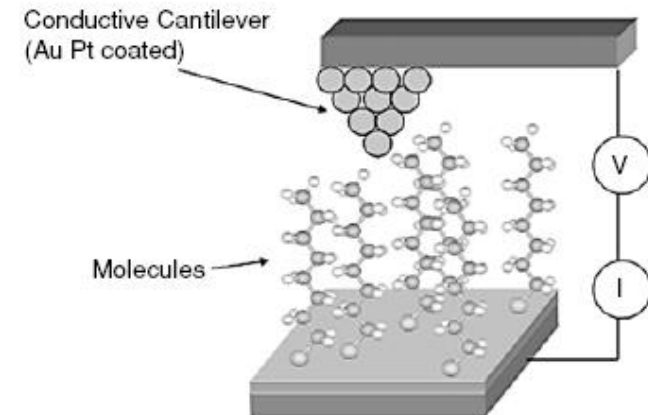


FIGURE 1. Schematic picture of conformation for molecules bridging tip and surface. In (a) it is seen that a variety of molecular conformations should exist in the contact zone under a compressive situation. Comparison of (b) and (c) for stretching or break-junction configurations shows that even a single molecule could have different bond orientation at the surface.



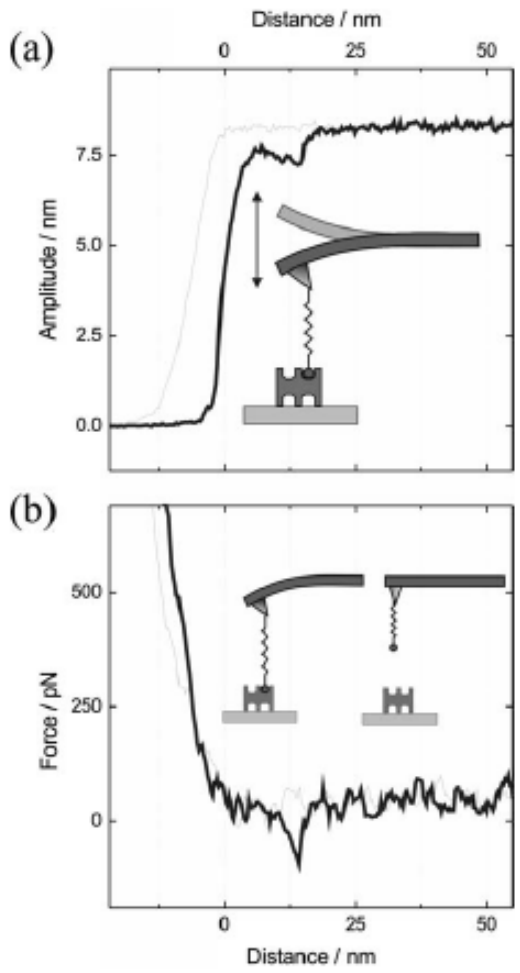


Fig. 10.4. Raw data of an amplitude-distance and a force-distance cycle showing a single avidin-biotin unbinding event. (a) In the amplitude-distance cycle, a single unbinding event is shown at 14 nm, resulting in an amplitude reduction of 1 nm at 8 nm free amplitude. (b) The simultaneously acquired force-distance cycle exhibits the same unbinding event with an unbinding force of 80 pN. Figure taken from [58]

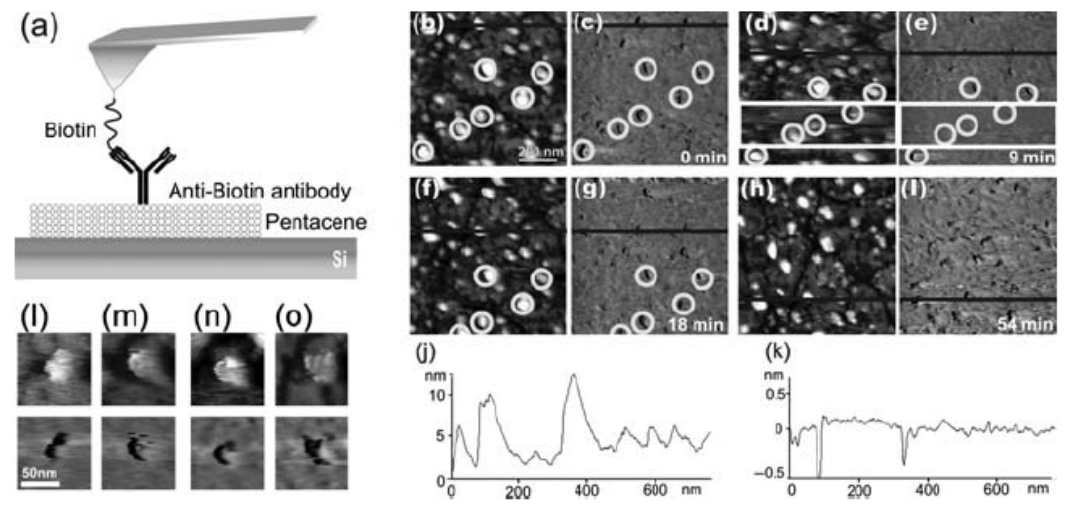
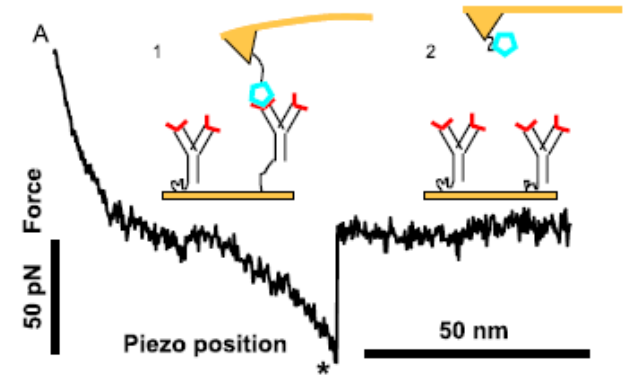


Fig. 10.11. (a) Scheme of the simultaneous topography and recognition AFM imaging of anti-biotin antibodies adsorbed on pentacene islands. Time Series of topography (b), (d), (f), (h) and recognition image (c), (e), (g), (i) of anti-biotin antibodies adsorbed on pentacene-islands obtained using a biotin-functionalized tip. (Gray scale range: topography images: 0 to 13 nm; recognition images: -0.5 to 0.7 nm). (j) and (k), show the cross section indicated by the lines in (b) and (c). (l)–(o) Topography (*top*) and recognition images (*bottom*) of anti-biotin antibodies adsorbed on pentacene islands. Different shapes of recognition spots were observed that can be attributed to different orientations of the Fab fragments of the adsorbed antibodies. (Gray scale range: topography images: 0 to 13 nm; recognition images -0.5 to 0.7 nm). Figures taken from [91]



b) Polymeric surfaces

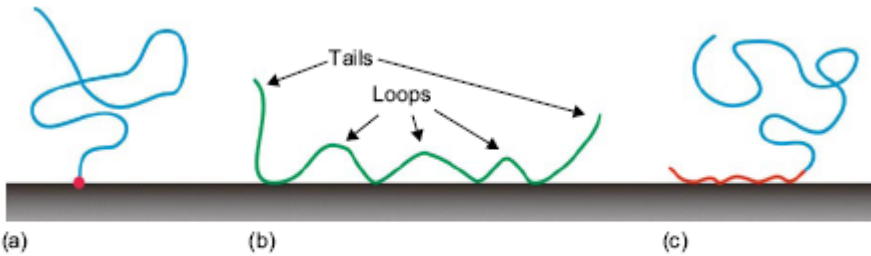


FIGURE 8.1 (a) A polymer chain chemically attached by one of its ends to a solid surface 'swollen' in a good solvent. (b) A polymer chain physisorbed on a solid surface by non-specific (physical) interactions along its backbone (four contact points), forming three loops and two tails. (c) Diblock copolymer in a solvent attached on a solid surface by adsorption of one of its two blocks.

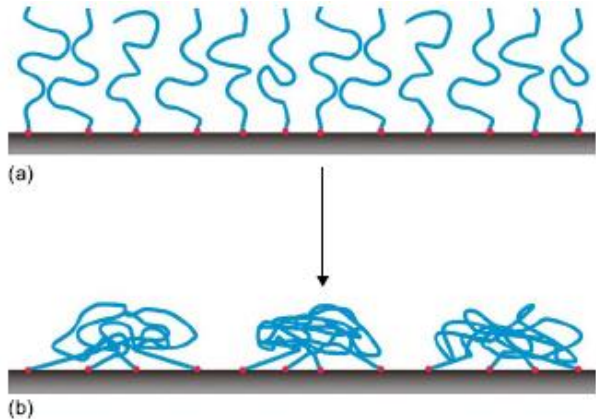
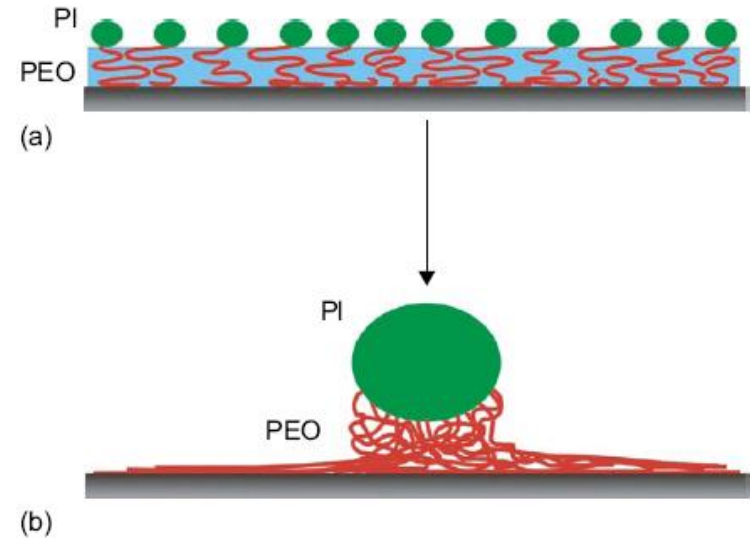


FIGURE 8.3 Schematic drawing of a polymer brush in (a) good solvent conditions and (b) poor solvent conditions. Upon the change of the solvent conditions, the polymer chains could self-organise in nanoscale aggregates of small groups of polymer chains instead of collapsing individually.



W. Richard Bowen, Nidal Hilal, Atomic Force Microscopy in Process Engineering: An Introduction to AFM for improved processes and products, Elsevier 2009

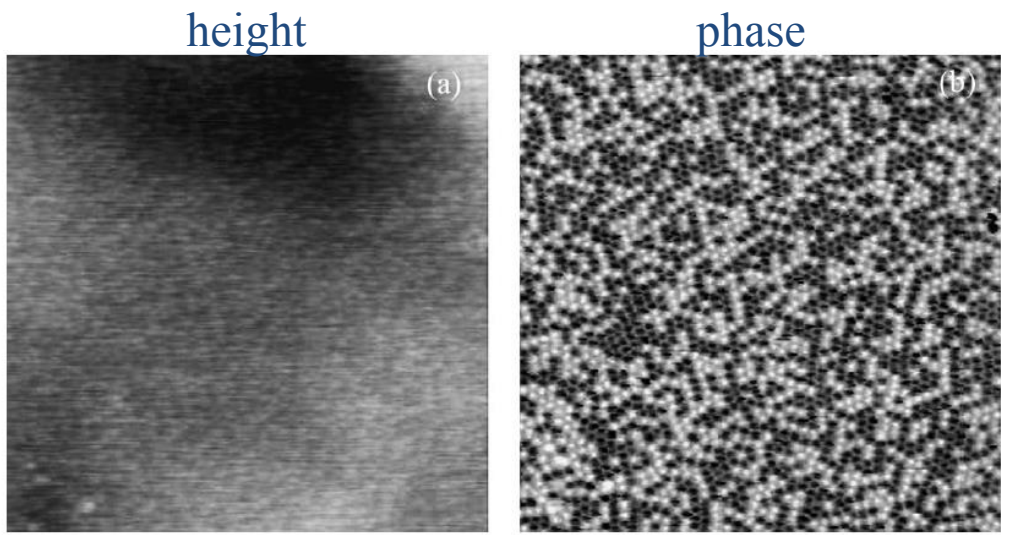


Fig. 19. AM-AFM images of a block copolymer mesophase. (a) Topography and (b) phase image. The phase image allows to resolve the individual spheres (12 nm in diameter). It also allows to distinguish between the crystalline (light) and molten (dark) PEO micelles. Image size 1 mm × 1 mm. The maximum height variation in (a) is 10 nm. By courtesy of Dr. G. Reiter.



Lateral_Force_mode_en_n.swf

c) Imaging in liquids (for several biological samples. Living organisms,....)

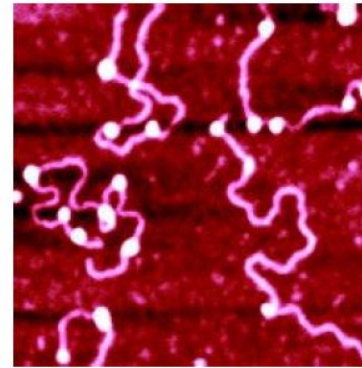
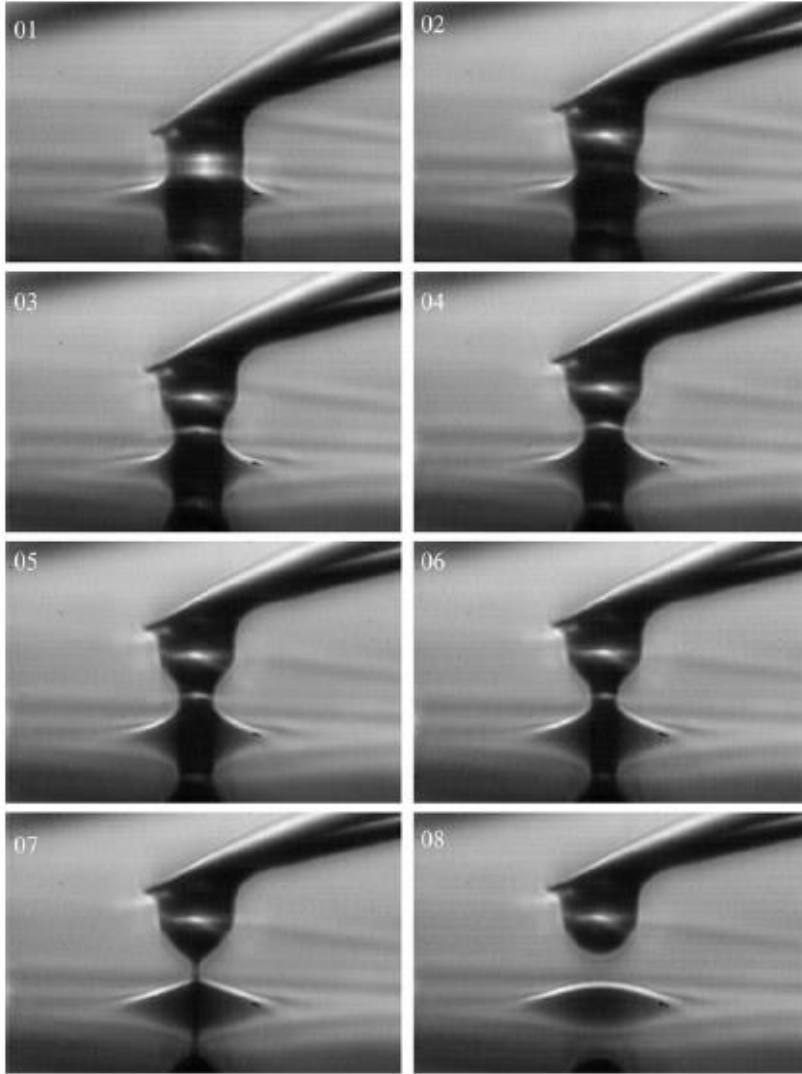
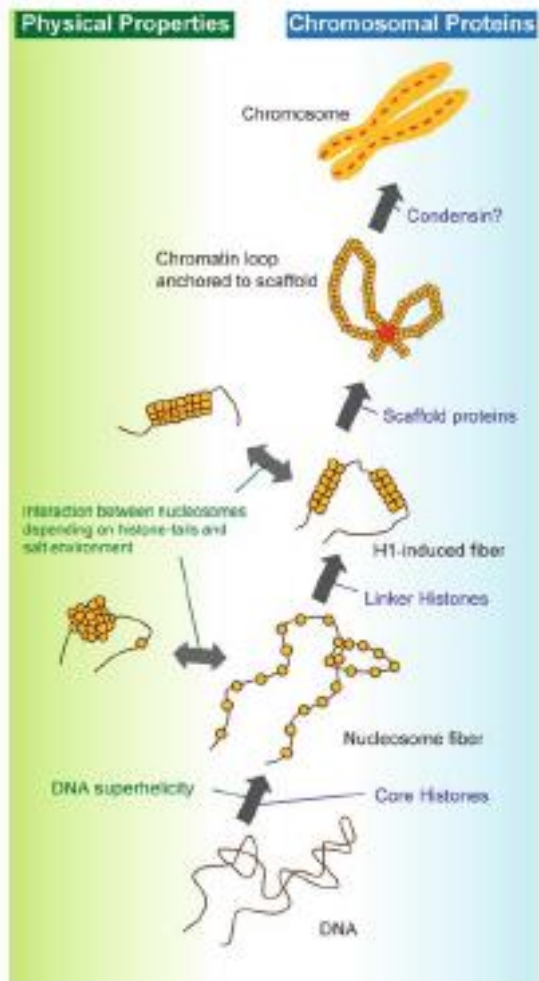


Figure 8. Tapping Mode image of biological sample, in this case nucleosomal DNA.

W. Richard Bowen, Nidal Hilal, Atomic Force Microscopy in Process Engineering: An Introduction to AFM for improved processes and products, Elsevier 2009

3) “Biological and Medical Applications”

a) SPM of biomolecules and DNA on surfaces and at interfaces



W. Richard Bowen, Nidal Hilal, Atomic Force Microscopy in Process Engineering: An Introduction to AFM for improved processes and products, Elsevier 2009

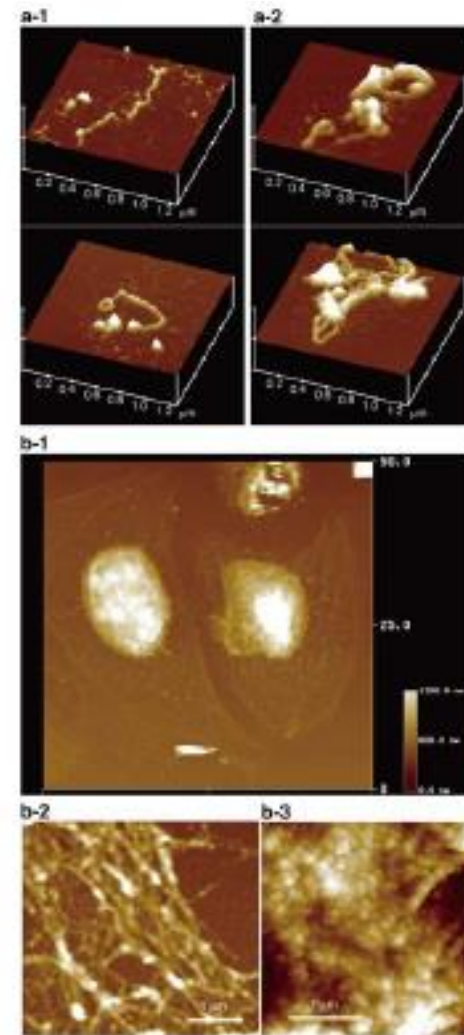
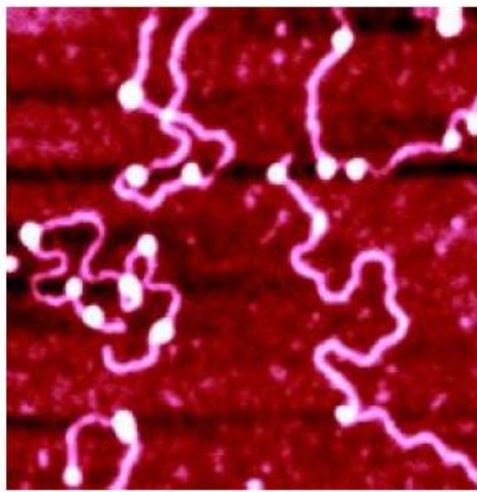


Fig. 20.6. AFM images of higher-order structures of chromatin and cytoskeleton. (a-1) Chromatin fibers were reconstituted from 186-kb plasmid DNA, core histones, and linker histone H1, and their structures were observed by AFM in air. H1-induced 30-nm fibers were detected. (a-2) Addition of topoisomerase II to the reconstituted 30-nm fibers induced loop structures. (b-1) AFM image of HeLa cells depleted of plasma membrane and cytoplasm. HeLa cells on a coverslip were sequentially treated with buffer A containing 0.5% Triton X-100, buffer B containing 250 mM $(\text{NH}_4)_2\text{SO}_4$, and 10U/ml DNaseI (b-1). Cytoskeletal fibers (b-2) and chromatin fibers (b-3) were clearly observed in enlarged images. The interphase chromatin is composed of granular fibers with a width of 78.1 ± 8.1 nm

Fig. 20.7. Schematic presentation of the hierarchical architecture of eukaryotic chromatin/chromosomes. Physical properties of DNA, chromosomal proteins, and local salt concentrations are critical for the formation of higher-order structures. First, DNA interacts with core histones, forming a beads-on-a-string structure, in which negative supercoiling of DNA promotes formation of nucleosomes. Second, linker histone H1 converts the beads-on-a-string into a 20–30-nm fiber. Salt concentrations affect the interaction between nucleosomes. By increasing the concentration of NaCl from 50 to 100 mM, well-separated beads-on-a-string convert to aggregates, and H1-induced fibers thicken from 20 to 30 nm in diameter. As shown in Fig. 20.6a, topoisomerase II, a component of the nuclear scaffold, makes loop structures in H1-induced fibers. Finally, mitotic chromosomes are formed with help from condensin complexes and other cellular components



W. Richard Bowen, Nidal Hilal, Atomic Force Microscopy in Process Engineering: An Introduction to AFM for improved processes and products, Elsevier 2009

Figure 8. Tapping Mode image of biological sample, in this case nucleosomal DNA.

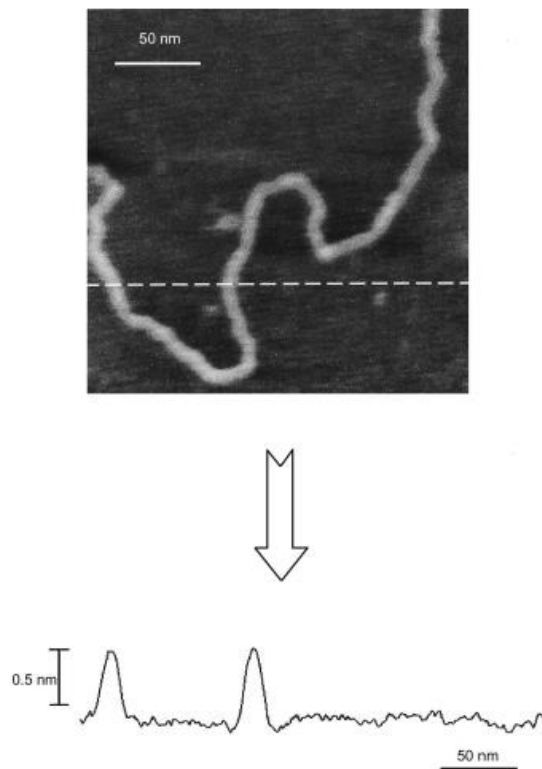


Fig. 15. (a) (top) AM-AFM image of a DNA fragment deposited on mica. (b) (bottom) Cross-section along the dashed line shown in (a).

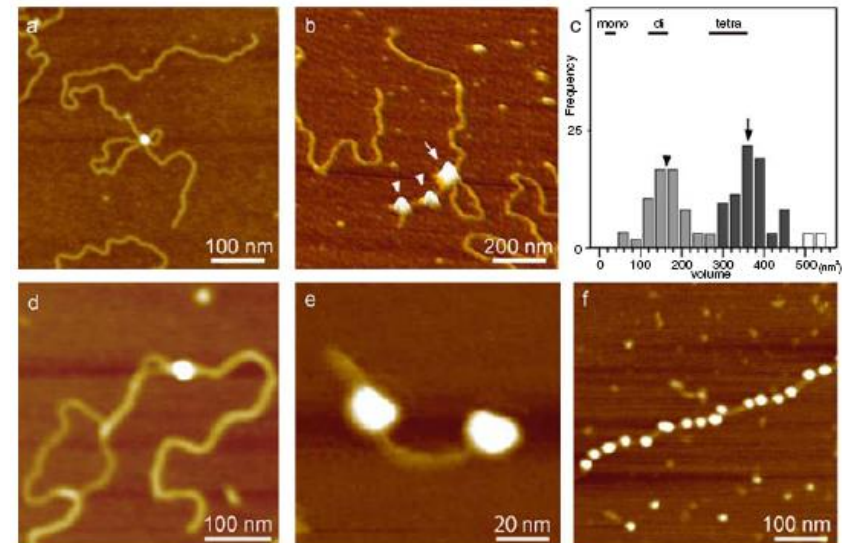


Fig. 20.5. AFM images of DNA-protein complexes. (a) DNA loop in the promoter region of the β -globin gene mediated by transcription factors. (b) DNA-loop mediated by telomere protein, TRF2. The proteins involved in the loop formation (*arrow*) and those not involved in (*arrowhead*) have different sizes. (c) The statistical analysis of the size of the protein in (b) indicates that proteins involved in the loop formation are TRF2 tetramer and those not involved in are dimer. (d) DNA-bound topoisomerase II α . (e) dinucleosome reconstituted from purified core histone and tandem repeat of positioning signals (from the 5S rRNA gene). (f) Polynucleosome reconstituted by an extract from fly embryo

b) Real-time evolution of in-vitro cells, virus, proteins

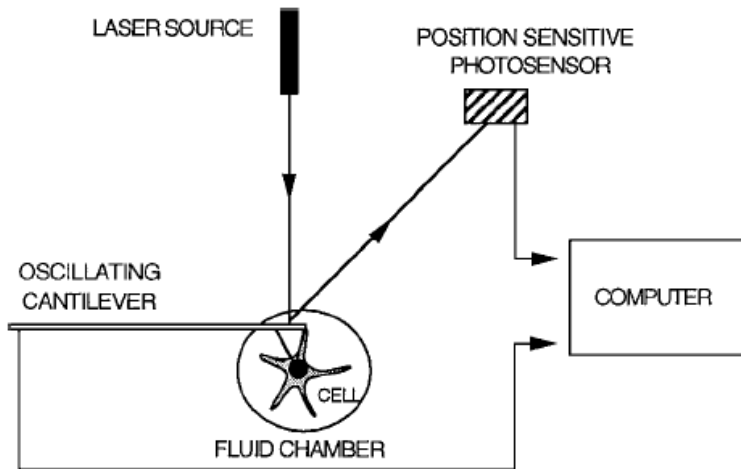


Fig. 1 Schematic diagram depicting key components of an AFM.

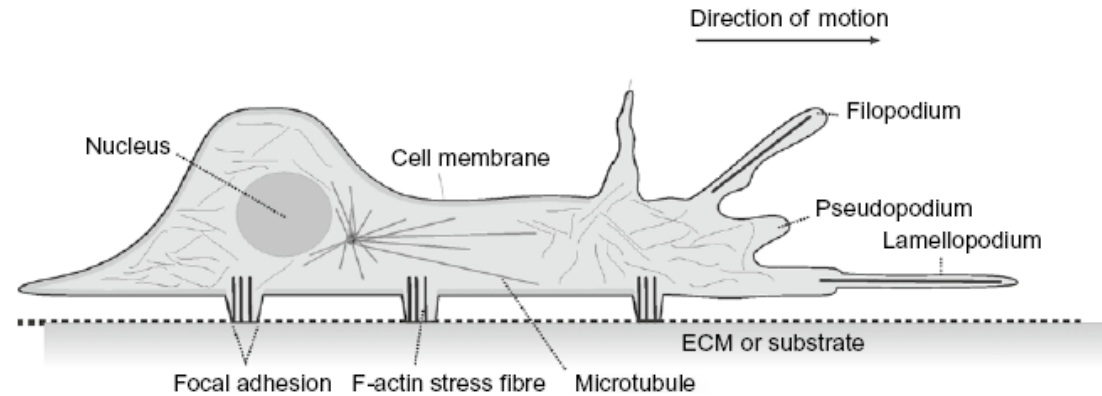


FIGURE 7.1 Schematic drawing of cell adhesion to an ECM or substrate. The cell adheres firmly to the ECM through focal adhesions (a multiprotein complex). The focal adhesions are the sites for the attachment of F-actin stress fibres – one type of cytoskeleton protein. Filopodium and lamellopodium are located at the leading edge for cell to migrate.

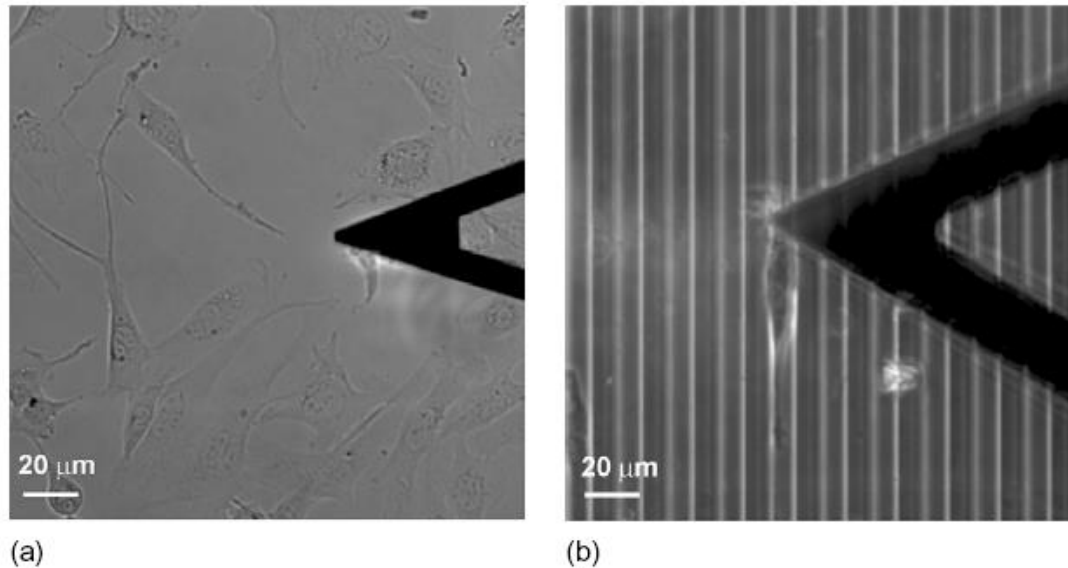
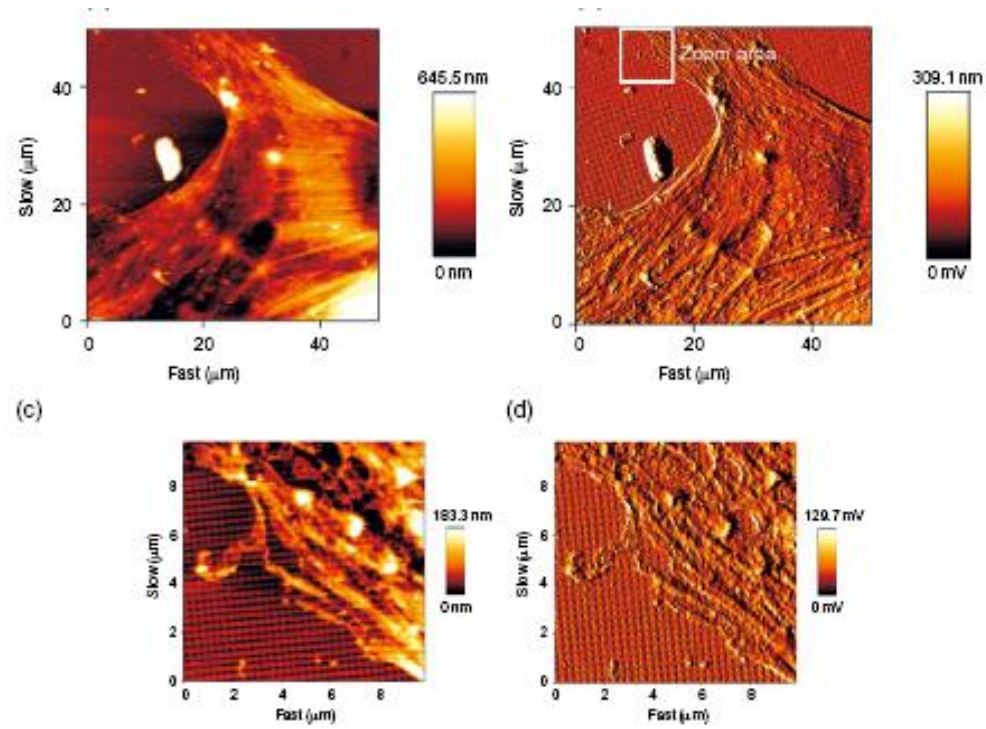
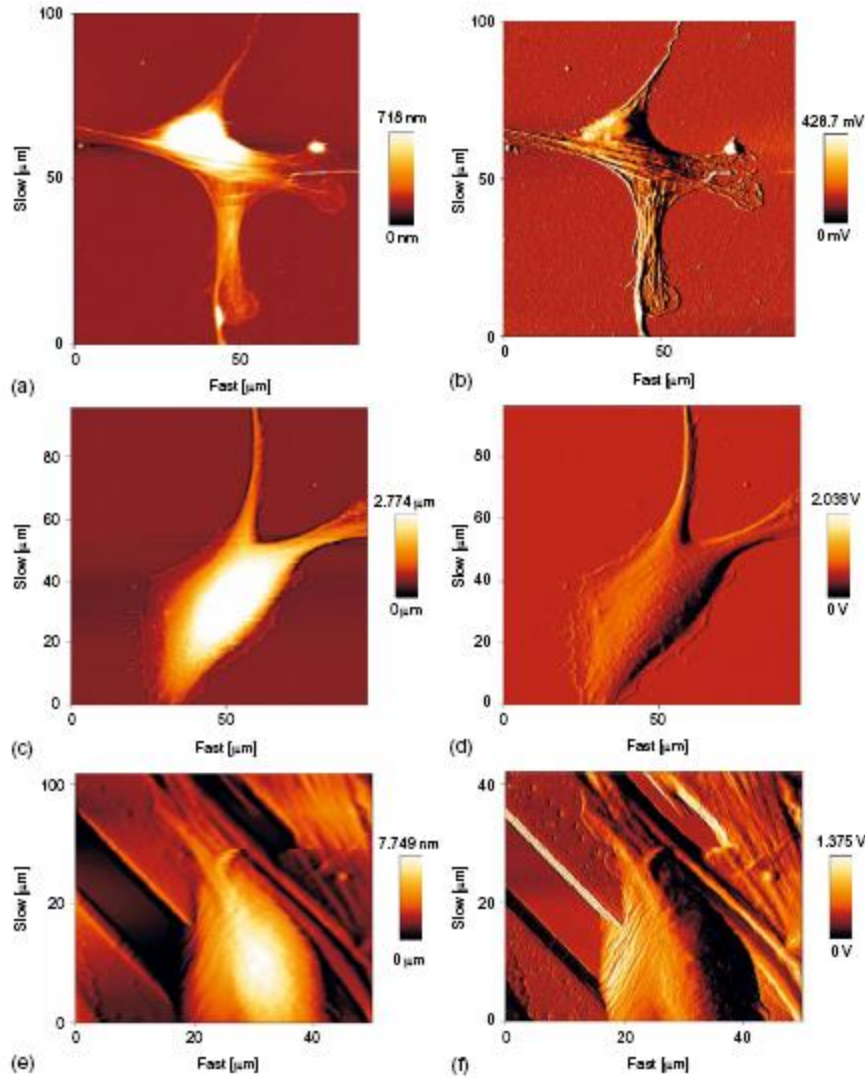


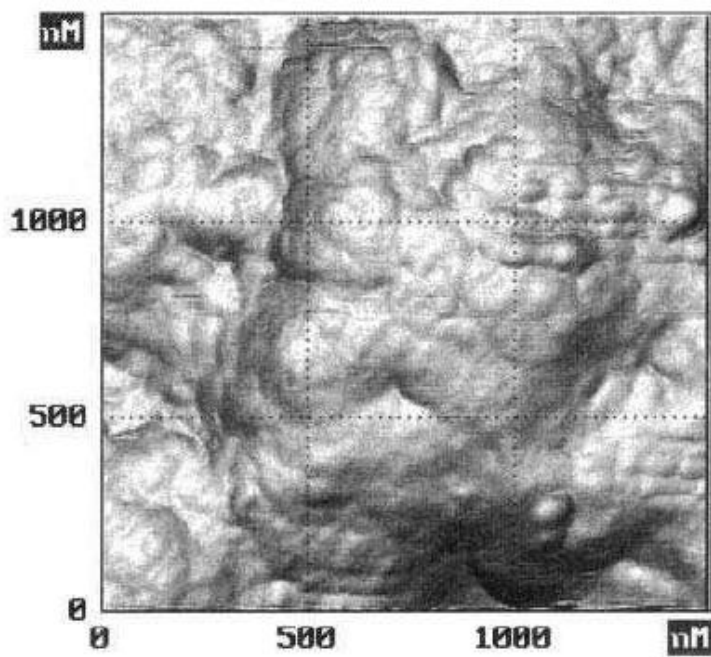
FIGURE 7.7 Optical images of an AFM cantilever positioned over a cell on (a) a planar substrate and (b) a structured substrate.

*W. Richard Bowen,
Nidal Hilal, Atomic
Force Microscopy
in Process
Engineering: An
Introduction to
AFM for improved
processes and
products, Elsevier
2009*

Cell (fibroblast) structure on nanostructured substrate

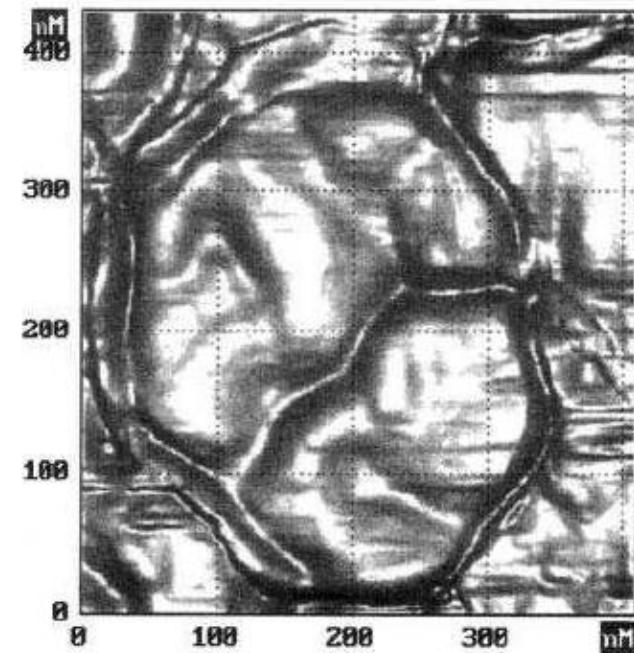
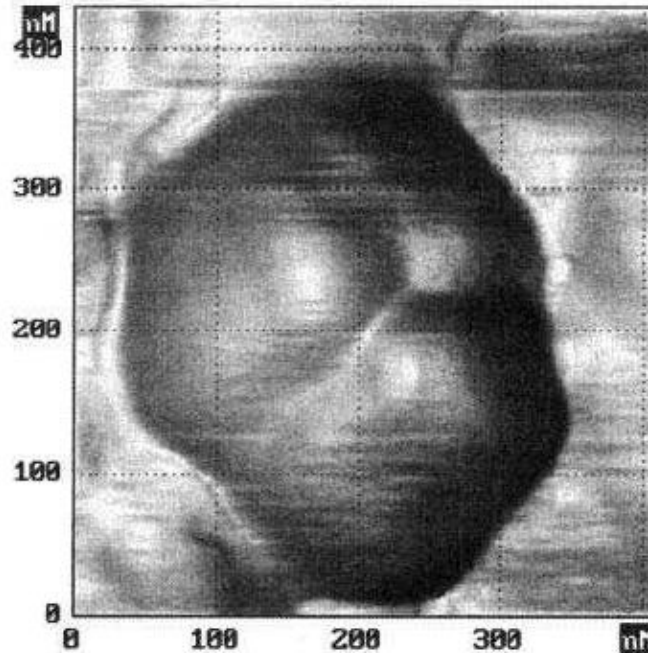
W. Richard Bowen, Nidal Hilal, Atomic Force Microscopy in Process Engineering: An Introduction to AFM for improved processes and products, Elsevier 2009





Healthy Lymphocyte
membrane

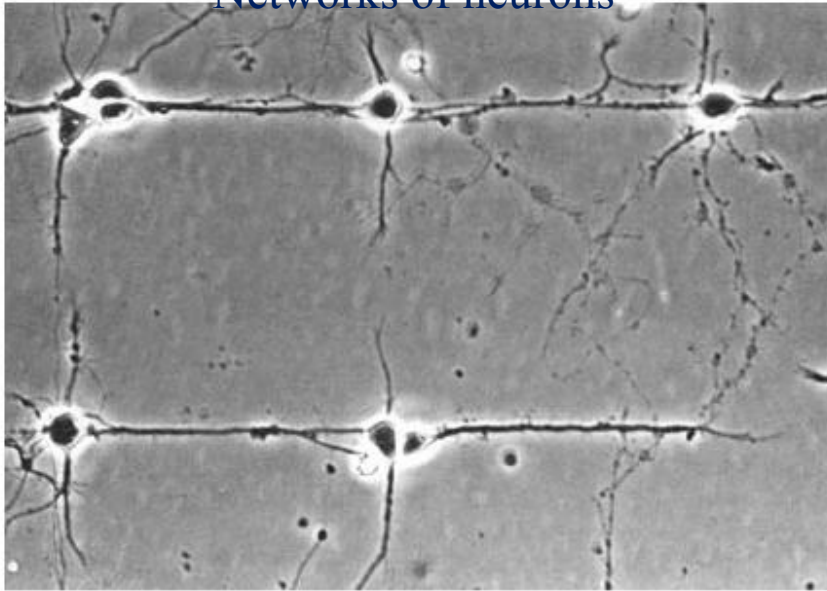
*W. Richard Bowen, Nidal Hilal, Atomic Force
Microscopy in Process Engineering: An
Introduction to AFM for improved processes
and products, Elsevier 2009*



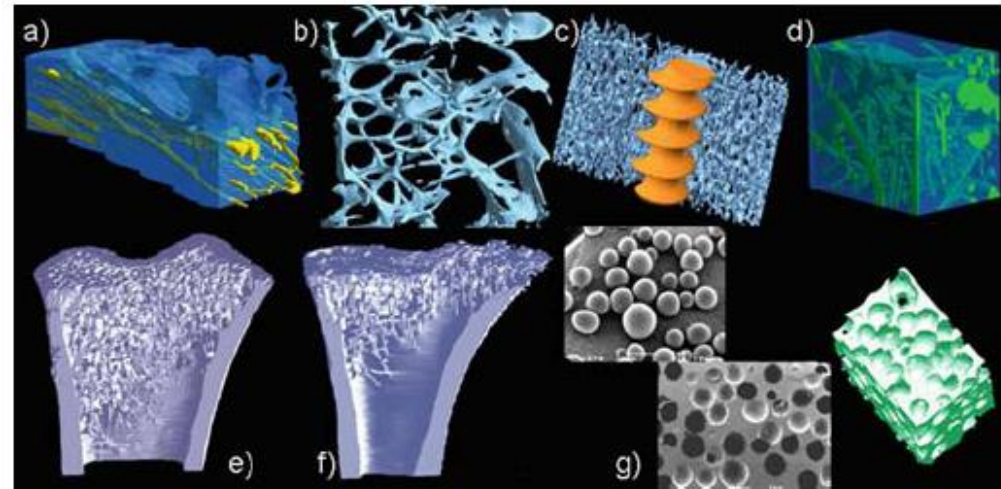
Cancer infected Lymphocyte membrane

c) Electromechanical behaviour in biological systems at the nanoscale

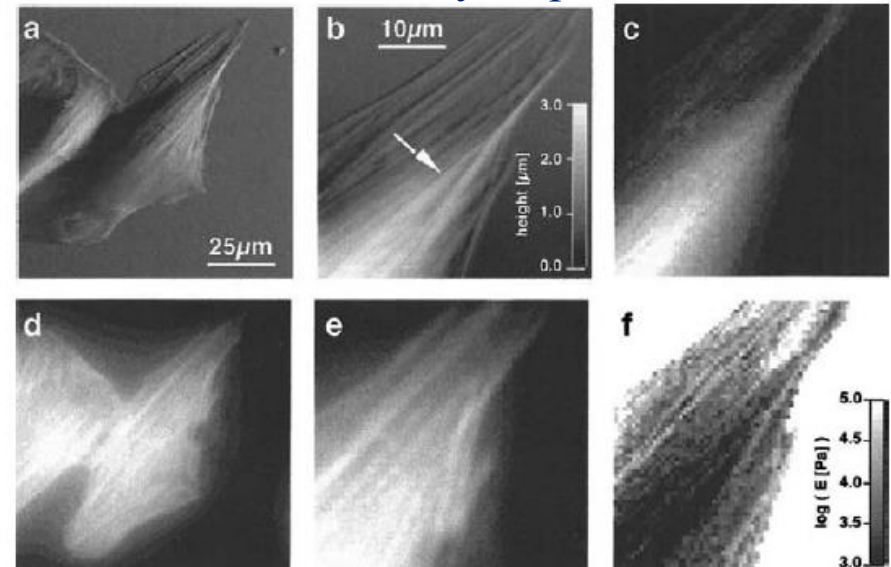
Networks of neurons



Properties of bones



Elasticity maps



W. Richard Bowen, Nidal Hilal, Atomic Force Microscopy in Process Engineering: An Introduction to AFM for improved processes and products, Elsevier 2009

Conclusions

- 1) Wide range of properties characterizations: Morphological, Mechanical, Electrical, Magnetic, Thermal, **local** properties (**nanoscale**), and much more.
- 2) Beyond characterizations: **Manipulation and Fabrication**
- 3) Intimate correlation **SPM**↔**Nanoscience and Nanotechnology**

AFM: some measurements

Formation and evolution of self-organized Au nanorings on indium-tin-oxide surface

F. Ruffino,^{1,2,a)} I. Crupi,² F. Simone,^{1,2} and M. G. Grimaldi^{1,2}

¹*Dipartimento di Fisica e Astronomia, Università di Catania, via S. Sofia 64, 95123 Catania, Italy*

²*MATIS CNR-IMM, via S. Sofia 64, 95123 Catania, Italy*

(Received 20 October 2010; accepted 18 December 2010; published online 10 January 2011)

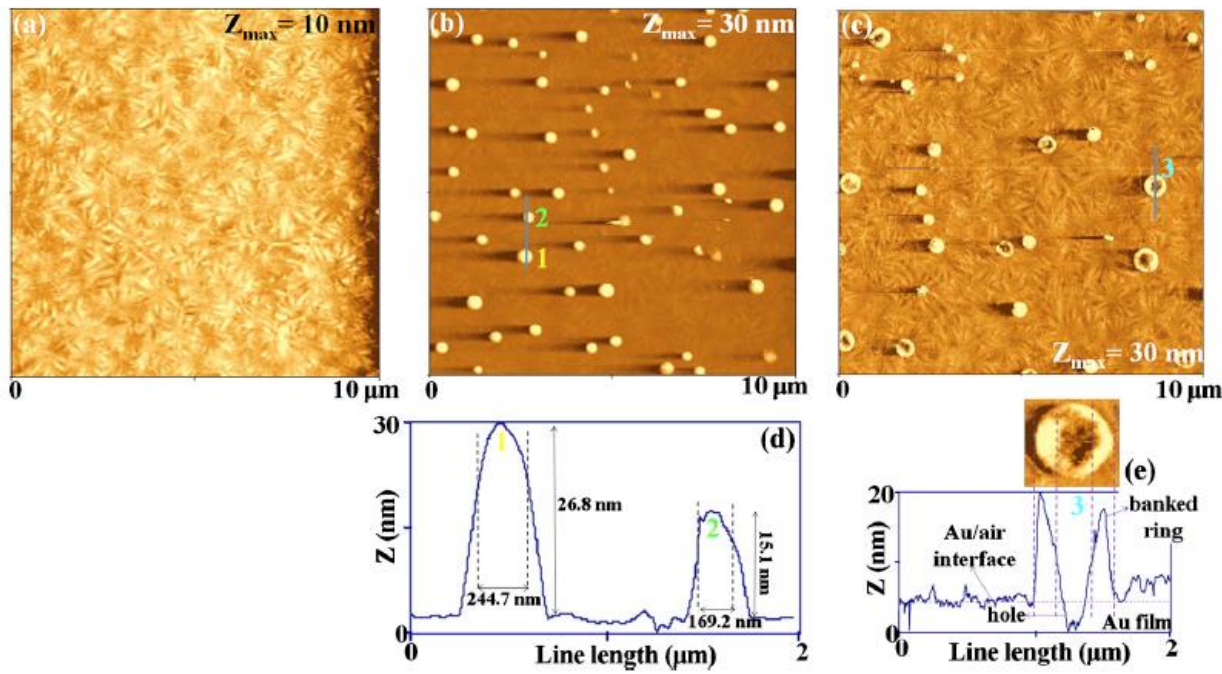


FIG. 1. (Color online) 10 μm × 10 μm AFM image of (a) the starting ITO surface, (b) 25 nm of Au sputter-deposited on the ITO surface, (c) 25 nm of Au sputter-deposited on the ITO surface annealed at 573 K-3600 s. (d) Cross-sectional AFM line-scanning profile of three NCs labeled as 1, and 2 in (b). (e) Cross-sectional AFM line-scanning profile of the NR labeled as 3 in (c).

NANO EXPRESS

Open Access

Atomic force microscopy investigation of the kinetic growth mechanisms of sputtered nanostructured Au film on mica: towards a nanoscale morphology control

Francesco Ruffino^{1,2}, Vanna Torrisi^{3*}, Giovanni Marletta³, Maria Grazia Grimaldi^{1,2}

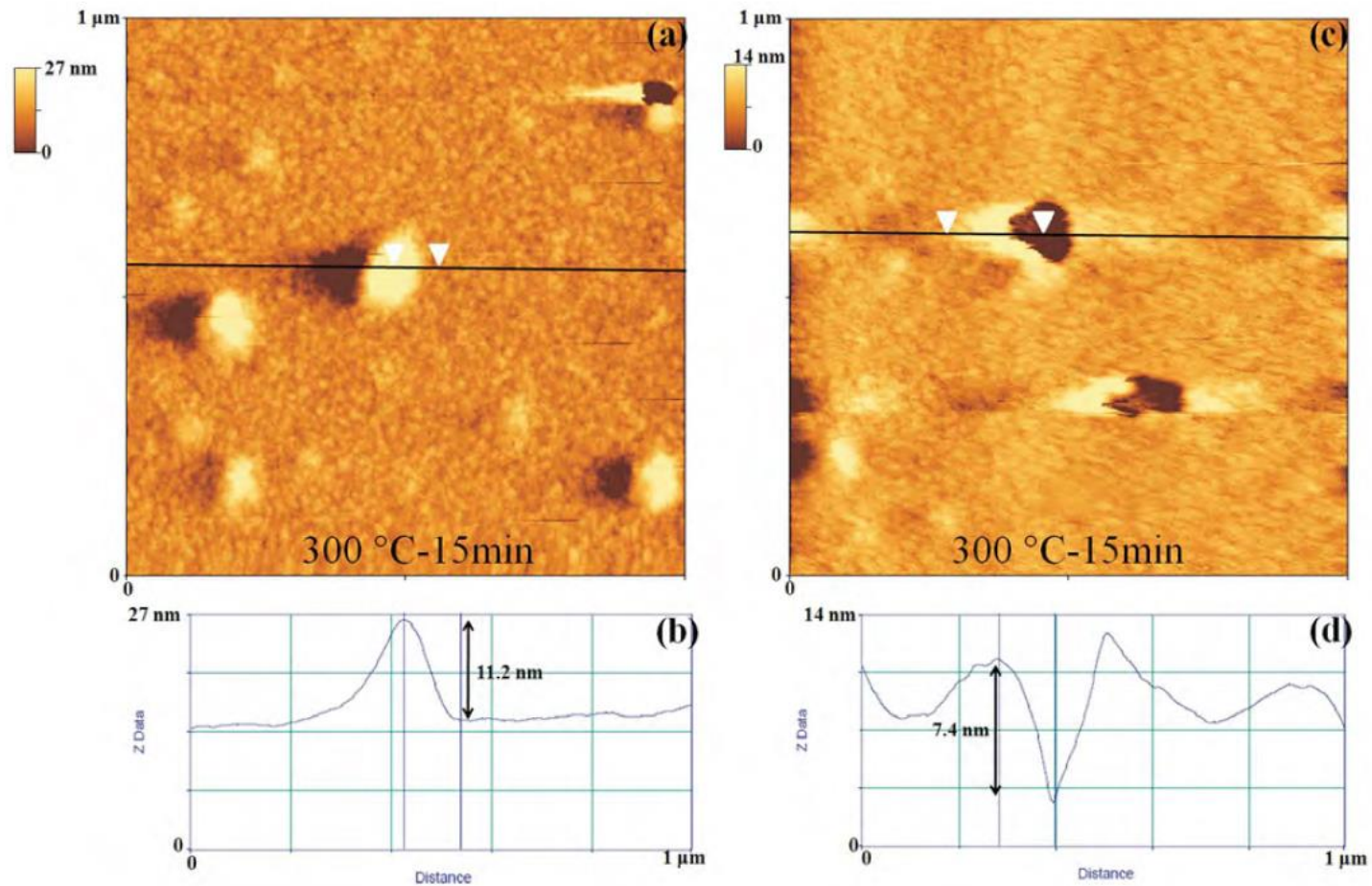


Figure 4 AFM images and section measurements of the thermally processed Au film: (a, c) 1 μm × 1 μm AFM scans of the Au film thermally processed at 573 K-15 min; (b) section measurement to estimate the height (11.2 nm) of a nucleated Au cluster; (d) section measurement to estimate the depth (7.4 nm) of a hole in the Au film.

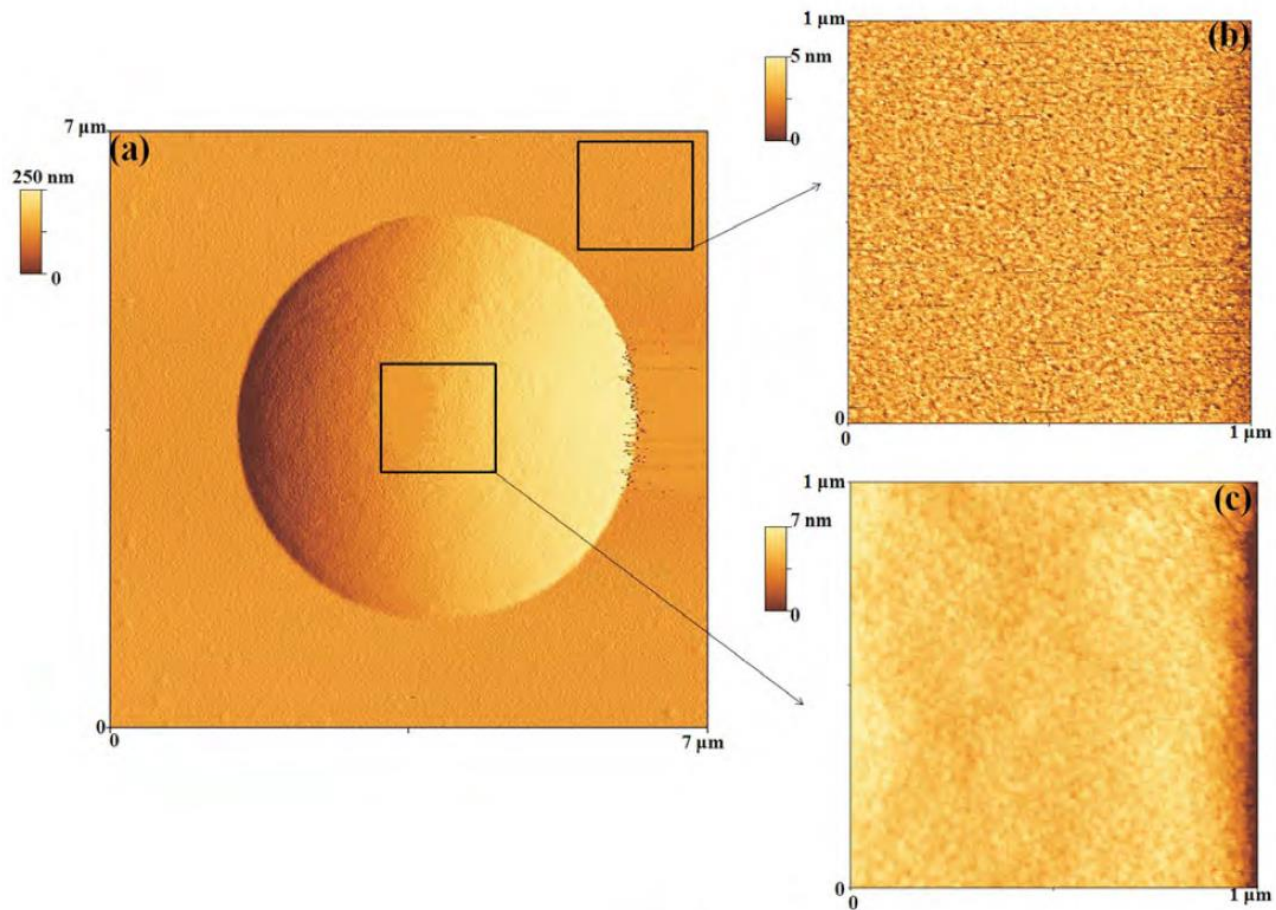


Figure 6 AFM image of a single Au cluster: (a) $7\ \mu\text{m} \times 7\ \mu\text{m}$ AFM scan of the Au film thermally processed at 773 K-60 min, focusing, in particular, on an Au cluster; (b) $1\ \mu\text{m} \times 1\ \mu\text{m}$ AFM scan of the underlying Au film; (c) $1\ \mu\text{m} \times 1\ \mu\text{m}$ AFM scan on the Au cluster, evidencing its granular structure.

Torrisi et al. *Nanoscale Research Letters* 2011, **6**:167
<http://www.nanoscalereslett.com/content/6/1/167>

 **Nanoscale Research Letters**
a SpringerOpen Journal

NANO EXPRESS

Open Access

Memory effects in annealed hybrid gold nanoparticles/block copolymer bilayers

Vanna Torrisi^{1*}, Francesco Ruffino², Antonino Licciardello¹, Maria Grazia Grimaldi², Giovanni Marletta¹

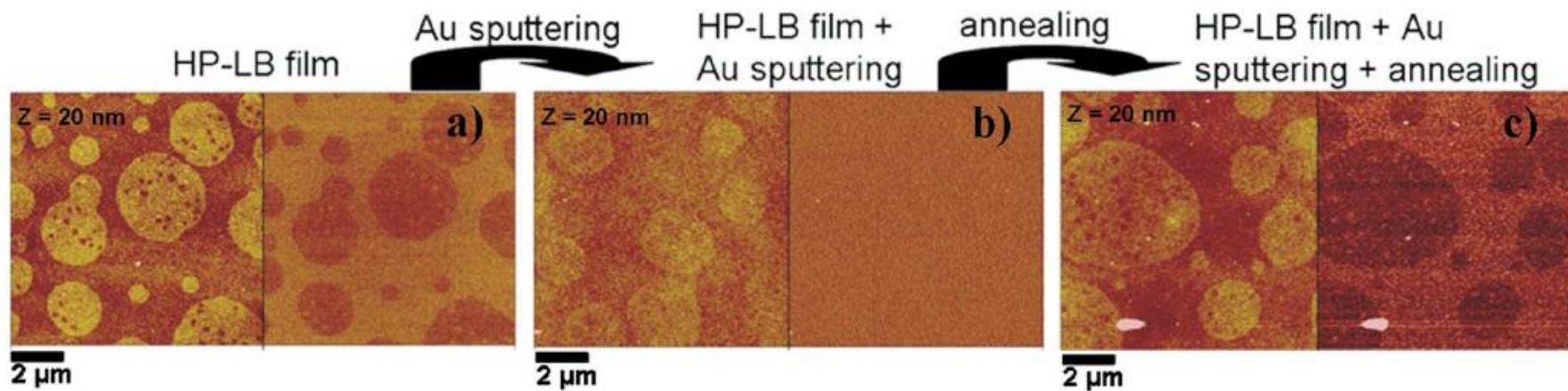


Figure 2 AFM images of the three steps of sample preparation: (a) HP-LB film of *PnBuA-b-PAA*; (b) HP-LB film covered with Au nanoparticles deposited by sputtering; (c) annealed bilayer (115°C, 15 min).



AMERICAN
SCIENTIFIC
PUBLISHERS

Copyright © 2012 by American Scientific Publishers

All rights reserved.

Printed in the United States of America

Science of Advanced Materials

Vol. 4, pp. 708–718, 2012

www.aspbs.com/sam

Formation and Evolution of Nanoscale Metal Structures on ITO Surface by Nanosecond Laser Irradiations of Thin Au and Ag Films

F. Ruffino^{1,2,*}, E. Carria^{1,2}, S. Kimiagar^{1,3}, I. Crupi², F. Simone^{1,2}, and M. G. Grimaldi^{1,2}

¹*Dipartimento di Fisica ed Astronomia-Università di Catania, via S. Sofia 64, 95123 Catania, Italy*

²*MATIS IMM-CNR, via S. Sofia 64, 95123 Catania, Italy*

³*Islamic Azad University, Central Tehran Branch, Tehran, Iran*

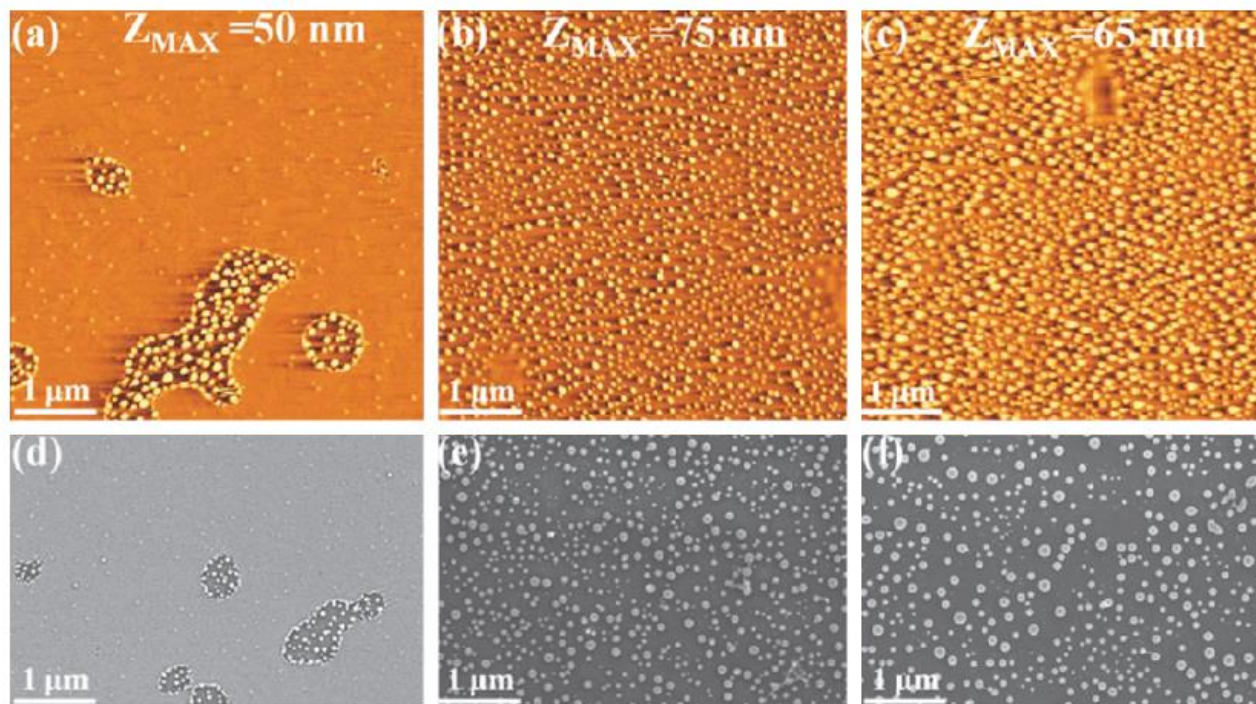


Fig. 2. AFM ((a)–(c)) and SEM ((d)–(f)) images of the 5 nm thick Au film on ITO irradiated by 500 mJ/cm² ((a) and (d)), 750 mJ/cm² ((b) and (e)), 1000 mJ/cm² ((c) and (f)).

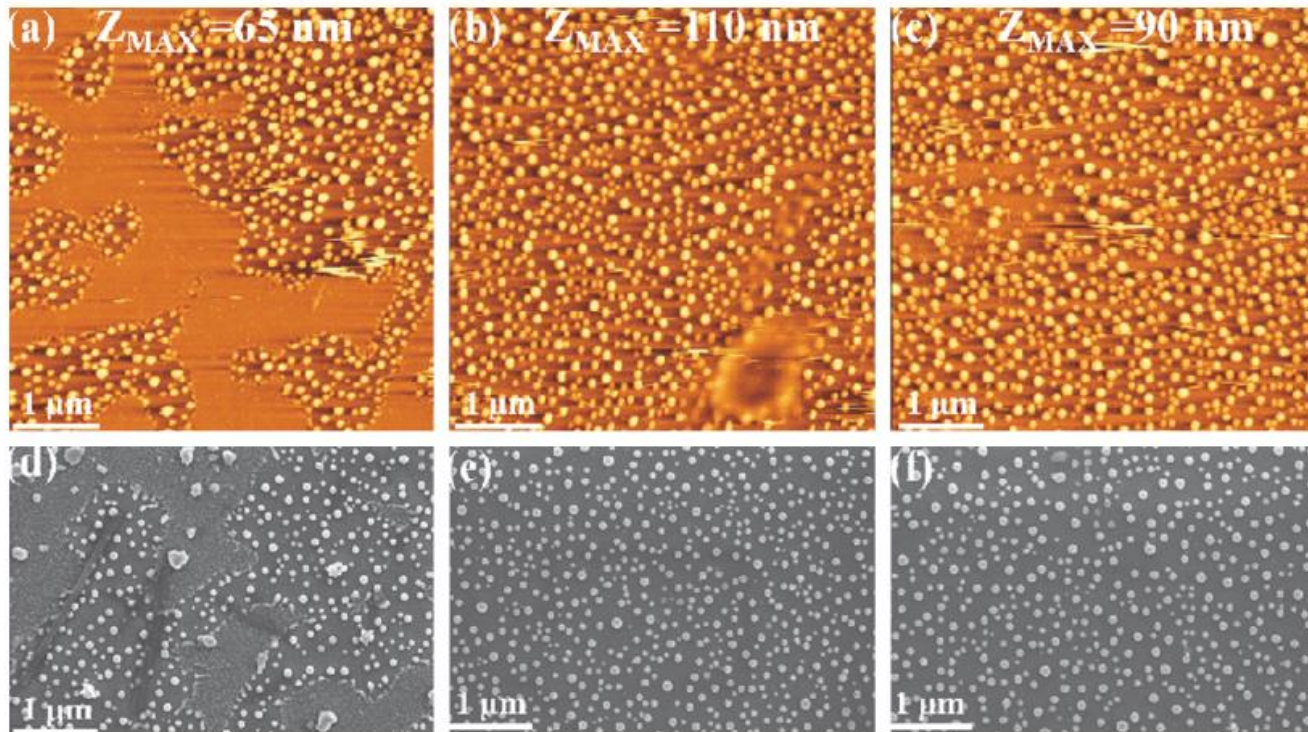
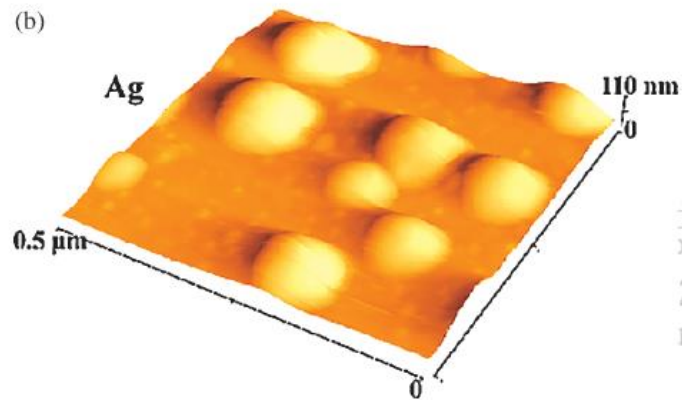
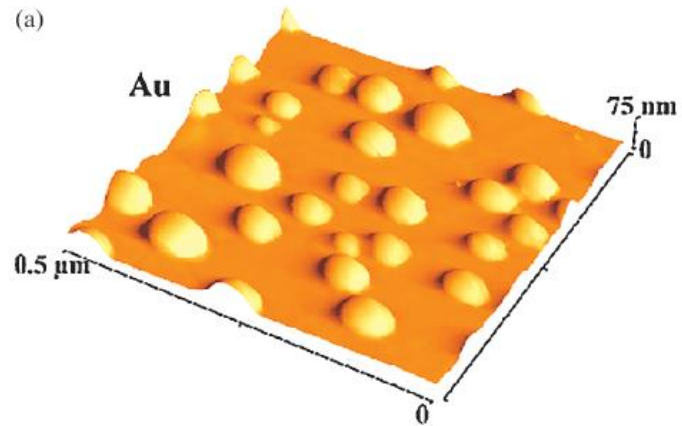


Fig. 3. AFM ((a)–(c)) and SEM ((d)–(f)) images of the 5 nm thick Ag film on ITO irradiated by 500 mJ/cm² ((a) and (d)), 750 mJ/cm² ((b) and (e)), 1000 mJ/cm² ((c) and (f)).



i by
olyt
29.10
il 20

Fig. 4. Three-dimensional reconstructions of $0.5 \mu\text{m} \times 0.5 \mu\text{m}$ AFM images the (a) Au and (b) Ag films irradiated by $750 \text{ mJ}/\text{cm}^2$.

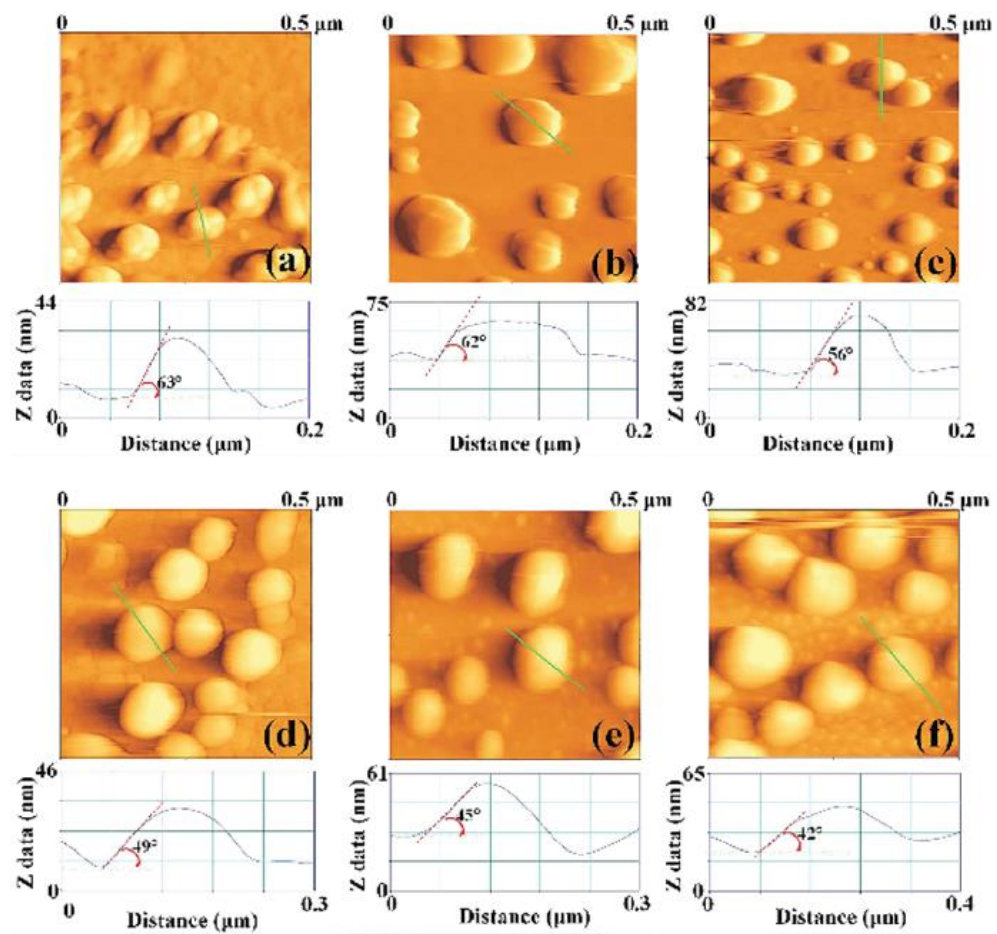


Fig. 8. $0.5 \mu\text{m} \times 0.5 \mu\text{m}$ AFM images of the samples and line profile sections of representative isolate NCs for the contact angle measurements: (a)–(c) Au film irradiated by 500 (a), 750 (b), and 1000 mJ/cm² (c); (d)–(f) Ag film irradiated by 500 (d), 750 (e), and 1000 mJ/cm² (f).

Structural and optical properties of highly Er-doped Yb-Y disilicate thin films

**Paolo Cardile,¹ Maria Miritello,^{1,*} Francesco Ruffino,^{1,2}
and Francesco Priolo^{1,2}**

¹CNR-IMM MATIS, via S. Sofia 64, I-95123 Catania, Italy

²Dipartimento di Fisica e Astronomia, Università di Catania, via S. Sofia 64, I-95123 Catania, Italy

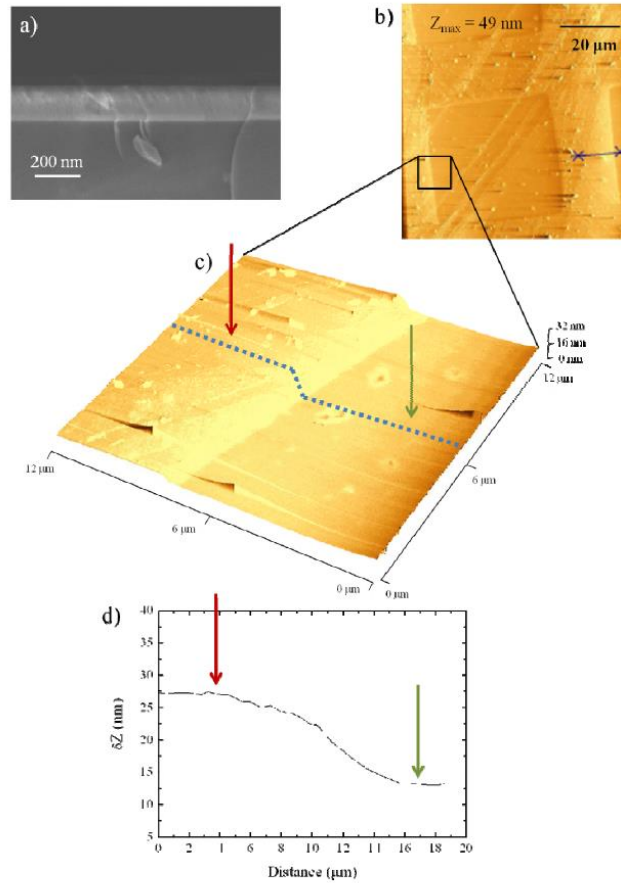


Fig. 2. (a) Cross sectional SEM image of an as deposited Yb-Y disilicate. (b) AFM measurements on an as-implanted sample, after removing a masking grating. (c) AFM zoom-in reporting the step height in a 3D picture. (d) Analytical measurement of the step height.

Fig. 2 a Scheme of the normal deposition ($\alpha = 0^\circ$) configuration and of the expected pattern of the Au and Ag films (cross-section view). b Scheme of the oblique deposition ($\alpha = 42^\circ$) configuration and of the expected pattern of the Au and Ag films (cross-section view)

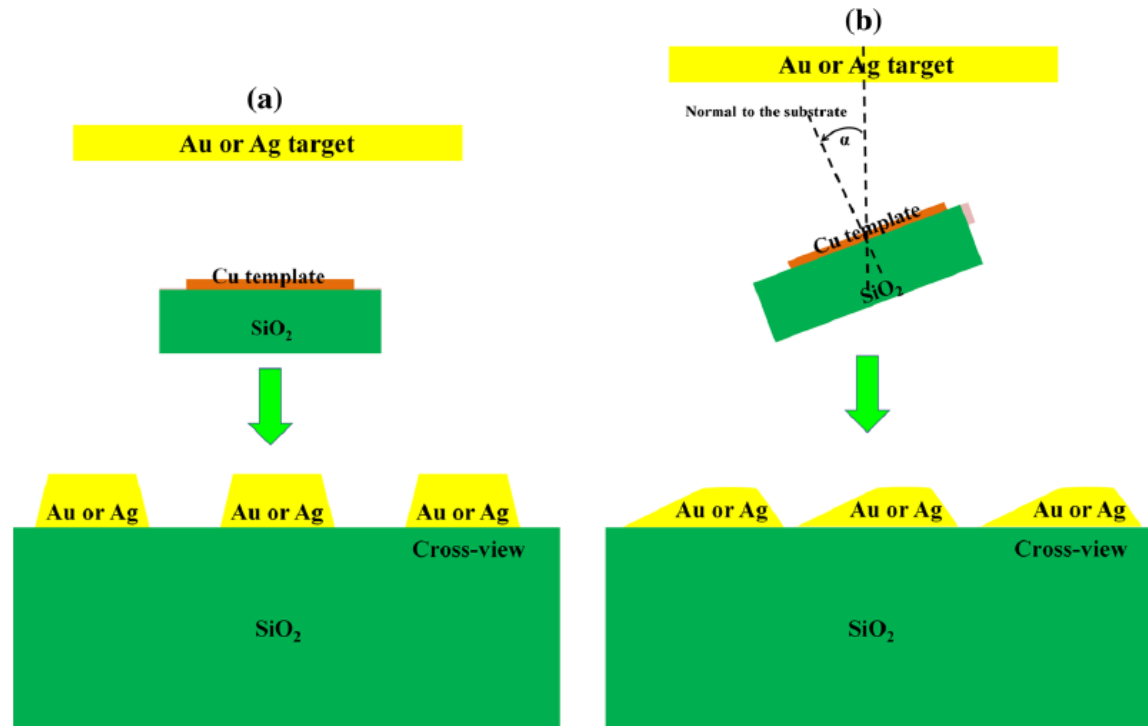


Fig. 3 **a** Two-dimensional AFM scan ($20\ \mu\text{m} \times 20\ \mu\text{m}$) of the 40 nm-thick Au film deposited through the lithographic mask in normal condition ($\alpha = 0^\circ$). **b** Three-dimensional reconstruction of the AFM image in (a). **c** Cross-line profile of a Au square corresponding to the *red line* in (a). From this symmetric cross-line profile, from the center to the edge the square is divided in four regions assigning to each region an effective height $\langle h_{ij} \rangle$ (d)

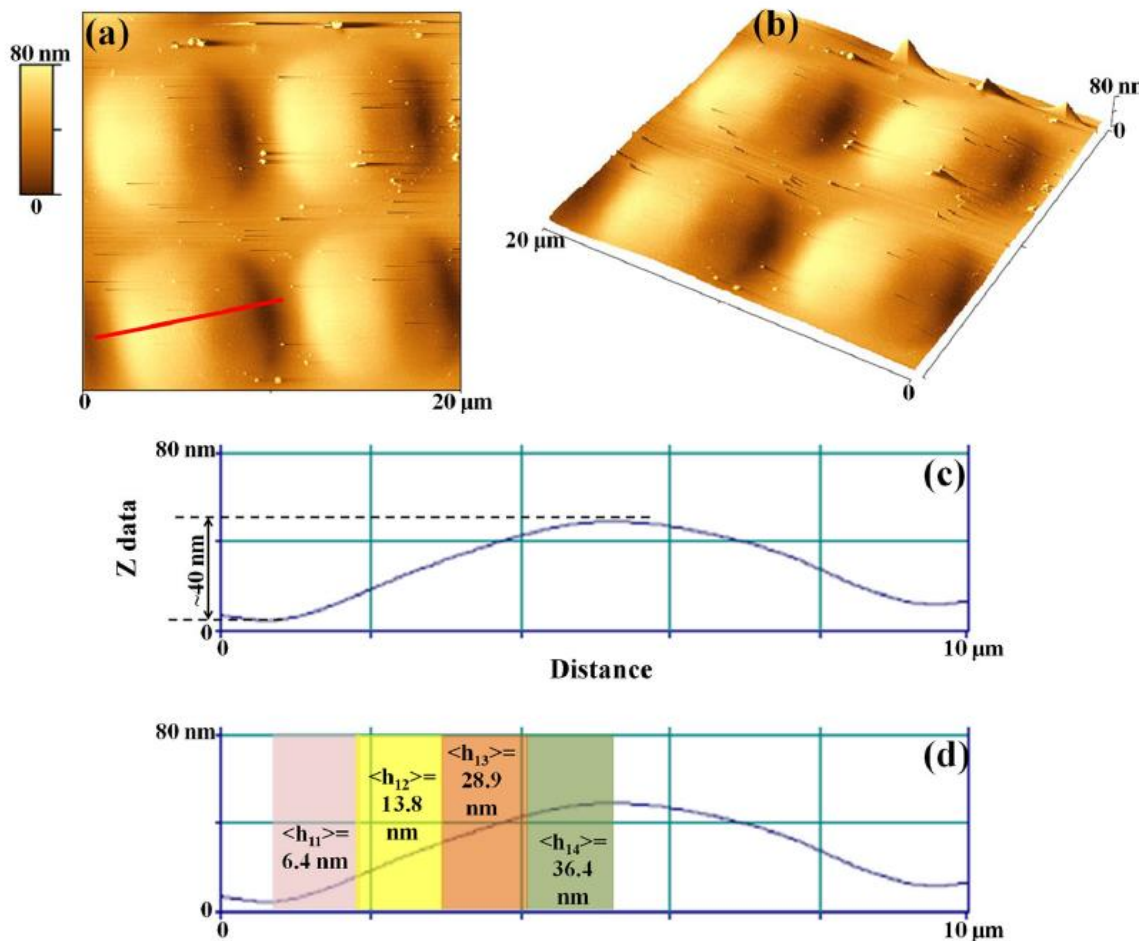
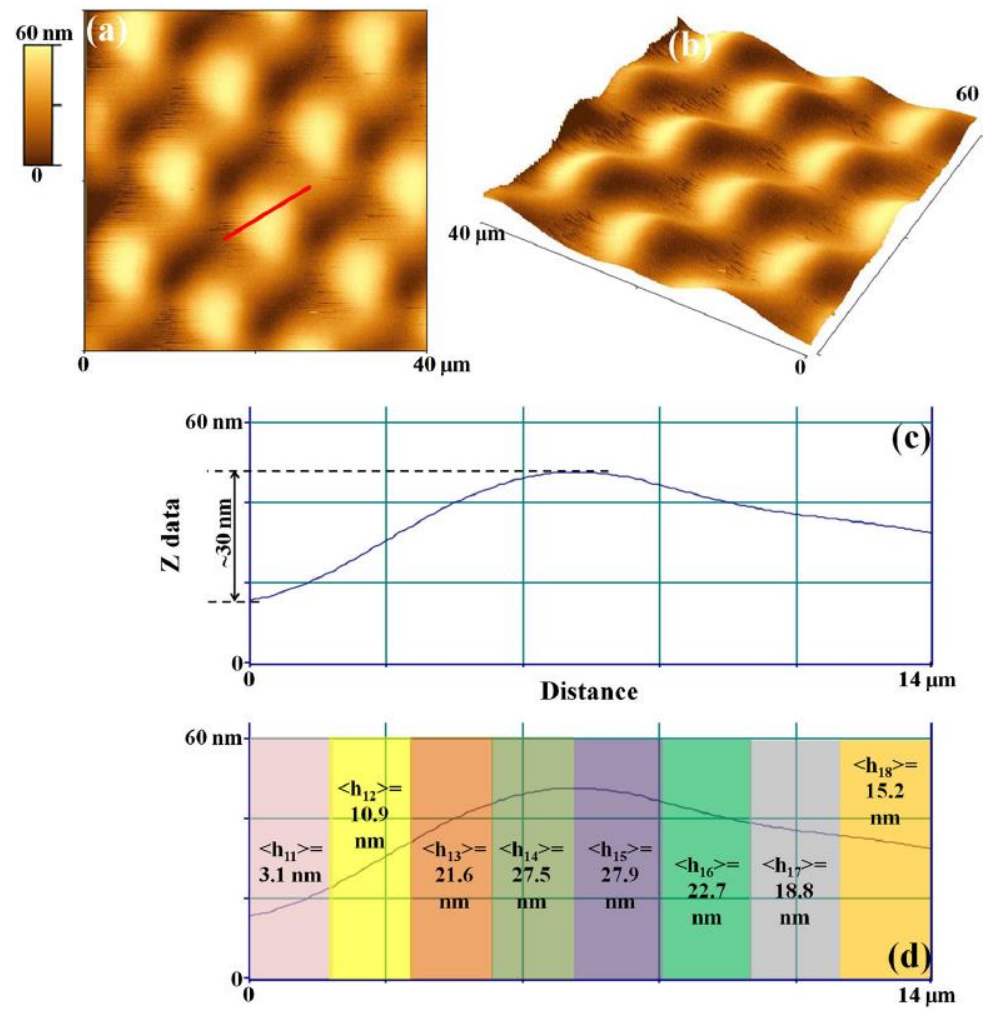


Fig. 4 **a** Two-dimensional AFM scan ($40\ \mu\text{m} \times 40\ \mu\text{m}$) of the 40 nm-thick Au film deposited through the lithographic mask in oblique condition ($\alpha = 42^\circ$). **b** Three-dimensional reconstruction of the AFM image in (a). **c** Cross-line profile of a Au square corresponding to the red line in (a). From this asymmetric cross-line profile, from the center to the edges the square is divided in height regions assigning to each region an effective height $\langle h_{ij} \rangle$ (**d**)



Superlattices and Microstructures 113 (2018) 430–441



ELSEVIER

Contents lists available at [ScienceDirect](#)

Superlattices and Microstructures

journal homepage: www.elsevier.com/locate/superlattices



Roughness evolution in dewetted Ag and Pt nanoscale films

F. Ruffino*, M.G. Grimaldi

Dipartimento di Fisica e Astronomia Università di Catania and MATIS CNR-IMM, Via S. Sofia 64, 95123 Catania, Italy



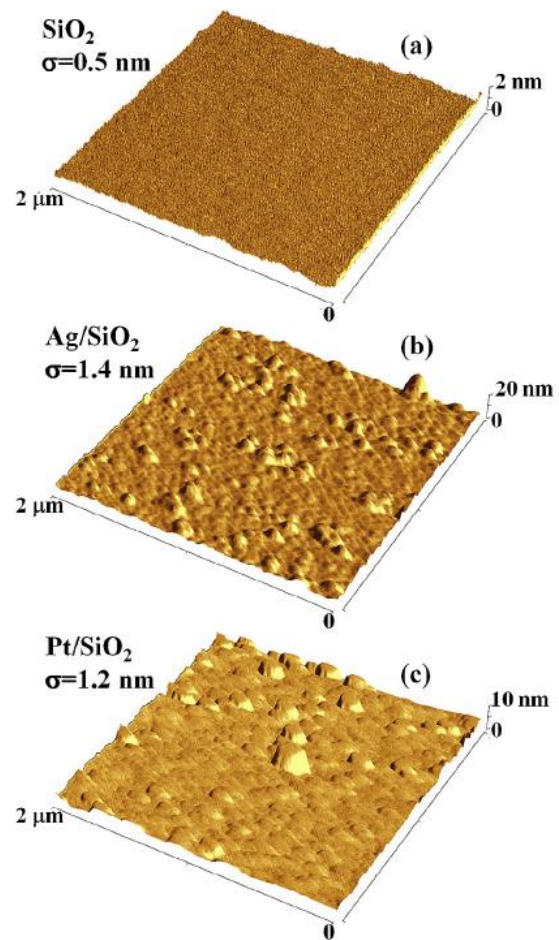


Fig. 1. Representative three-dimensional AFM images ($2\ \mu\text{m} \times 2\ \mu\text{m}$) of: (a) the bare SiO₂ surface, (b) the surface of 15 nm-thick Ag film deposited on the SiO₂ surface, (c) the surface of 15 nm-thick Pt film deposited on the SiO₂ surface. Each image is accompanied by the corresponding value of the roughness σ .

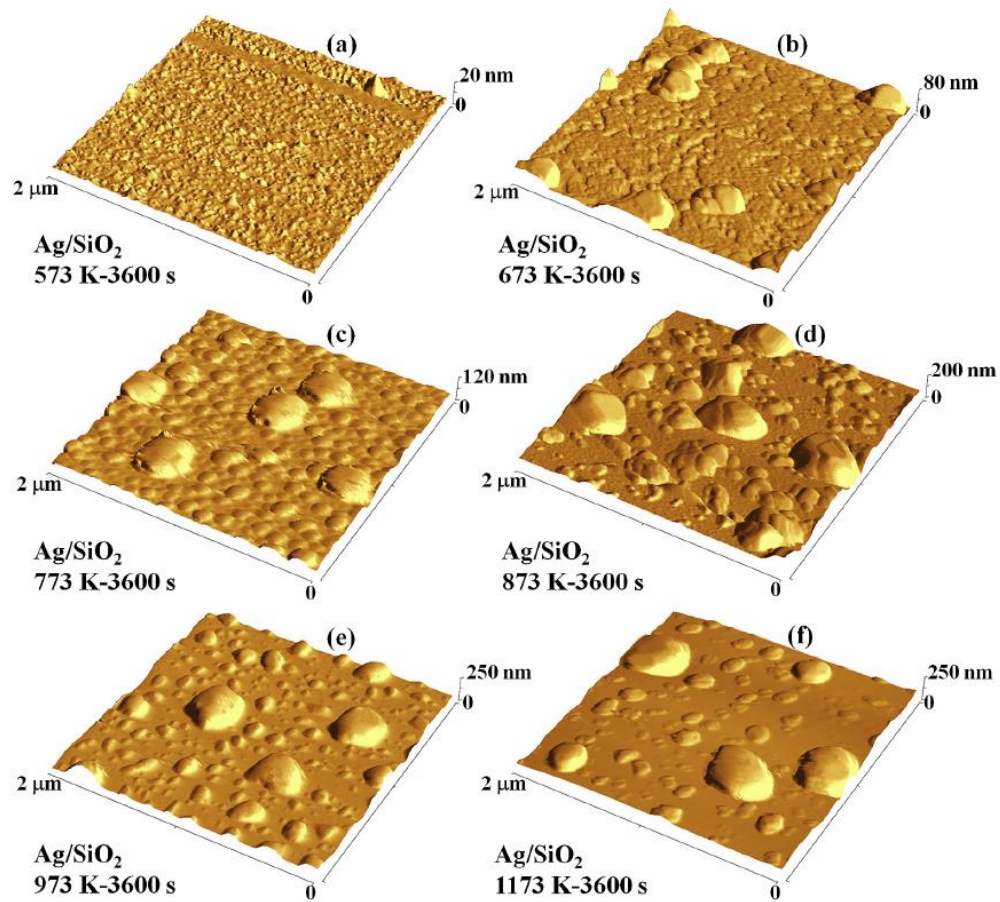


Fig. 2. Representative three-dimensional AFM images ($2\ \mu\text{m} \times 2\ \mu\text{m}$) of the 15 nm-thick Ag film deposited on the SiO_2 surface and thermally processed at: (a) 573 K-3600 s, (b) 673 K-3600 s, (c) 773 K-3600 s, (d) 873 K-3600 s, (e) 973 K-3600 s, (f) 1173 K-3600 s. These images allow to follow the evolution of the Ag film morphology versus the annealing temperature.

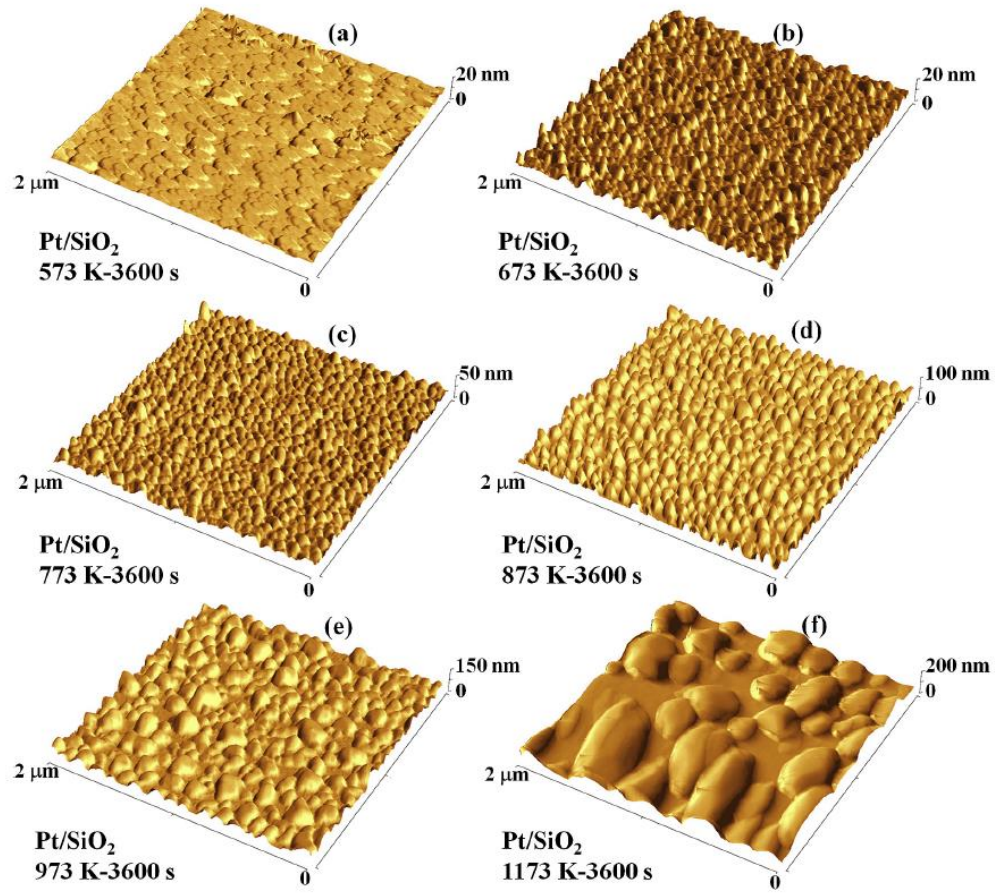


Fig. 3. Representative three-dimensional AFM images ($2\ \mu\text{m} \times 2\ \mu\text{m}$) of the 15 nm-thick Pt film deposited on the SiO₂ surface and thermally processed at: (a) 573 K-3600 s, (b) 673 K-3600 s, (c) 773 K-3600 s, (d) 873 K-3600 s, (e) 973 K-3600 s, (f) 1173 K-3600 s. These images allow to follow the evolution of the Pt film morphology versus the annealing temperature.

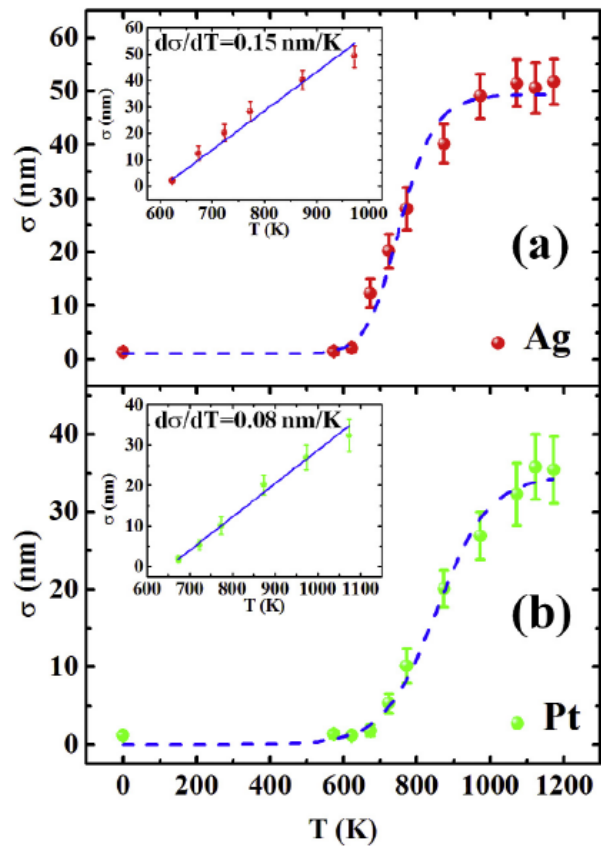


Fig. 4. Plots of the roughness σ versus the annealing temperature T when fixed the annealing time $t = 3600$ s, for the 15 nm-thick Ag film (a) and the 15 nm-thick Pt film (b). The insets report σ versus T restricted to the linear regions and the blue lines represent the corresponding linear fits of the experimental data.

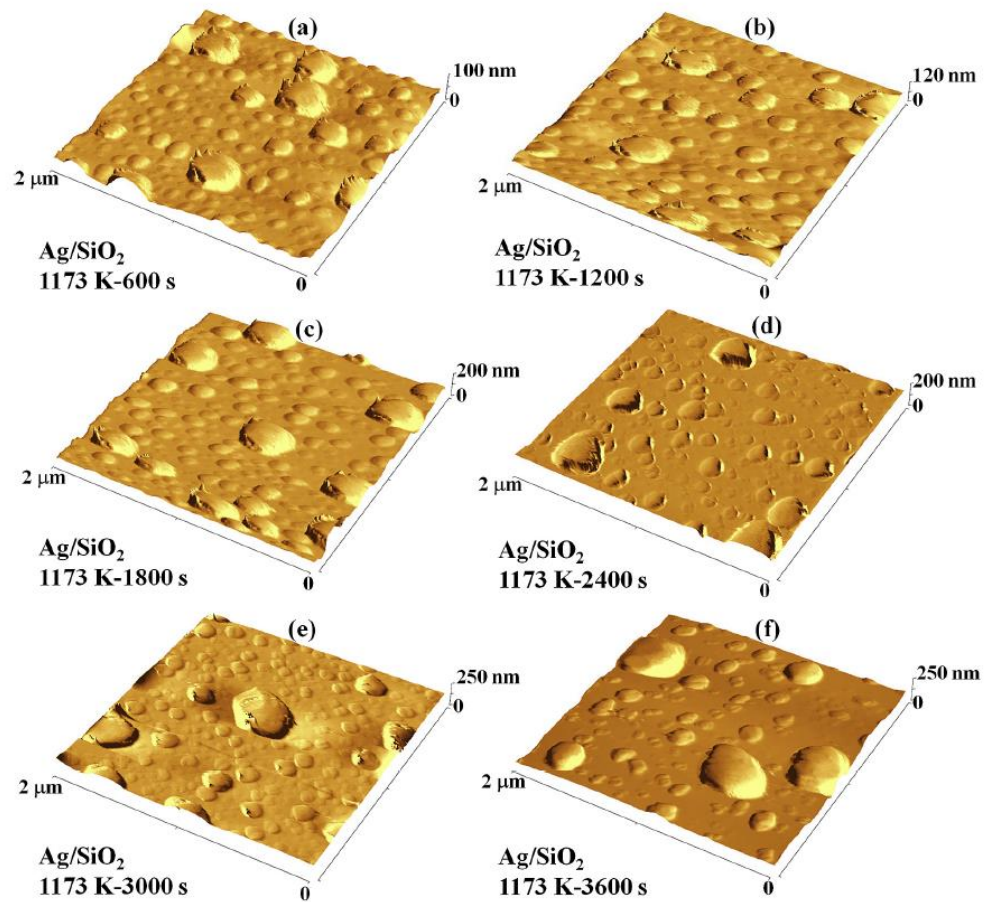


Fig. 5. Representative three-dimensional AFM images ($2\ \mu\text{m} \times 2\ \mu\text{m}$) of the 15 nm-thick Ag film deposited on the SiO₂ surface and thermally processed at: (a) 1173 K-600 s, (b) 1173 K-1200 s, (c) 1173 K-1800 s, (d) 1173 K-2400 s, (e) 1173 K-3000 s, (f) 1173 K-3600 s. These images allow to follow the evolution of the Ag film morphology versus the annealing time.

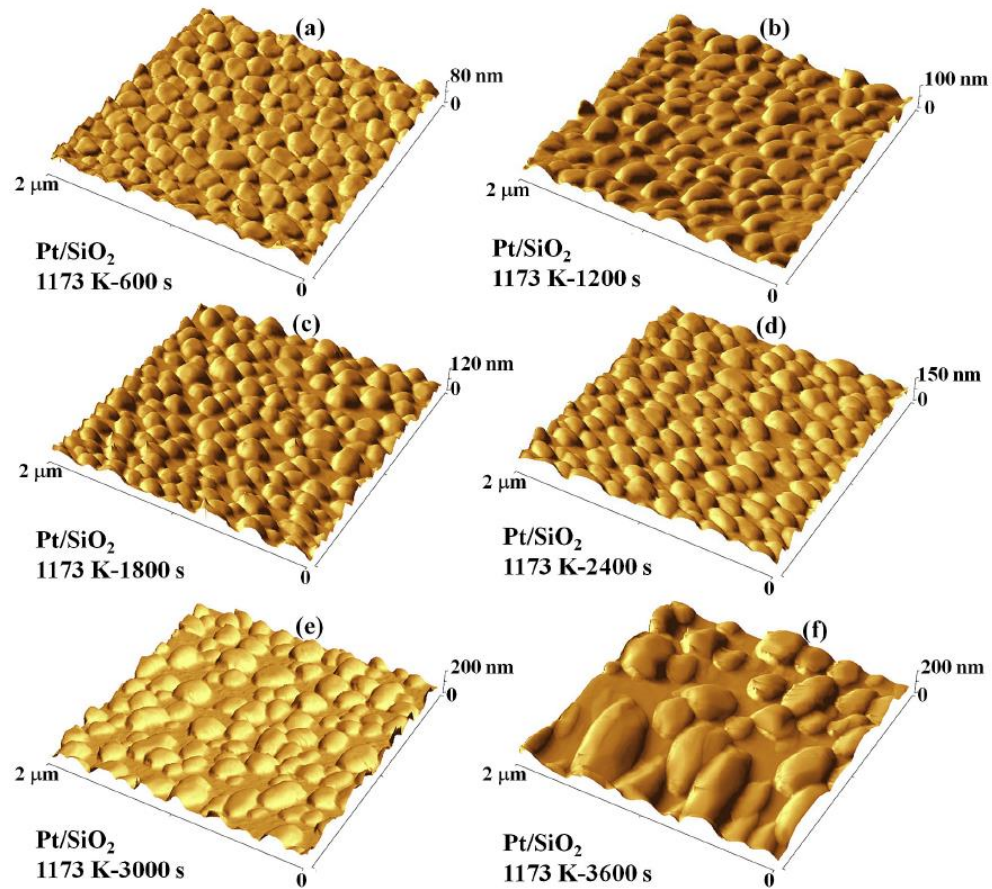


Fig. 6. Representative three-dimensional AFM images ($2\ \mu\text{m} \times 2\ \mu\text{m}$) of the 15 nm-thick Pt film deposited on the SiO₂ surface and thermally processed at: (a) 1173 K-600 s, (b) 1173 K-1200 s, (c) 1173 K-1800 s, (d) 1173 K-2400 s, (e) 1173 K-3000 s, (f) 1173 K-3600 s. These images allow to follow the evolution of the Pt film morphology versus the annealing time.

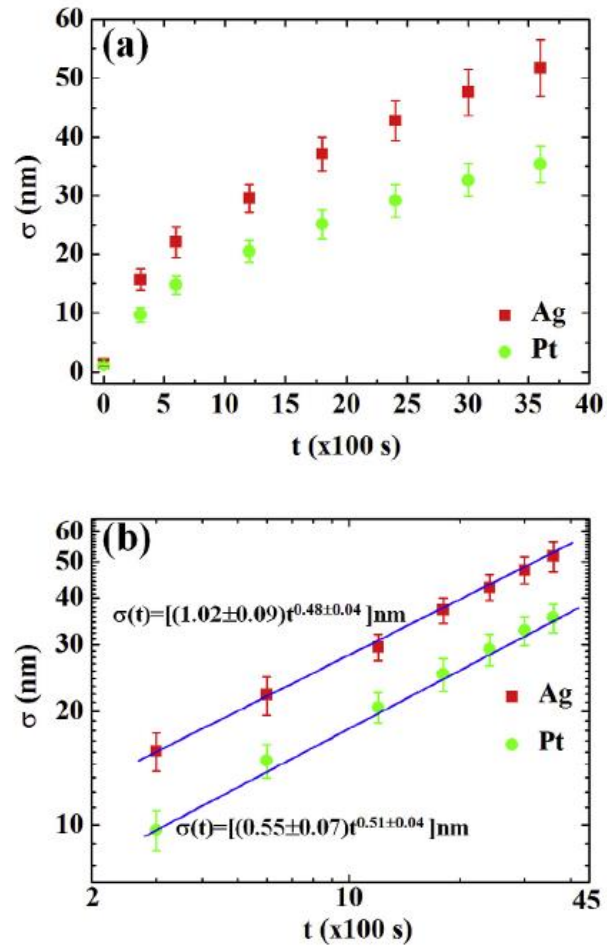


Fig. 7. (a) Plots of the roughness σ versus the annealing time t when fixed the annealing temperature $T = 1173$ K, for the 15 nm-thick Ag film and the 15 nm-thick Pt film. (b) Reports the same experimental data (apart the value for $t = 0$ s) plotted in Log-Log scale and the continuous lines indicate the fit of the experimental data by $\sigma(t) = \alpha t^\beta$ from which values for the fitting parameters α and β are extracted.



ELSEVIER

Contents lists available at ScienceDirect

Solid State Communications

journal homepage: www.elsevier.com/locate/ssc



Nanoscale electrical characteristics of metal (Au, Pd)–graphene–metal (Cu) contacts



F. Ruffino ^{a,b,*}, G. Meli ^a, M.G. Grimaldi ^{a,b}

^a Dipartimento di Fisica ed Astronomia-Università di Catania, via S. Sofia 64, 95123 Catania, Italy

^b MATIS IMM-CNR, via S. Sofia 64, 95123 Catania, Italy

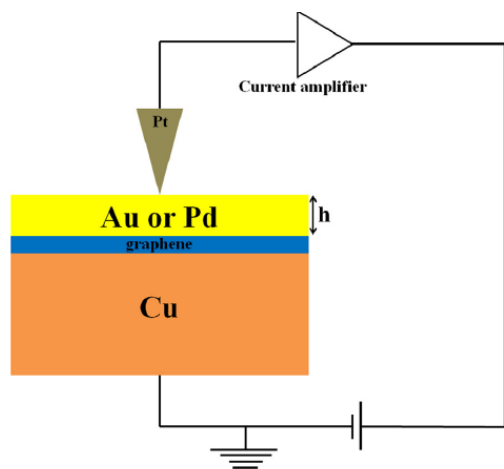


Fig. 2. Picture of the analyzed samples and conductive atomic force microscopy measurement setup configuration.

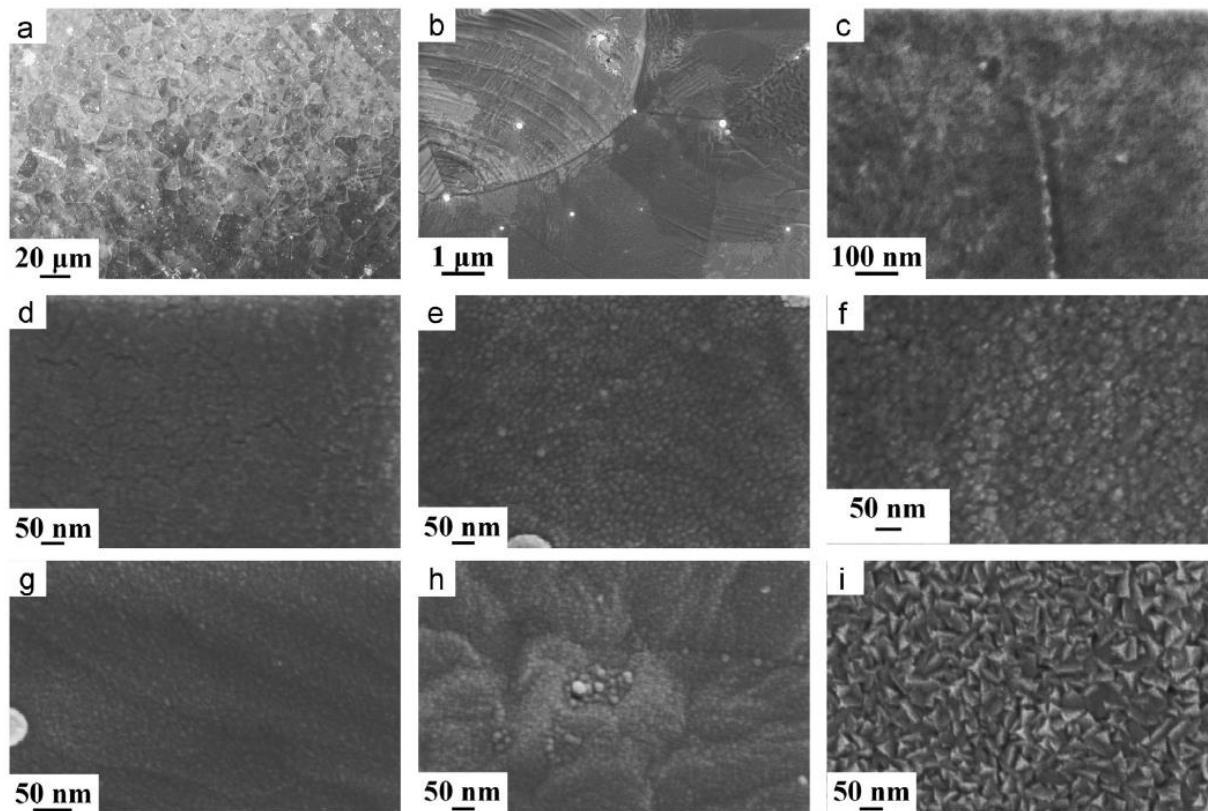
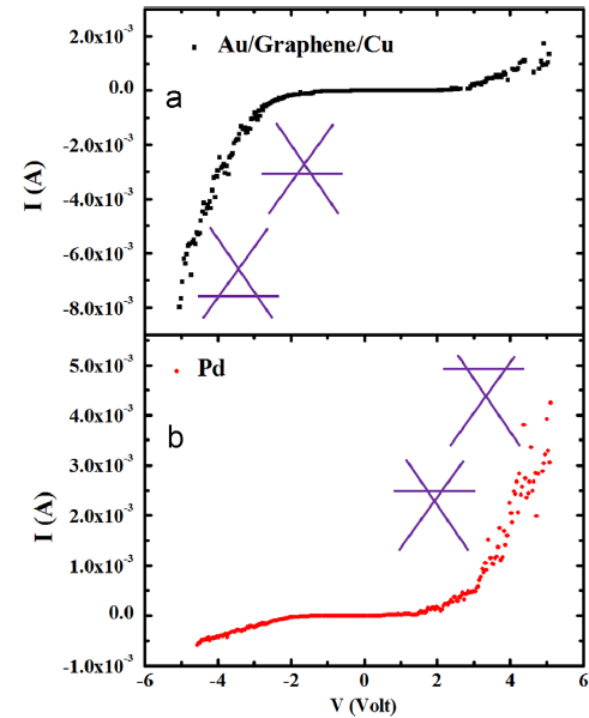
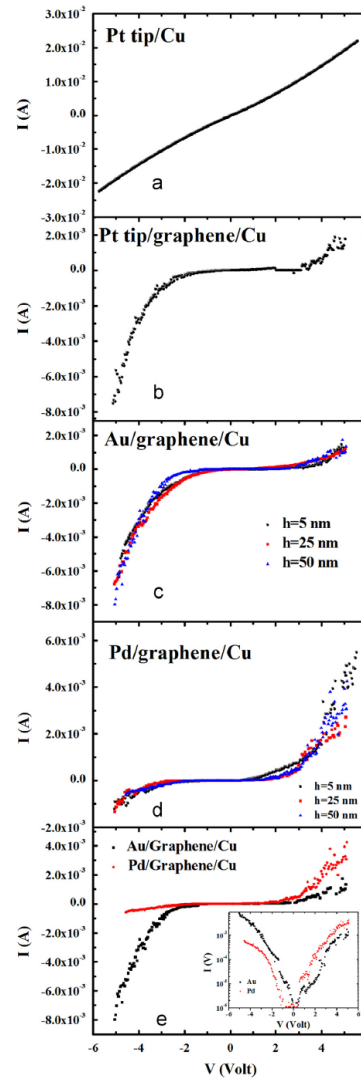


Fig. 3. Representative scanning electron microscopy images of: (a)–(c) graphene/Cu surface at different magnifications, (d)–(f) Au films deposited on the graphene/Cu surface with thickness of 5 nm (d), 25 nm (e) and 50 nm (f), (g)–(i) Pd films deposited on the graphene/Cu surface with thickness of 5 nm (g), 25 nm (h) and 50 nm (i).

Table 1
 W_M : metal work-function, W_G : free-standing graphene work-function (4.48 eV) and graphene work-function when in contact with a specific metal. Adapted from [18].

	Gr	Pd	Cu	Au	Pt
$W_M(\text{eV})$		5.67	5.22	5.54	6.13
$W_G(\text{eV})$	4.48	4.03	4.40	4.74	4.87





Contents lists available at [ScienceDirect](#)

Applied Surface Science

journal homepage: www.elsevier.com/locate/apsusc



Emerging interface dipole *versus* screening effect in copolymer/metal nano-layered systems



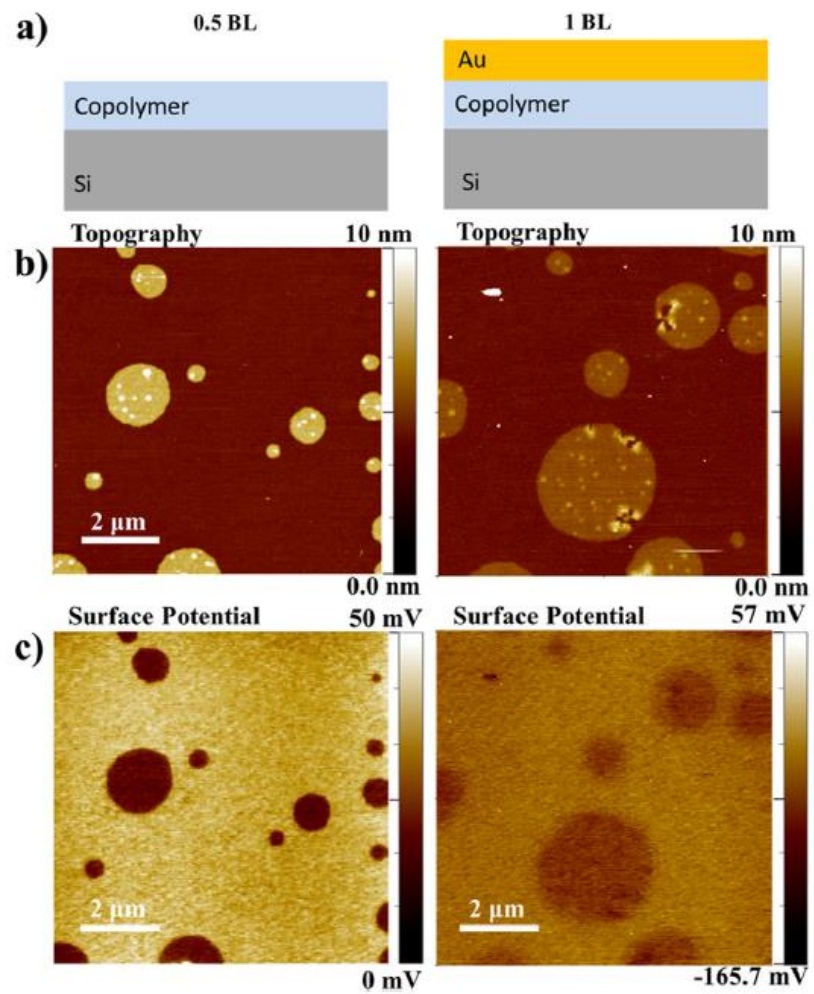
V. Torrìsi^{a,*}, F. Ruffino^{b,c}, A. Liscio^d, M.G. Grimaldi^{b,c}, G. Marletta^a

^a *Laboratory for Molecular Surfaces and Nanotechnology (LAMSUN), Department of Chemical Sciences, University of Catania, Viale A. Doria 6, 95125, Catania, Italy*

^b *Dipartimento di Fisica ed Astronomia-Università di Catania, via S. Sofia 64, 95123 Catania, Italy*

^c *MATIS IMM-CNR, via S. Sofia 64, 95123 Catania, Italy*

^d *Istituto per la Sintesi e la Fotoreattività CNR, via Gobetti 101, 40129, Bologna, Italy*

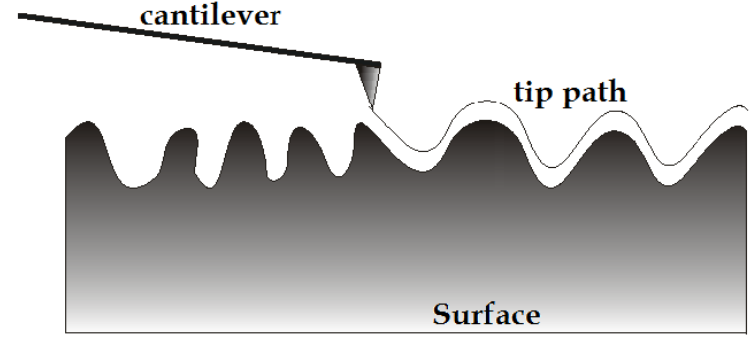


AFM: surface roughness

ence surface. Films grown under nonequilibrium condition are expected to develop self-affine surfaces [7, 14], whose rms widths scale with time t and the length L sampled as [15]

$$\sigma(L, t) = L^\alpha F\left(t/L^{\alpha/\beta}\right) \quad (1)$$

where $\sigma(L) \propto L^\alpha$ for $t/L^{\alpha/\beta} \rightarrow \infty$ and $\sigma(t) \propto t^\beta$ for $t/L^{\alpha/\beta} \rightarrow 0$. The parameter $0 < \alpha < 1$ is defined as the roughness exponent [16], and the parameter, β , as the growth exponent. Actual self-affine surfaces are characterized by an upper horizontal cutoff to scaling, or correlation length, ξ , beyond which the surface width no longer scales as L^α , and eventually reaches a saturation



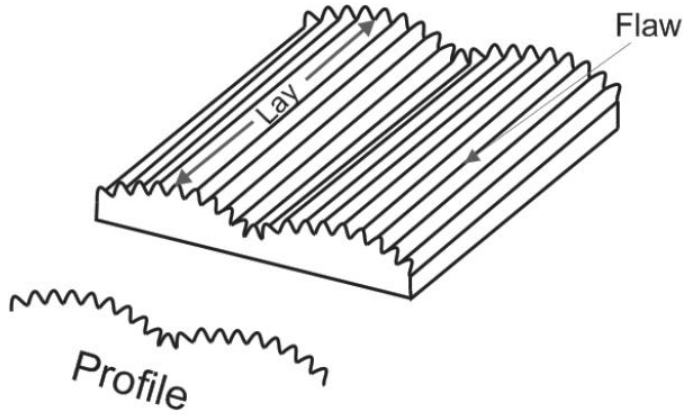
value, σ . Implicit in Eq. 1 is a correlation length which increases with time as $\xi \propto t^{1/z}$, where $z = \alpha/\beta$ is the dynamic scaling exponent.

In thin films deposition methodologies in which the film thickness, h , is proportional to the time of deposition, t , then, in the asymptotical limits,

$$\sigma(h) = ah^\beta \quad (2)$$

$$\xi(h) = bh^{1/z} \quad (3)$$

where a and b are the opportune proportionality constants.



The global surface morphology thus proceeds to a steady growth with the evolution of vertical roughening and lateral coarsening. Two correlation lengths are assigned to describe the interface growth process: the mean surface height fluctuations σ , which is a measure of the vertical interface roughness, and the lateral correlation length ξ , which characterizes the coarsening size. In particular, the roughness function is defined by³⁰

$$\sigma = \langle z(x,y)^2 \rangle^{1/2} = \langle [h(x,y) - \langle h(x,y) \rangle]^2 \rangle^{1/2}, \quad (6)$$

where $h(x,y)$ is the height function and $\langle \dots \rangle$ is the spatial average over a planar reference surface. The roughness σ of a real self-affine surface must saturate at large length scales, and the correlation length ξ is the horizontal cutoff associated with the saturation value of σ . For a growing film, the time evolution of the saturated σ is characterized by the “growth” exponent³⁰ β ,

$$\sigma \propto \langle h \rangle^\beta. \quad (7)$$

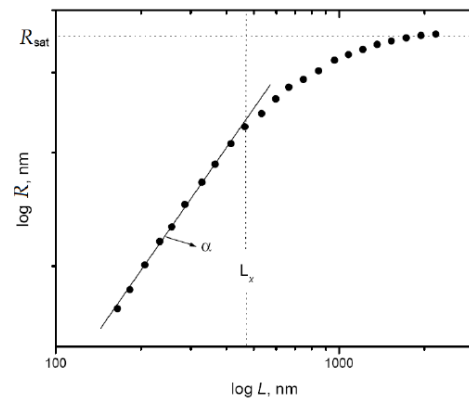
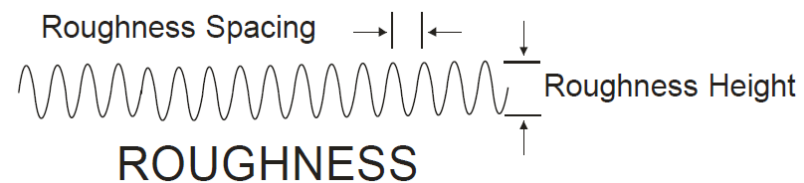


Fig. 25. For self-affine surfaces, the slope of the unsaturated region of roughness is the roughness exponent (Cruz T.G.S., 2002).

Atomic force microscopy study of the growth mechanisms of nanostructured sputtered Au film on Si(111): Evolution with film thickness and annealing time

F. Ruffino^{a)} and M. G. Grimaldi

*Dipartimento di Fisica e Astronomia, Università di Catania, via S. Sofia 64, 95123 Catania, Italy and
CNR-IMM MATIS, via S. Sofia 64, 95123 Catania, Italy*

(Received 19 January 2010; accepted 15 April 2010; published online 26 May 2010)

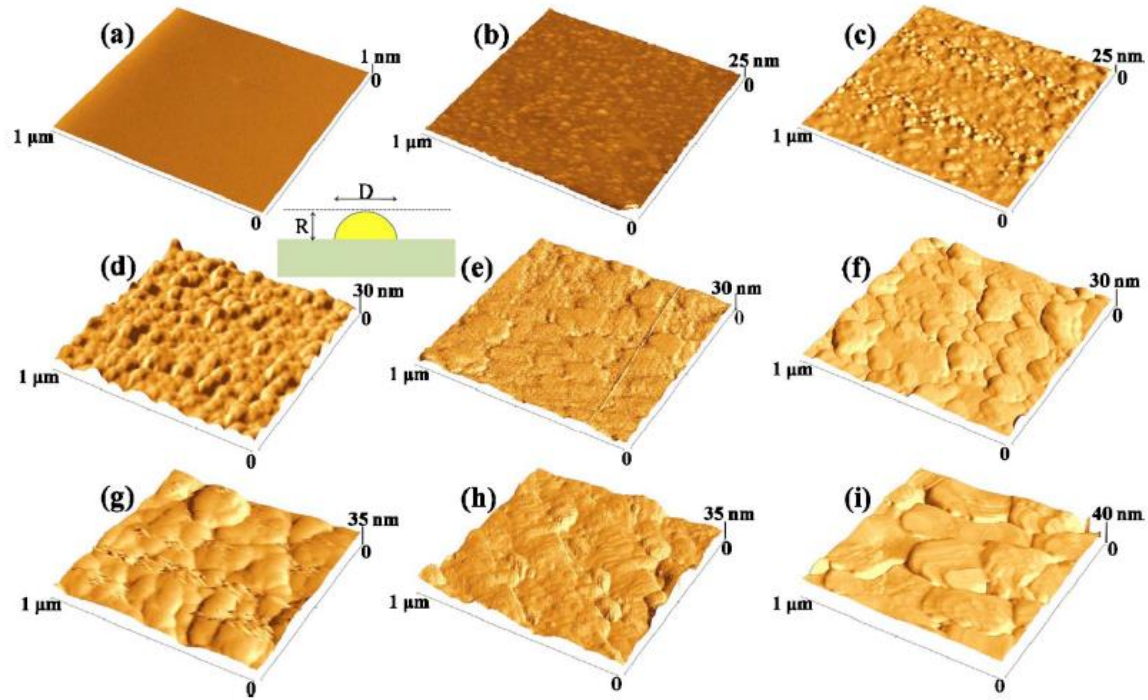


FIG. 1. (Color online) (a) $1 \times 1 \mu\text{m}^2$ AFM image of the Si(111) substrate; $1 \times 1 \mu\text{m}^2$ AFM images of the Si(111) substrate sputter-deposited with Au of different thickness h : (b) $h=1.7 \times 10^{17} \text{ Au/cm}^2$, (c) $h=2.1 \times 10^{17} \text{ Au/cm}^2$, (d) $h=3.0 \times 10^{17} \text{ Au/cm}^2$, (e) $h=5.2 \times 10^{17} \text{ Au/cm}^2$, (f) $h=6.8 \times 10^{17} \text{ Au/cm}^2$, (g) $h=7.7 \times 10^{17} \text{ Au/cm}^2$, (h) $h=9.4 \times 10^{17} \text{ Au/cm}^2$, and (i) $h=1.0 \times 10^{18} \text{ Au/cm}^2$. The inset shows a schematic of the horizontal, D , and vertical, R , dimensions of the Au clusters.

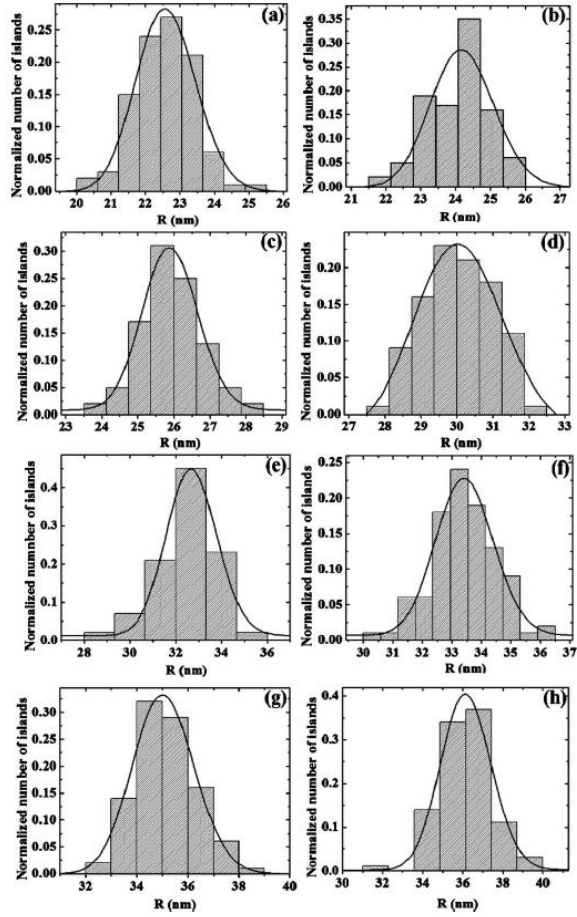


FIG. 2. Distributions of the clusters vertical size R for samples with different amount h of Au: (a) $h=1.7 \times 10^{17}$ Au/cm², (b) $h=2.1 \times 10^{17}$ Au/cm², (c) $h=3.0 \times 10^{17}$ Au/cm², (d) $h=5.2 \times 10^{17}$ Au/cm², (e) $h=6.8 \times 10^{17}$ Au/cm², (f) $h=7.7 \times 10^{17}$ Au/cm², (g) $h=9.4 \times 10^{17}$ Au/cm², and (h) $h=1.0 \times 10^{18}$ Au/cm². The continuous lines are the fits by the log-normal function.

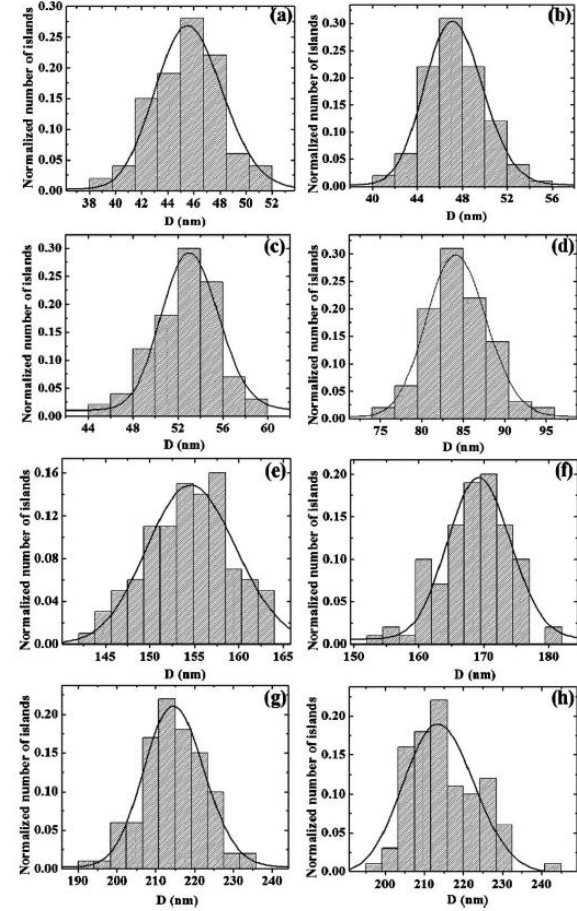


FIG. 3. Distributions of the clusters vertical size D for samples with different amount h of Au: (a) $h=1.7 \times 10^{17}$ Au/cm², (b) $h=2.1 \times 10^{17}$ Au/cm², (c) $h=3.0 \times 10^{17}$ Au/cm², (d) $h=5.2 \times 10^{17}$ Au/cm², (e) $h=6.8 \times 10^{17}$ Au/cm², (f) $h=7.7 \times 10^{17}$ Au/cm², (g) $h=9.4 \times 10^{17}$ Au/cm², and (h) $h=1.0 \times 10^{18}$ Au/cm². The continuous lines are the fits by the log-normal function.

Stage 1: Nucleation



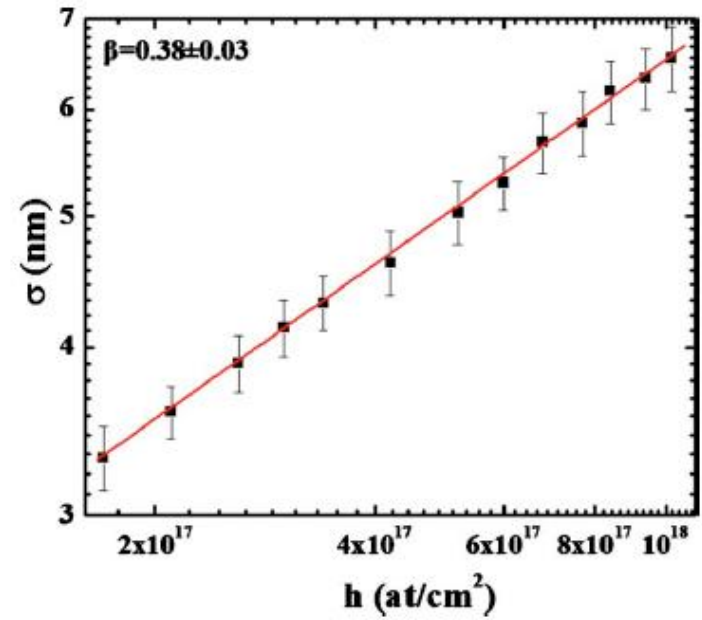
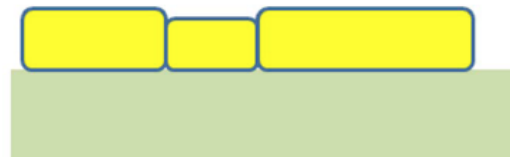
Stage 2: Lateral growth



Stage 3: Coalescence



Stage 4: Vertical growth



Chemical Physics Letters 639 (2015) 120–125



Contents lists available at [ScienceDirect](#)

Chemical Physics Letters

journal homepage: www.elsevier.com/locate/cplett



Quantitative evaluation of surface topographical changes of Au thin films after DNA immobilization



S. Spampinato^a, G. Cacciato^{a,b}, M. Zimbone^{b,*}, F. Ruffino^{a,b}, M.G. Grimaldi^{a,b}

^a Dipartimento di Fisica ed Astronomia – Università di Catania, via S. Sofia 64, 95123, Catania, Italy

^b IMM-CNR, via S. Sofia 64, 95123, Catania, Italy

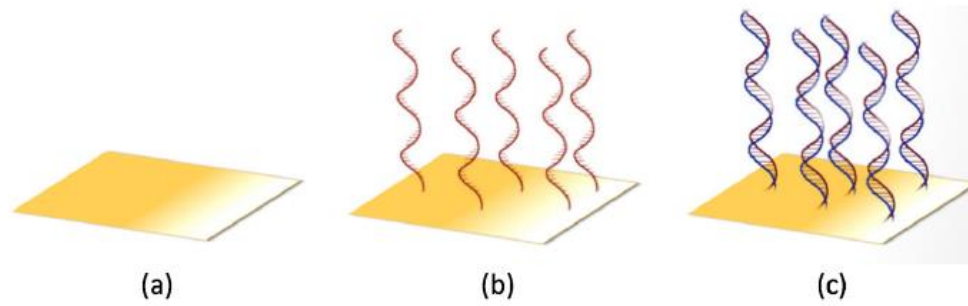


Figure 1. Schematic pictures of the analyzed samples: (a) bare Au surface, (b) Au surface after ssDNA immobilization, (c) Au surface after dsDNA hybridization.

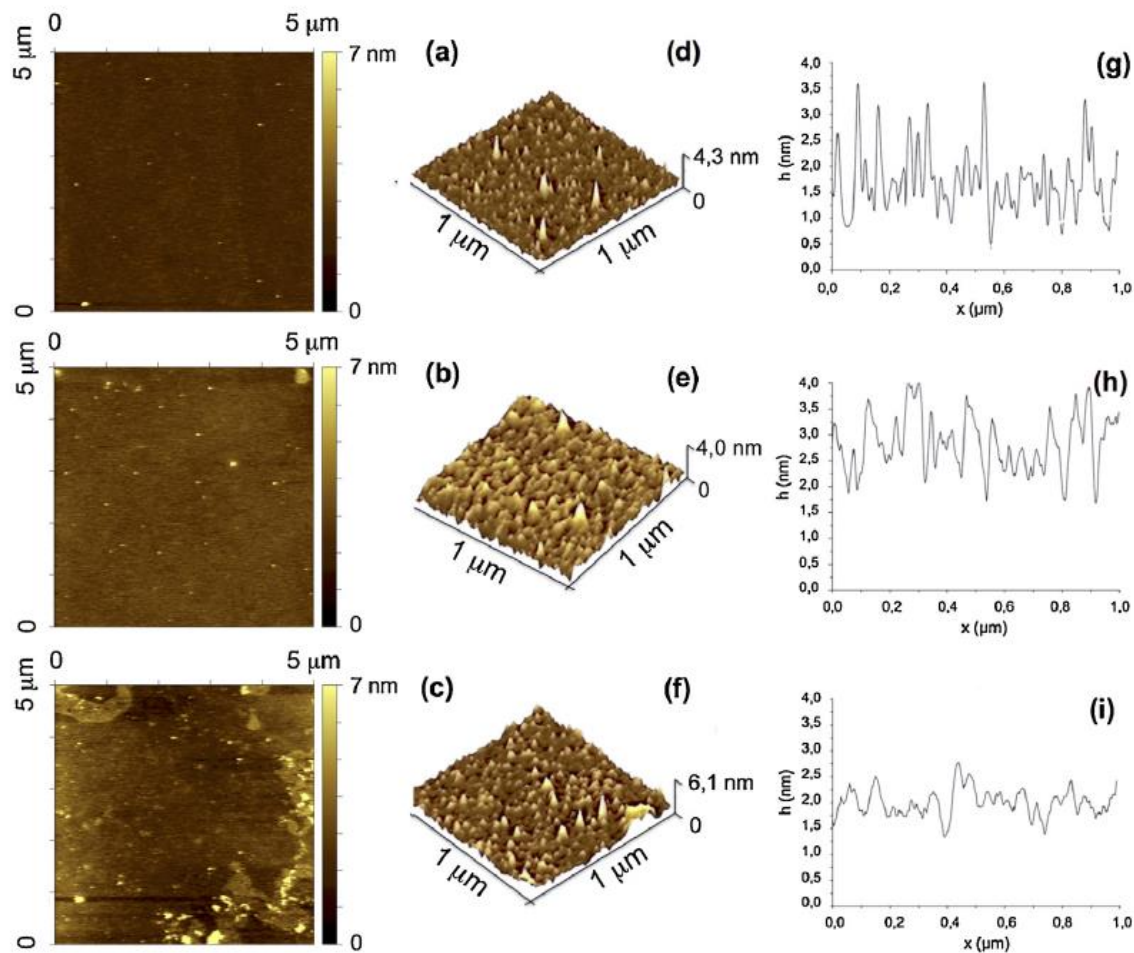


Figure 2. (a)–(c) Representative $5\ \mu\text{m} \times 5\ \mu\text{m}$ 2D AFM images corresponding to the bare Au surface (a), the Au surface after ssDNA immobilization (b), and the Au surface after dsDNA hybridization (c). (d)–(f) Representative $1\ \mu\text{m} \times 1\ \mu\text{m}$ 3D AFM images corresponding to the bare Au surface (d), the Au surface after ssDNA immobilization (e), and the Au surface after dsDNA hybridization (f). (g)–(i) Representative cross-line section profiles of the corresponding $1\ \mu\text{m} \times 1\ \mu\text{m}$ scan of the surfaces.

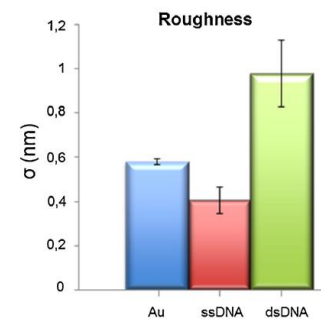


Figure 3. Calculated values for the roughness of the bare Au surface and after ssDNA immobilization and dsDNA hybridization.

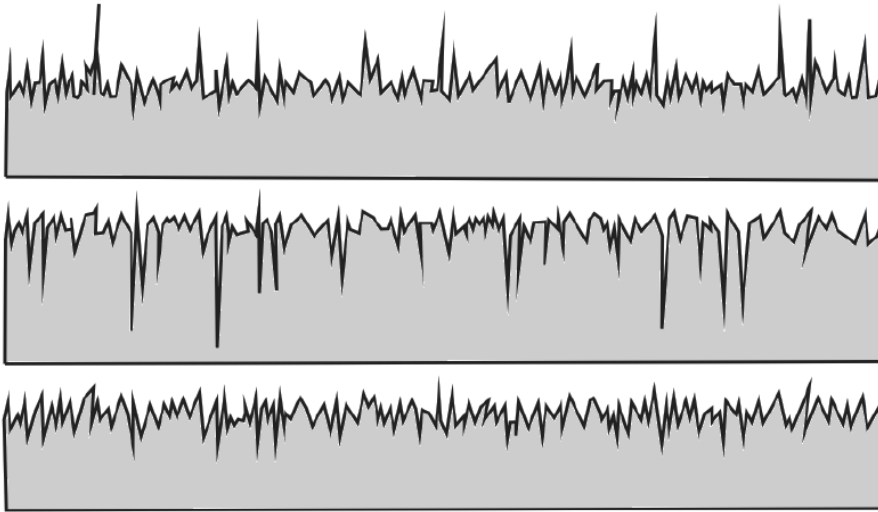


Fig. 13. Different profiles of surfaces, with the same roughness average (adapted from Predev, 2011).

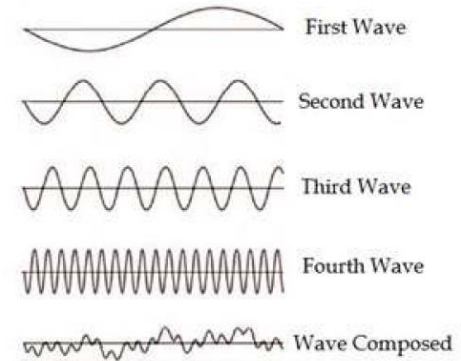


Fig. 26. Example of a wave decomposed by PSD. The sum of the four waves results in the composed wave (adapted from Freitas, A. C. P., 2010).

The power spectral density (PSD) is a complementary analysis of surface roughness which gives information related to parameters of the roughness height and spacing. The PSD is a parameter used in micrographs which relates the Fourier Transform (FT) with the root mean square roughness (RMS). The relationship between the PSD, FT and RMS is described by (Park, 2011):

$$PSD = FT^2 \quad (22)$$

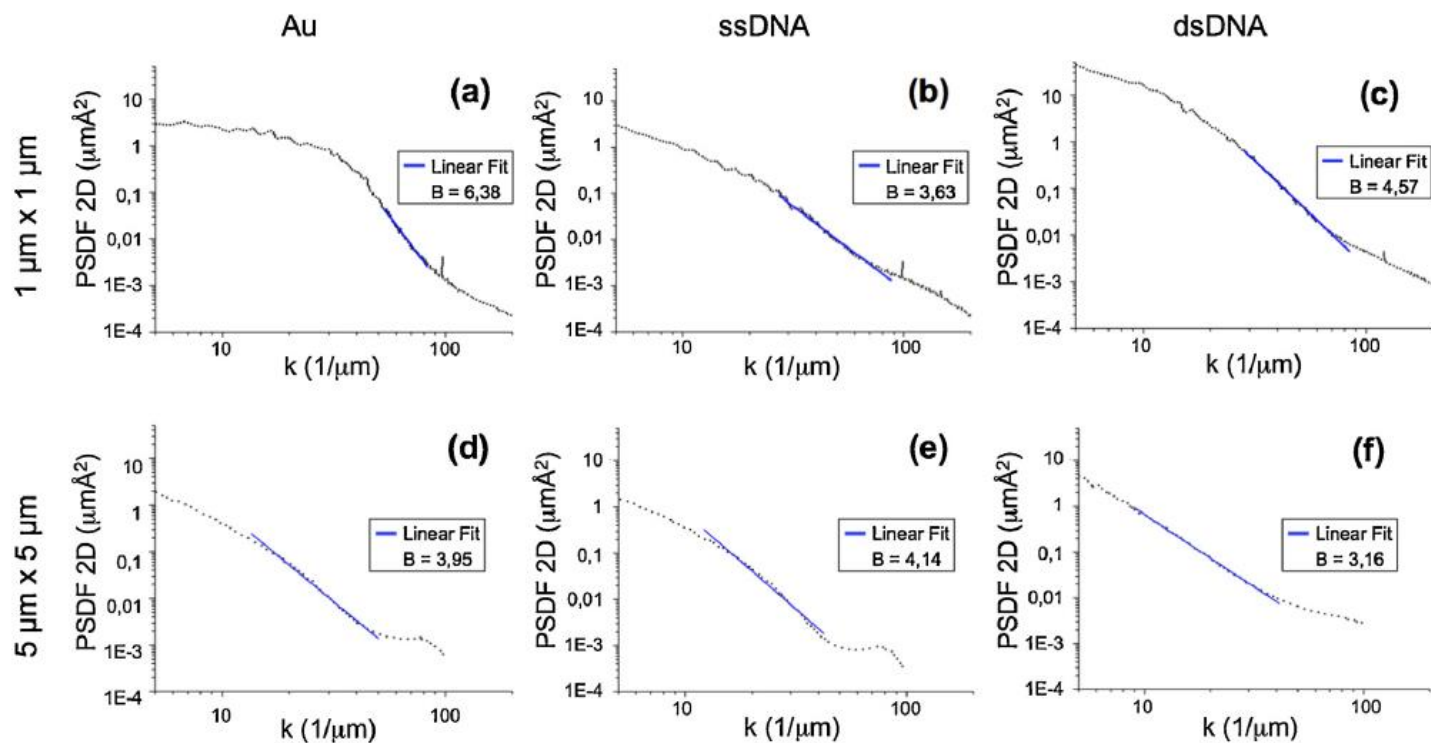


Figure 4. Representative two-dimensional PSD spectra for (a) the bare Au surface obtained by the analysis of $1 \mu\text{m} \times 1 \mu\text{m}$ scans, (b) the Au surface after ssDNA immobilization and obtained by $1 \mu\text{m} \times 1 \mu\text{m}$ scans, (c) the Au surface after dsDNA immobilization and obtained by $1 \mu\text{m} \times 1 \mu\text{m}$ scans, (d) the bare Au surface and obtained by the analysis of $5 \mu\text{m} \times 5 \mu\text{m}$ scans, (e) the Au surface after ssDNA immobilization and obtained by $5 \mu\text{m} \times 5 \mu\text{m}$ scans, (f) the Au surface after dsDNA immobilization and obtained by $5 \mu\text{m} \times 5 \mu\text{m}$ scans. The full lines are the fit of the linear regions.

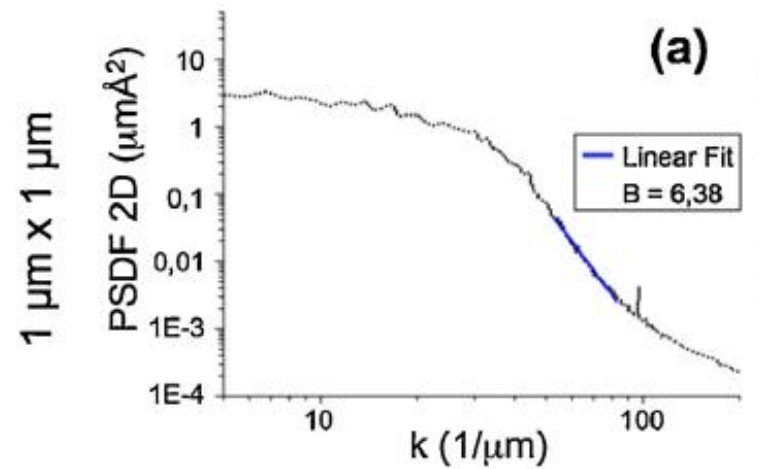
However, the roughness σ of a surface might not correctly represent the anisotropy of the topography. In fact, for example, almost similar σ values can be found for surfaces containing either few high-amplitude features or many low-lying features. Thus, we evaluated the two-dimensional fractal dimension D_f for the examined surface.

Mathematically, a surface exhibits fractal behavior when the dimension is non-integer, having fractional values [40]. For real surfaces, the fractal dimension, D_f , is $2 \leq D_f \leq 3$ and a smooth surface has a D_f value near 2, and an increasing surface roughness, either by porosity and/or relief increments, should increase the D_f value without exceeding the value of 3 [41]. At nanometric scale, most surface structures of materials have complicated shapes and surface topography is generally quantified by the roughness. Such parameter is useful to describe the surface quality, but its values can be ambiguous because the surface topography is, in general, multiscaled [42]. More information can be achieved by using a fractal approach in which the fractal dimension D_f is the parameter used to characterize the surface morphology. Furthermore, D_f should be, in principle, independent from the magnification values, going from macro or micro to nanoscale [42]. The power spectrum density (PSD) algorithm allows to estimate D_f for a surface. Each spectrum is the square of the surface roughness amplitude per spatial frequency k . The integral over all frequencies is the mean-square surface roughness within the measured bandwidth (σ^2). For exam-

a power spectrum has two distinct regions: the flat, low and very low frequency part resembling uncorrelated white noise and the sloped portion representing the correlated portion of the surface roughness. In the power spectral density showed in Figure 4, k values ranges from $5 \mu\text{m}^{-1}$ to $100 \mu\text{m}^{-1}$; in this range only medium and high k frequencies are considered and a correlated behavior is evident. The PSD of an isotropic 2D fractal Brownian function varies as [14,15,38]

$$\text{PSD} \propto k^{-B} \quad (1)$$

with $k = (x^2 + y^2)^{1/2}$ the radial frequency and $B \geq 0$ a characteristic exponent related to the fractal dimension [14,15,40,43]. So, B can be easily obtained plotting the PSD versus $1/k$ in an Arrhenius-type plot and fitting linearly the linear sloped portion of the spectrum. Appropriate values of k (from 30 to 90 μm^{-1} and from 10 to



Now, the exponent B in Eq. (1) is related to the fractal dimension D_f by [14,15,43]

$$B = 8 - 2D_f. \quad (2)$$

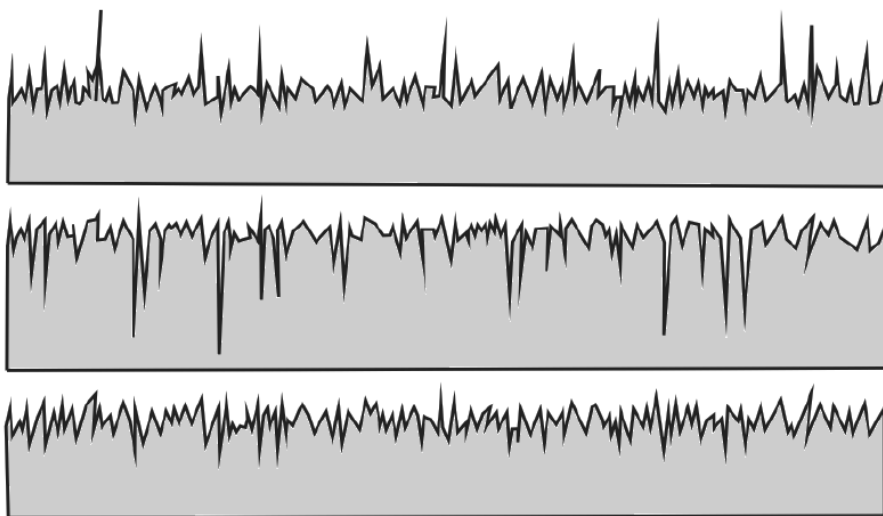


Fig. 13. Different profiles of surfaces, with the same roughness average (adapted from Predev, 2011).

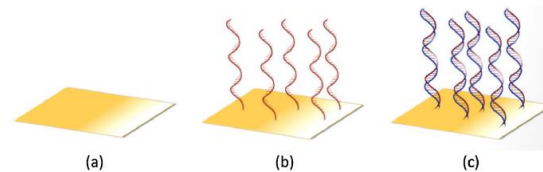
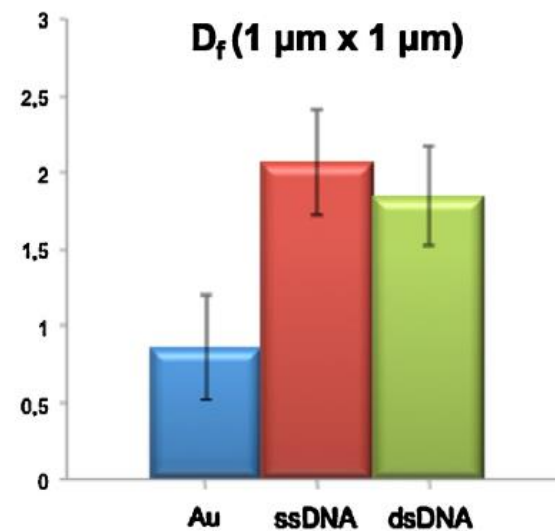


Figure 1. Schematic pictures of the analyzed samples: (a) bare Au surface, (b) Au surface after ssDNA immobilization, (c) Au surface after dsDNA hybridization.



theory [40–42] we know that for a self-affine surface the fractal dimension D_f , should not be influenced by the magnification of the AFM images and it should be $2 \leq D_f \leq 3$ (2 for a GAUSSIAN smooth surface). In spite of this, it is known that deposited metallic films on a surface growing by a Volmer–Weber mode (which is the case of Au on SiO_2 [44]) often present $D_f < 1.5$ [45]. A theory, developed by Fiorentini et al. [46], calculate a 1.2 value for film growing in a purely Volmer–Weber mode and it is verified, for example for deposited Al thin films by $3 \mu\text{m} \times 3 \mu\text{m}$ AFM scans [45]. In particular deposition conditions, Au films have shown such a low D_f value: Gómez-Rodríguez et al. [47], used scanning tunneling microscopy to study the fractal dimension of vacuum-evaporated Au film. Their films grow by a Volmer–Weber mechanism originating nano-granular Au film composed of small clusters (<30 nm) corresponding to rounded shapes with Euclidean character. In this case, for such a film, they evaluated the fractal dimension $D_f = 1$. In other deposition conditions, they obtained a film composed by bigger and ramified clusters exhibiting fractal dimension $D_f = 1.72$. Similar results were obtained by Word et al. [48] they obtained a fractal dimension $D_f \approx 1.3$ for ramified Au film on surface.

